

EUROPEAN ORGANIZATION FOR NUCLEAR RESEARCH

CERN - PS DIVISION

CERN/PS 2001-014 (OP)

NON-INVASIVE MEASUREMENT OF EMITTANCE AND OPTICAL PARAMETERS FOR HIGH-BRIGHTNESS HADRON BEAMS IN A SYNCHROTRON

A. Jansson

Abstract

For hadron colliders, such as the Large Hadron Collider at CERN, emittance preservation is of prime importance to achieve a high luminosity. Since there are no significant effects (apart from active cooling) that decrease the emittance of a hadron beam, the smallest possible emittance is set by the source, and has to be preserved along the entire injector chain. One possible source of emittance increase is due to optical mismatch at beam transfer between two machines in this chain. To verify the matching on-line requires a non-invasive instrument capable of measuring the optical parameters of the injected beam. Such instruments are very rare. A quadrupole pick-up is a non-invasive instrument sensitive to beam size. It is basically a beam position monitor, where the non-linear response to particle position is used to extract information on the second moment of the transverse beam distribution. The basic idea was proposed a long time ago, and have been successfully used at a few occasions, but have not found any widespread application. This is largely due to the fact that in the quadrupole pick-ups used so far the very small interesting signal was embedded in a massive common-mode background. The use of quadrupole pick-ups therefore required very good rejection of this background to extract the beam size information. This report describes a new design concept where, due to the pick-up geometry, there is no common-mode background. In practice, this is achieved by coupling to the radial component of the magnetic field. Analytic formulae for the transfer impedances of such a pick-up have been derived and compared with simulations and measurements on a series of prototypes. Based on these results, a quadrupole pick-up have been developed for the CERN Proton Synchrotron (PS), and its performance is discussed in detail. It is shown that installing two such instruments in well-chosen locations in a circular machine like the PS enables the measurement of matching and emittance of a single, selected bunch, with an accuracy comparable to destructive methods. Some further possible applications of quadrupole pick-ups in circular machines are also discussed.

Stockholm University

Geneva, Switzerland
11 May 2001



NON-INVASIVE MEASUREMENT OF EMITTANCE AND OPTICAL PARAMETERS FOR HIGH-BRIGHTNESS HADRON BEAMS IN A SYNCHROTRON

Dissertation

Andreas Jansson

Department of Physics
Stockholm 2001

Stockholm University – Department of Physics
Manne Siegbahn Laboratory
CERN – European Organization for Nuclear Research

CERN/PS 2001–014 (this version)

ISBN 91-7265-253-5 (printed paperback)

The corrections listed in the errata to the printed version
have been included in this version.

Abstract

For hadron colliders, such as the Large Hadron Collider at CERN, emittance preservation is of prime importance to achieve a high luminosity. Since there are no significant effects (apart from active cooling) that decrease the emittance of a hadron beam, the smallest possible emittance is set by the source, and has to be preserved along the entire injector chain.

One possible source of emittance increase is due to optical mismatch at beam transfer between two machines in this chain. To verify the matching on-line requires a non-invasive instrument capable of measuring the optical parameters of the injected beam. Such instruments are very rare.

A quadrupole pick-up is a non-invasive instrument sensitive to beam size. It is basically a beam position monitor, where the non-linear response to particle position is used to extract information on the second moment of the transverse beam distribution. The basic idea was proposed a long time ago, and have been successfully used at a few occasions, but have not found any widespread application. This is largely due to the fact that in the quadrupole pick-ups used so far the very small interesting signal was embedded in a massive common-mode background. The use of quadrupole pick-ups therefore required very good rejection of this background to extract the beam size information.

This report describes a new design concept where, due to the pick-up geometry, there is no common-mode background. In practice, this is achieved by coupling to the radial component of the magnetic field. Analytic formulae for the transfer impedances of such a pick-up have been derived and compared with simulations and measurements on a series of prototypes. Based on these results, a quadrupole pick-up have been developed for the CERN Proton Synchrotron (PS), and its performance is discussed in detail.

It is shown that installing two such instruments in well-chosen locations in a circular machine like the PS enables the measurement of matching and emittance of a single, selected bunch, with an accuracy comparable to destructive methods. Some further possible applications of quadrupole pick-ups in circular machines are also discussed.

Keywords: Quadrupole Pick-up, Beam Size Measurement, Emittance Measurement, Optical Matching, Beam Brightness, Magnetic Coupling, Synchrotron

To Jennifer.

Clarke's First Law:

> When a distinguished but elderly scientist states that something is possible, he is almost certainly right. When he states that something is impossible, he is very probably wrong.

List of publications

This thesis is based on work reported in the following papers.

1. **A New Optimised Quadrupole Pick-up Design using Magnetic Coupling**
   A. Jansson, D.J. Williams. Accepted for publication in *Nuclear Instruments and Methods in Physics Research A*. CERN-PS-2000-073-OP

2. **Optimisation of a Magnetic Quadrupole Pick-up Structure using HFSS**
   A. Jansson. In *Proceedings of the 6th International Computational Accelerator Physics Conference*, Darmstadt, Germany, 2000. CERN-PS-2000-063-OP

3. **Measurements with the Magnetic Quadrupole Pick-up in the CERN PS**
   A. Jansson, M. Lindroos, L. Søby, D.J. Williams. In *Proceedings of the 7th European Particle Accelerator Conference*, Vienna, Austria, 2000. CERN-PS-2000-020-OP

4. **A Magnetic Quadrupole Pick-up for the CERN PS**
   A. Chapman-Hatchett, A. Jansson, D.J. Williams. In *Proceedings of the 18th Particle Accelerator Conference*, New York, NY, 1999. CERN-PS-99-030-OP

The following papers, also produced during the course of the thesis work, have not been included in the thesis.

1. **Monitoring of Beam Quality in the PS Complex during the LHC Era**
   M. Benedikt et al. To be published in *Proceedings of the 2001 Workshop on Accelerator Operation*, Villars, Switzerland, 2001.

2. **'Intelligent' Automatic Beam Steering and Shaping**
   A. Jansson, M. Lindroos. In *Proceedings of the 7th European Particle Accelerator Conference*, Vienna, Austria, 2000. CERN-PS-2000-019-OP

3. **The PS Complex as Proton Pre-Injector for the LHC – Design and Implementation Report**
   M. Benedikt (ed) et al. CERN Yellow Report. CERN-2000-003

4. **A Comparative Study of Profile and Scraping Methods for Emittance Measurements in the PS Booster**
   C. Carli, A. Jansson, M. Lindroos, H Schönauer.
   Particle Accelerators, Vol. 63, pp. 255-277. CERN-PS-2000-062-OP

5. **Tomographic Reconstruction of Transverse Phase Space from Turn-by-Turn Profile Data**
   S. Hancock, A. Jansson, M. Lindroos. In *Proceedings of the 18th Particle Accelerator Conference*, New York, NY, 1999. CERN-PS-99-029-OP

6. **Simultaneous Matching of Dispersion and Twiss Parameters in a Transfer Line**
   M. Giovannozzi, A. Jansson, M. Martini. In *Proceedings of the Automated Beam Steering and Shaping Workshop*, Geneva, Switzerland, 1998. CERN-99-07

7. **Study of Emittance Blow-up Sources between the PS Booster and the 26 GeV PS**
   A. Jansson et al. In *Proceedings of the 6th European Particle Accelerator Conference*, Stockholm, Sweden, 1998. CERN-PS-98-058-OP

8. **A Comparative Study of Fast Wire Scanners, Beam Scope and SEM Grids for Emittance Measurements in the PS Booster**
   M. Arruat et al. In *Proceedings of the European Workshop on Beam Diagnostics and Instrumentation for Particle Accelerators*, Frascati, Italy, 1997. CERN-PS-97-059-BD

9. **Generic Automated Beam Steering and Shaping Programs with an Object Oriented Approach**
   M. Arruat et al. In *Proceedings of the International Conference on Accelerator and Large Experimental Physics Control Systems*, Beijing, China, 1997.
   CERN-PS-97-064-CO-OP

10. **Emittance Preservation in the PS Complex**
    B. Autin et al. In *Proceedings of the 17th Particle Accelerator Conference*, Vancouver, Canada, 1997. CERN-PS-97-049-OP

11. **Mismatch Between the PSB and CPS due to the Present Vertical Recombination Scheme**
    A. Jansson, M. Lindroos. In *Proceedings of the International Workshop on High Brightness Beams for Large Hadron Colliders*, Montreux, Switzerland, 1996. Published in Particle Accelerators Vol. 58, pp. 201-207. CERN-PS-97-014-OP

All papers can be retrieved in electronic form from the CERN Electronic Preprint Server using their reference number.

Contents

1 Introduction **1**
- 1.1 The Large Hadron Collider Project . . . 1
  - 1.1.1 Some Impressive Numbers . . . 1
  - 1.1.2 Particle Physics Motivation . . . 2
  - 1.1.3 Beam Physics Challenges . . . 3
  - 1.1.4 Implications for the Injector Chain . . . 3
- 1.2 The Emittance Measurement Problem . . . 5
  - 1.2.1 Standard Techniques to Measure Emittance . . . 6
  - 1.2.2 Quadrupole Pick-ups . . . 8
  - 1.2.3 Requirements on a Matching Detector for the PS Machine . . . 9

2 Theoretical Background **11**
- 2.1 Basic Accelerator Theory . . . 11
  - 2.1.1 Equations of Motion in the Transverse Plane . . . 11
  - 2.1.2 Motion of Off-Momentum Particles . . . 13
  - 2.1.3 Emittance and Twiss Parameters of a Beam . . . 14
  - 2.1.4 Filamentation and Emittance Increase at Injection . . . 15
  - 2.1.5 Machine Resonances . . . 16
  - 2.1.6 Linear Coupling . . . 17
  - 2.1.7 Collective Effects . . . 18
- 2.2 Pick-up Working Principles . . . 20
  - 2.2.1 Electrostatic Pick-ups . . . 20
  - 2.2.2 Magnetic Pick-ups . . . 22

3 Analytical Field Calculations **25**
- 3.1 Introduction . . . 25
- 3.2 Magnetic Field Induced by a Particle Beam . . . 26
  - 3.2.1 Infinite Beam in Free Space . . . 26
  - 3.2.2 Relation Between Beam Moments and Field Multipoles . . . 27
  - 3.2.3 Influence of a Conducting Boundary . . . 28
- 3.3 Conceptual Quadrupole Pick-up Design . . . 29
  - 3.3.1 Basic Design Idea . . . 29
  - 3.3.2 Inductive Coupling to the Beam . . . 30

3.3.3 Inductive Coupling Between Loops . . . 32
3.3.4 Antenna Loop Transfer Impedances . . . 38
3.3.5 Pick-up Transfer Impedances . . . 40
3.3.6 Pick-up Nonlinearity . . . 41
3.3.7 The Effect to Alignment Errors . . . 43

4 Applications of Quadrupole Pick-ups 45
4.1 Understanding the Quadrupole Signal . . . 45
4.1.1 Signal Components . . . 45
4.1.2 Effects of Space Charge . . . 46
4.2 Review of Previous Results . . . 47
4.2.1 Emittance Measurement in LINACs . . . 47
4.2.2 Energy Spread Measurement in Rings . . . 49
4.2.3 Study of Beam Size Oscillations in Rings . . . 49
4.2.4 Discussion on Previous Results . . . 50
4.3 Further Possible Applications in Rings . . . 50
4.3.1 Measurement of Steady-State Emittance . . . 50
4.3.2 Measuring Emittance and Matching by Matrix Inversion . . . 51
4.3.3 Measuring Emittance and Matching using a Model Fit . . . 52
4.3.4 Measurement of Coupling . . . 53
4.4 Implementation in the PS machine . . . 53
4.4.1 Pick-up Locations . . . 53
4.4.2 Error sensitivity . . . 55

5 Design of a Magnetic Quadrupole Pick-up 61
5.1 The First Pick-up Prototype . . . 61
5.2 The Lab Prototype . . . 64
5.3 The Final Optimised Pick-up . . . 65
5.4 Auxiliary Electronics . . . 65
5.4.1 Hybrid . . . 65
5.4.2 Amplifiers . . . 68

6 Bench Measurement and Simulation Methods 69
6.1 The Wire Method of Simulating a Beam . . . 69
6.1.1 Transfer Impedance Measurement . . . 69
6.1.2 Longitudinal Impedance . . . 70
6.2 Bench Measurement Setup . . . 71
6.3 The HFSS Simulation Program . . . 72
6.3.1 Program Description and Functionality . . . 72
6.3.2 Modelling the Pick-up Structure . . . 73
6.3.3 Eliminating Systematic Mesh Effects . . . 74

7 Bench Measurement and Simulation Results **77**
7.1 Transfer Impedances . . . 77
7.1.1 Verifications of Analytic Formulae . . . 77
7.1.2 Prototype Measurements and Simulations . . . 80
7.2 Undesired Couplings . . . 82
7.2.1 Antenna Loop Improvements . . . 85
7.2.2 Effects of the Coating on the Ceramic . . . 85
7.3 Longitudinal Impedance . . . 90
7.3.1 Simulations . . . 90
7.3.2 Measurements . . . 94

8 Beam Measurements **95**
8.1 Analysis of the Measured Data . . . 95
8.2 Beam-based Calibration . . . 96
8.2.1 Signal Correlations . . . 96
8.2.2 Comparison with Turn-by-Turn SEM-grid . . . 98
8.3 Sensitivity and Accuracy Estimation . . . 98
8.4 Beam Observations . . . 99
8.4.1 Coupling . . . 99
8.4.2 Space Charge Damping and Detuning . . . 100

9 Summary and Conclusions **103**
9.1 Motivation . . . 103
9.2 The New Pick-up Design . . . 104
9.3 Emittance and Matching Measurement . . . 104
9.4 Further Possibilities . . . 105

A Symbols and Acronyms **107**
A.1 Symbols . . . 107
A.2 Acronyms used in the text . . . 108

B Quadrupole signal components **109**

C Error analysis of Matrix Method **113**

References **115**

Acknowledgements **121**

"All science is either Physics or
stamp collection"

Ernest Rutherford

Chapter 1

Introduction

1.1 The Large Hadron Collider Project

1.1.1 Some Impressive Numbers

The Large Hadron Collider (LHC), currently under construction at CERN, will become the worlds highest energy accelerator when it starts up in 2005. At collision energy, its two counter-rotating beams consisting of almost 3000 bunches, each one filled with 10^{11} protons, will have an energy of 7 TeV. This corresponds to a total stored kinetic energy of 350 MJ, equivalent to about 75 kg of TNT, per beam. Along the entire machine circumference of 27 km, these beams will be kept inside a beam pipe aperture of less than 6 cm guided by a magnetic field of more than 8 T maintained by 1232 super-conducting dipole magnets. The magnets are made of low-temperature super-conducting material in order to sustain the electric current of about 12 kA needed to produce the high field. Therefore, they must be cooled to 1.8° K. Due to the large amount of energy stored in the beam, a loss of even a very small fraction of the beam particles can potentially heat the magnets sufficiently to make them quench (cease to be super-conducting), which could cause damage since the energy stored in the circulating electric current is then almost instantly converted into heat[1]

The LHC design does not only touch the limits in many different areas of technology, but also the limit of public funding for large scale research projects. To be cost effective, the machine has been designed with only very small margins, which means that the design parameters has to be strictly met in order for the collider to reach its foreseen luminosity performance. The emittance and intensity of the injected beam are just some of those critical parameters.

[1]The total energy stored in the LHC main bending magnets in the form of circulating electric currents correspond to almost 2 tons of TNT[1].

1.1.2 Particle Physics Motivation

There must be, and are indeed, very good reasons for building a machine as large and complex as the LHC. One reason is to find and study the Higgs boson that, on very strong theoretical grounds, is believed to be responsible for the spontaneous breaking of electroweak symmetry and the appearance of particle masses[2]. All available data points to a Higgs mass of a few hundred GeV/c^2, and recent hints from LEP seems to indicate a mass as low as 115 GeV/c^2[3], well within the reach of the LHC.

Also, our current understanding of the physics of fundamental particle tells us that the established theory, the standard model (SM), can not be valid to arbitrarily high energies, although it has performed wonderfully in precision measurements at the Large Electron-Positron Collider (LEP). A strong argument for this is the so-called hierarchy problem, which is linked to the fact that the Higgs mass (assuming that the Higgs exists) is not protected by any symmetry of the SM. A perturbation expansion with loop diagrams in the Higgs propagator is therefore quadratically divergent in the cut-off scale Λ, and cannot be renormalised. Since the Higgs couples to particles in proportion to their mass, the largest contribution to this effect comes from loops involving top quarks. By requiring that the Higgs mass contribution due to the interaction with the top should be smaller than the Higgs mass itself, it is possible to determine an upper limit on the cut-off energy Λ_{SM} where the SM ceases to be valid. For a Higgs mass of 200 GeV/c^2, this limit is about 700 GeV/c^2[4].

Thus, it is believed that the the SM is only an low-energy effective theory, and that a more general theory is needed. The most promising candidates for an extension of the SM are the so called super-symmetric theories. Super-symmetry provide a natural cut-off energy of the loop integrals occurring in perturbation theory, by postulating that all known particles have heavy super-symmetric partners. The typical mass of these new particles should be of the order of the cut-off energy Λ_{SM}.

Super-symmetry appearing at about 1 TeV/c^2 is also favoured by experiments, since it would make the coupling constants of the strong, electro-magnetic and weak forces meet in a single point at the energy scale Λ_{GUT}, around 10^{16} GeV[5].

Therefore, the LHC is bound to be a success. It will most likely uncover the Higgs boson, unless it has already been detected at the Fermilab Tevatron by the time the LHC experiments start up, in which case the LHC experiments will be able to study its properties in detail. Moreover, the energy range of the LHC should cover at least some of the super-symmetric particles, if they exist. Another possibility is of course that nothing at all, or something totally unexpected, will be found at the LHC. This would perhaps be the most exciting result, since then all the present theories fail and will have to be re-worked. In any case, the LHC will provide a great step forward in our understanding of Nature at the smallest and most fundamental scale.

1.1.3 Beam Physics Challenges

The most important parameter for a collider like the LHC is the luminosity $\mathcal{L}$, since it gives the number of events that will eventually be seen in the experiments. For the LHC a somewhat simplified but useful parametrisation for the luminosity is[6],

$$\mathcal{L} = \frac{\gamma_{\mathrm{L}}}{4\pi e}\frac{N_{\mathrm{p}}}{\varepsilon_{\mathrm{N}}}\frac{I_{\mathrm{p}}}{\beta^*}, \tag{1.1}$$

where γ_{L} is the relativistic Lorenz factor, N_{p} is the number of particles per bunch, ε_{N} is the normalised emittance (which is assumed to be the same in both planes), I_{p} is the total beam current and β^* is the optical beta function at the interaction point. The total beam current is limited by collective effects and the cryogenic load due to synchrotron radiation, particle losses and induced wall currents. The beam brightness $N_{\mathrm{p}}/\epsilon_{\mathrm{N}}$, on the other hand, is limited by the head-on beam-beam interaction in collision, but also by space charge effects in the low energy injector machines.

The LHC is designed to run as close as possible to these limits, in order to maximise the luminosity. The nominal target luminosity is 10^{34} cm^{-2}s^{-1}. To achieve this, the beam brightness is a key parameter. In order to provide the LHC with the brightest beam it can possibly accept, the emittance has to be kept small. There are also many beam dynamical reasons for keeping the beam emittance small[7]. Moreover, a small emittance beam has a larger safety margin for touching the vacuum pipe, which is very relevant considering the large stored beam energy and the small aperture. To protect the magnets, a sophisticated collimation scheme is foreseen, which will remove particles that are too close to the aperture, in order to prevent them from depositing their energy in the superconducting magnets. A large beam emittance will give higher losses at the collimators, and therefore a reduced intensity. The LHC parameters for protons are given in Tab. 1.1.

1.1.4 Implications for the Injector Chain

The high demands on beam quality set by the LHC are propagated down the injector chain (see Fig. 1.1) to the Super Proton Synchrotron (SPS), Proton Synchrotron (PS), the PS Booster Synchrotron (PSB), and the linacs and particle sources. Unlike the LHC, that have been optimised and built for its foreseen high-brightness beam, the machines in the injector chain were initially constructed with only the highest possible intensity in mind, and have had to be modified and upgraded to be able to deliver the bright beam required by the LHC[8].

According to Liouville's theorem of classical mechanics[9], the local phase space density is a constant of the motion. With some simplifications this can be translated into the statement that the normalised emittance is a conserved quantity. This statement is generally true, but there are some exceptions. Emission of synchrotron radiation[10], for example, can reduce the emittance, since it is a non-conservative process. Synchrotron radiation, however, is mainly an issue in electron machines. In the LHC, the damping time due to synchrotron radiation will be of the order of 40 hours, much longer than the

Parameter	Initial	Nominal	Ultimate	Unit
Beam Energy (E)	7	7	7	TeV
Luminosity ($\mathcal{L}$)	$0.1 \cdot 10^{34}$	$1.0 \cdot 10^{34}$	$2.3 \cdot 10^{34}$	$\mathrm{cm}^{-2}\mathrm{s}^{-1}$
Beam Current I_p	0.086	0.56	0.845	A
Number of bunches	2808	2808	2808	
Particles per bunch (N_p)	$0.17 \cdot 10^{11}$	$1.1 \cdot 10^{11}$	$1.67 \cdot 10^{11}$	
Bunch r.m.s. duration	-	0.28	-	ns
Bunch separation	24.95	24.95	24.95	ns
Normalised transverse emittance (ε_N)	1.0	3.75	3.75	μm
Beta at IP (β^*)	0.5	0.5	0.5	m
Beam r.m.s size at IP	4.24	15.9	15.9	μm

Table 1.1: LHC proton beam parameters at collision (compiled from LHC parameter database[1]). The initial beam will be used during machine commissioning, the nominal beam corresponds to the design value and the ultimate beam is what can be expected if all systems perform perfectly. The ultimate values are for cryogenics and instrumentation only, the magnet and powering can go to 7.54 TeV, but the beam current will then be limited by the cryogenics.

expected luminosity lifetime. There are also some ingenious inventions that can reduce the emittance. Stochastic cooling[11] uses the fact that the beam consists of a finite number of particles, and not a continuum, to re-arrange the empty space between particles to bring them closer together and decrease the emittance, while respecting Liouville's theorem. Due to resolution limits, however, it can only be used for relatively low intensity beam. Electron cooling[12] decreases the emittance of an ion beam by letting it interact with a very cool (small emittance) beam of electrons. As the two beams move towards thermal equilibrium, the ion beam emittance is transfered to the electron beam, which is eventually dumped.

Most effects that does not conserve the emittance, however, tend to increase rather than decrease it. The electromagnetic interaction between particles in the beam[13], the so-called space charge effect, creates a tune spread within the beam. If the tune spread is large enough, particles may be trapped on resonances which lead to emittance increase or even beam loss. This is mainly a concern in low energy machines, since space charge effects decrease rapidly with increasing energy. Sudden changes in the vacuum chamber shape or size can give rise to wake-fields[14] that can induce resonances and emittance growth. The vacuum chamber of high intensity machines is therefore made as smooth as possible. Rutherford scattering between individual particles in the beam, so called intra-beam scattering[15], can also lead to an increased emittance. This is mainly a problem for highly charged ions.

A relatively large emittance increase is possible in the process of transferring a beam from one machine to another. Before ejection, the beam distribution in phase space is given by the steady-state solution of the equations of motion in the sending machine. The beam is then ejected and sent through a transfer line containing bending and focusing magnets. Ideally, it should arrive in the receiving machine with a phase space distribution

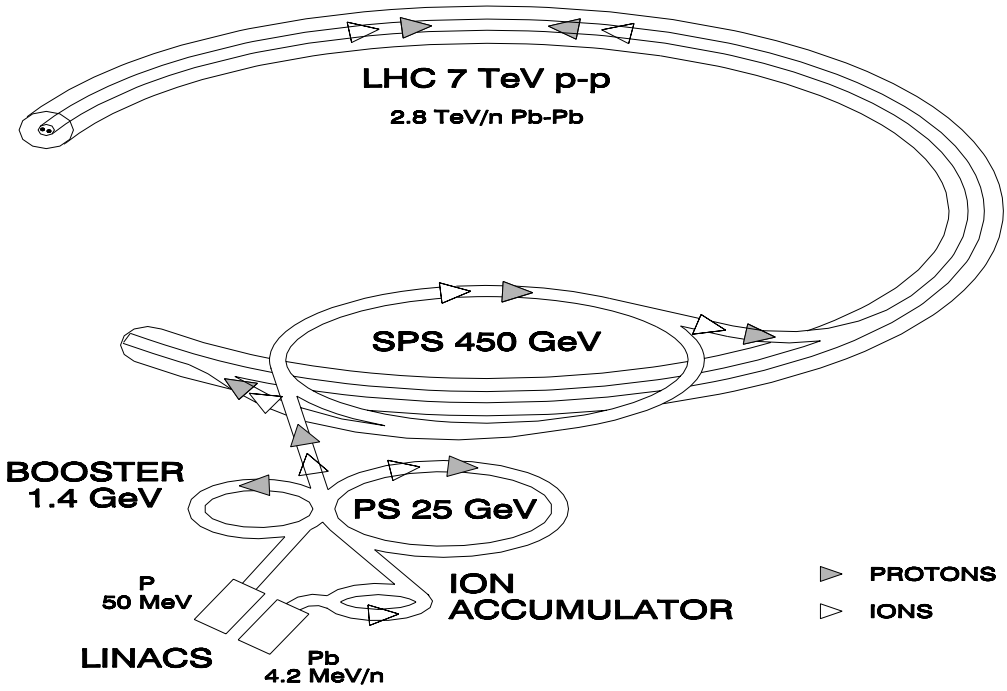

Figure 1.1: The LHC injection chain for protons and ions. The cut in the LHC shows the two separate beam pipes for the counter-rotating beams.

corresponding to the steady-state solution of that machine. This requirement applies to both mean position, size and divergence of the beam. If the beam is injected with an error, e.g. due to incorrect magnet settings in the transfer line, this will lead to emittance increase.

For the LHC beam no active cooling will be done, and synchrotron radiation damping is negligible. It is therefore essential to suppress processes that leads to emittance increase. The smallest achievable emittance is given by the emittance of the source. The difference between the source emittance and the nominal LHC emittance defines the blow-up margin. This has been allotted to the different machines in the injection chain according to Tab. 1.2. Between the exit of the Booster and the exit of the PS, the allowed emittance increase is limited to about 10%. In order to achieve this, the beam has to be carefully steered, and it optical parameters well matched to the receiving machine, when it is transfered.

1.2 The Emittance Measurement Problem

The LHC project puts high demands on the emittance preservation along the injector chain. However, the measurement of transverse emittance and matching is not trivial. The LHC

Machine	Energy	Normalised Emittance, ε_N	Batches to fill receiving machine
LHC	7 TeV	3.75 μm	-
SPS	450 GeV	3.75 μm	12
PS	26 GeV	3.5 μm	3
PSB	1.4 Gev	3.0 μm	2
LINAC	50 MeV	2.5 μm	1
RFQ	750 keV	1.2 μm	1
GUN		0.5-1.0 μm	1

Table 1.2: Normalised emittances at the exit of each machine in the injector chain, in order to finally reach the nominal LHC emittance. The beam energy and the number of batches required to fill the receiving machine is also shown. Table from [16].

emittance budget foresees a maximum increment in emittance of the order of 10% at each step in the chain. It is interesting to note that all methods for measuring the transverse emittance have errors that are expected to be in this order of magnitude[17]. The reason for this is that even if the beam size can be measured with outstanding accuracy, to turn this into a value of the emittance necessarily involves the use of some input parameters describing the optics of the machine, which introduces significant systematic errors. Also, in most cases, one has to correct for dispersive effects which are due to the energy spread of the beam, and this yields another source of systematic error. Since the statistical errors are easily reduced by collecting a large enough data set, systematic errors usually dominate completely the total error of any emittance measurement. Comparative measurement at level of 10% or better are therefore not obvious.

1.2.1 Standard Techniques to Measure Emittance

Wire Scanner

The wire-scanner[18], sometimes called flying wire, measures the beam profile by moving a wire through the beam and recording either the shower of secondary particles produced, or the secondary emission current induced in the wire. Since the wire is very thin and passes through the beam quickly, the measurement does not perturb the beam significantly, apart from at very low energies where some emittance blow-up is caused[19]. At high energies, the heating of the wire by the impinging particles can be a problem. For this reason, the method can not be used in the LHC at full intensity, since the wire would burn. The time it takes for the wire to traverse the beam is of the order of thousands of machine revolutions, so the beam must be stable during this time is order not to falsify the measurement. The beam profile obtained with a wire scanner has a very high resolution, and the error in the emittance value obtained is therefore dominated by systematic errors, as discussed previously.

BeamScope

The BeamScope[20] is an instrument used e.g. in the PS Booster. It measures the decrease in beam current as the beam is moved by a local closed orbit bump towards an aperture limitation, and gradually lost. For a constant bump velocity, the time-derivative of the measured beam intensity gives the betatron amplitude distribution, from which the the emittance can be calculated. However, in practice the measurement is quite complicated and involves sophisticated corrections for different effects, which makes it susceptible to errors. The method also requires a stable, circulating beam, which is not entirely compatible with the orbit bump, that tends to induce counter-reactions in the fast feed-back loops that are designed to keep the beam stable. Apart from potential errors introduced in the data treatment, systematic errors from machine optics parameters affects the results as in the case of the wire-scanner. Moreover, this method is totally destructive and therefore not suitable for on-line emittance monitoring.

Optical Transition Radiation

Optical Transition Radiation (OTR) screens make use of radiation emitted by a charged particle passing the boundary between two media with different refractive indices. A thin foil (usually aluminium) is placed in the beam path, and the emitted light focused onto a micro-channel plate (MCP) that amplifies it before it is measured by a CCD camera. The result is a two-dimensional profile of the beam, with a very good resolution. Since the foil can be made very thin, the effect on a beam of high-energy particles is small for a single pass. In a transfer line, three or more such screens are used together to collect enough beam size data to calculate the emittances, using the knowledge of the optics of the line.

An interesting application of OTR screens have been developed for the SPS[21], where a screen is left in the circulating beam and the beam size is measured for a number of turns immediately following the injection. In this way, correct beta matching can be ensured by verifying that the beam size is not oscillating. Since the measurement of the relative beam size oscillation amplitude is not dependent on any input parameters, this is a very accurate way to measure the matching. The data acquisition is limited by the MCP dead-time to once every four machine turns. Moreover, the screen left in the circulating beam causes some emittance blow-up, and the method is therefore not suitable for continuous monitoring.

Secondary Emission Monitors

Secondary Emission (SEM) Grids[18], or Harps, consists of a number of parallel wires. The charge deposited on the wires due to secondary emission is measured. This way one can measure the transverse beam dimensions in the horizontal and vertical planes. The standard use of SEM grids is in transfer lines, where data from several grids are used together, as in the case of the OTR screens. The grids are semi-destructive, and the resolution of the profiles is given by the wire-spacing on the grid. With a reasonable number of wires per standard deviation, the beam size can be determined with good accuracy. The

calculation of emittance requires knowledge of the optics, as in the other methods, which introduces systematic errors.

A SEM grid with a fast data acquisition system was tested in the PS Booster for space charge studies at injection[22]. This system, which was inspired by the multi-turn OTR screen measurements in the SPS, have been adapted to the PS[23] and used for some measurements presented in this report. This method is however entirely destructive, since the beam is dumped after some 50 turns to avoid damage to the grid.

1.2.2 Quadrupole Pick-ups

One way of gaining information about the beam size is to measure the quadrupole field component induced by the beam. It can be shown that its magnitude is proportional to

$$\kappa = \sigma_x^2 - \sigma_y^2 + \bar{x}^2 - \bar{y}^2, \tag{1.2}$$

where σ_x and σ_y are the horizontal and vertical r.m.s. beam size, and $\bar{x}$ and $\bar{y}$ the beam position. This measurement can be done with a so-called quadrupole pick-up. The idea of such a pick-up was first introduced by Gol'din[24] already in 1966. He proposed to use an electrostatic pick-up with parabolic electrodes following the equipotential lines of the quadrupole field component. His ideas were taken up by Nassibian at CERN, who also generalised Gol'din's work to higher order field components[25]. However, it was found that the parabolic electrodes proposed by Gol'din are not practically feasible due to their large inter-electrode capacitance that reduces the sensitivity.

Since Gol'dins proposal of a specialised quadrupole pick-up, very little work has been done in order to optimise the design of a dedicated quadrupole pick-up. Standard position pick-ups have been used, sometimes with some modifications. This is in a way a contradiction, since the quadrupole signal originates from the non-linearity of the pick-up, and position pick-ups are usually optimised to have a linear response to beam displacement. The quadrupole signal is therefore extremely small. In particular, in a perfectly linear position pick-up the quadrupole signal is absent.

Historically, two main problems have been associated with quadrupole pick-ups, and restricted their usefulness as beam size monitor. The first is that the output quadrupole signal is not only dependent on the beam dimensions, but also on the beam position. As will become clear, this is a fundamental problem which can not be solved by a clever pick-up design. It can however be overcome either by centring the beam in the pick-up or measuring the beam position and correct for its contribution. As long as the beam displacement from the centre is small compared to the beam this can be done with a reasonable accuracy.

The second and major problem is the range in signal levels involved. If the electrodes are situated at a distance a from the beam pipe centre, the ratio between the quadrupole signal and the dominating beam current signal is of the order of σ^2/a^2. Thus, if the beam is much smaller than the aperture, a very good rejection of the beam current signal is required to measure the quadrupole signal with any accuracy. However, as will be shown, the latter problem is not fundamental, but can be solved by an improved pick-up design.

In the few cases where quadrupole pick-ups have been successfully used, one can see a clear distinction in how the signals have been acquired. In electron LINACs, being single pass machines, the pick-up signal have been studied bunch-by-bunch. Typically, several measurements, using either separate pick-ups of different magnet focusing strengths, have been combined to calculate the emittance and matching[26, 27, 28]. In circular machines, however, the frequency spectrum of the signal have been studied to detect the peaks that would be produced by beam size oscillations due e.g. to bad matching[29, 30, 31]. One reason why a LINAC type emittance measurement on a single bunch was so far not attempted in a circular machine is probably that the beam-size-to-aperture ratio in is generally smaller circular machines, and therefore the common-mode rejection problem is more acute.

1.2.3 Requirements on a Matching Detector for the PS Machine

The PS machine is filled with beam from the preceding machine, the PS Booster. The Booster consists of four rings, stacked on top of each other, each containing a single bunch. At ejection, the four bunches are recombined to the level of the PS using a series of vertical kickers and septa in the transfer line. The LHC injection scheme foresees that the PS is filled with six bunches from two consecutive Booster cycles. All bunches therefore comes from either different rings or different machine cycles. Steering and matching errors should therefore be monitored on a bunch-to-bunch level. For this to be possible, the pick-up must have enough bandwidth to cover the entire bunch spectrum. In the PS this means a required bandwidth ranging from about 70 kHz to 20 MHz.

The transverse r.m.s. width of the LHC beam is of the order of 10 mm at injection into the PS, and the matching instrument should be able to measure optical mismatch (also called beta-beating) of the order of about 10%. The PS was originally built for high-intensity, large emittance beam, and its elliptical vacuum pipe has a major axis of 145 mm. To maintain the possibility of accelerating high intensity beams for parallel users, the aperture can not be reduced. Therefore, using a standard electrostatic position pick-up to measure the quadrupole moment would require a very good common-mode rejection. Test with such a pick-up was made, but did not produce useful results.

"The conventional view serves to protect us from the painful job of thinking"

J.K. Galbraith

Chapter 2

Theoretical Background

2.1 Basic Accelerator Theory

There is a wealth of introductory literature in accelerator theory[32, 33, 34]. This section is not intended as a complete overview of accelerator physics, but rather as a brief introduction to the notation used in this report. Specific references are only given for formulae that are not commonly found in introductory books.

2.1.1 Equations of Motion in the Transverse Plane

Most accelerators are made up of a sequence of magnets, where each magnet only has one field component (sometimes two). Dipole fields deflect the beam and define the beam trajectory, whereas quadrupole fields provide focusing. The sequence of magnets is called the machine lattice. Due to the focusing force of the quadrupoles, particles in the beam which are not on the central beam trajectory perform betatron oscillations. The oscillations are governed by Hill's equation, which has the form

$$\frac{\partial^2}{\partial s^2}x + K(s)x = 0 \tag{2.1}$$

where x is the deviation from the reference trajectory, s is the longitudinal coordinate along this trajectory and $K(s)$ is the quadrupole gradient[1]. The solution to Eq. (2.1) has the general form[32]

$$x = A\sqrt{\beta(s)}\sin(\mu(s) + \mu_0) \tag{2.2}$$

where the amplitude function β is referred to as the Twiss beta function and

$$\mu(s) = \int_{s_0}^{s} \frac{1}{\beta(s)}\, ds \tag{2.3}$$

[1] In the horizontal plane, there is also a focusing effect due to the curvature of the trajectory

is the phase advance. In a circular machine, the number of oscillation in one machine turn

$$Q = \frac{\nu}{2\pi} = \frac{1}{2\pi} \oint \frac{1}{\beta(s)}\, ds \tag{2.4}$$

is called the tune (the symbol ν will be used in this report for the tune as measured in radians).

By taking the derivative of Eq. (2.2) and making use of trigonometric identities one can derive the Courant-Snyder invariant

$$A^2 = \gamma(s)\, x(s)^2 + 2\,\alpha(s)\, x(s)\, x'(s) + \beta(s)\, x'(s)^2 \tag{2.5}$$

where the Twiss parameters α, β and γ are are defined as

$$x'(s) = \frac{\partial}{\partial s} x(s), \quad \alpha(s) = -\frac{1}{2}\frac{\partial}{\partial s}\beta(s), \quad \gamma(s) = \frac{1+\alpha(s)^2}{\beta(s)} \tag{2.6}$$

The form of the invariant shows that particle trajectories follow ellipses in phase space (x-x' space), and that the shape of the ellipse changes along the machine.

In practice, Eq. (2.1) is solved by piecewise integration, using a so-called hard-edge model where K is constant inside quadrupoles and zero outside. Then, one can define a transfer matrix M that relates a particle's position in x and x' at the entry and exit of an element

$$\begin{pmatrix} x \\ x' \end{pmatrix}_{\text{out}} = \underbrace{\begin{pmatrix} C & S \\ C' & S' \end{pmatrix}}_{M} \cdot \begin{pmatrix} x \\ x' \end{pmatrix}_{\text{in}} \tag{2.7}$$

where S and C are the sine-like

$$S(0) = 0, \qquad S'(0) = 1 \tag{2.8}$$

and cosine-like

$$C(0) = 1, \qquad C'(0) = 0 \tag{2.9}$$

solutions to Eq. (2.1) for constant K.

The transfer matrix for a series of elements is given by the product of their individual matrices. The sine- and cosine-like solutions for such a transfer matrix can also be expressed in terms of the Twiss parameters α, β, γ and the phase advance μ, using Eq. (2.2), which yield the parametrisation

$$M(s_1 \to s_2) = \begin{pmatrix} \sqrt{\frac{\beta_2}{\beta_1}}(\cos\Delta\mu + \alpha_1 \sin\Delta\mu) & \sqrt{\beta_2\beta_1}\sin\Delta\mu \\ -\frac{1+\alpha_1\alpha_2}{\sqrt{\beta_1\beta_2}}\sin\Delta\mu + \frac{\alpha_1-\alpha_2}{\sqrt{\beta_1\beta_2}}\cos\Delta\mu & \sqrt{\frac{\beta_1}{\beta_2}}(\cos\Delta\mu - \alpha_2\sin\Delta\mu) \end{pmatrix} \tag{2.10}$$

for the transfer matrix. If the transfer matrix describes one full turn in a circular machine, exit and entry Twiss parameters are the same, and therefore the one-turn transfer matrix of a circular machine is given by

$$M(s_1 \rightarrow s_1) = \begin{pmatrix} 1 & 0 \\ 0 & 1 \end{pmatrix} \cos \Delta\mu + \begin{pmatrix} \alpha & \beta \\ -\gamma & -\alpha \end{pmatrix} \sin \Delta\mu \tag{2.11}$$

from which the periodical (lattice) Twiss parameters can be calculated when the transfer matrix is known.

Using the Courant-Snyder invariant one can also derive the propagation rule for the Twiss functions in terms of the components of the transfer matrix

$$\begin{pmatrix} \beta_2 \\ \alpha_2 \\ \gamma_2 \end{pmatrix} = \begin{pmatrix} C^2 & -2\,S\,C & S^2 \\ -C\,C' & S\,C' + S'\,C & -S\,S' \\ C'^2 & -2\,S'\,C' & S'^2 \end{pmatrix} \cdot \begin{pmatrix} \beta_1 \\ \alpha_1 \\ \gamma_1 \end{pmatrix} \tag{2.12}$$

2.1.2 Motion of Off-Momentum Particles

Since the deflection of a charged particle in a magnetic field is dependent on the momentum of the particle, off-momentum particles do not see the same bending angle in the dipole magnets. Their reference trajectories are therefore different from on-momentum particles. This is parametrised by the dispersion function D, and its derivative with respect to s, D'. The dispersion function is defined as

$$D = \frac{\partial x}{\partial(\frac{\Delta p}{p})} \tag{2.13}$$

in other words, it describes the amount of trajectory offset per unit relative momentum offset. In a circular machine, the dispersion is defined by periodic boundary conditions, just as the Twiss functions. When dispersion is included, the position of a beam with respect to the central (on-momentum) trajectory is given by

$$x = A\sqrt{\beta}\sin(\mu - \mu_0) + \frac{\Delta p}{p} D \tag{2.14}$$

The off-momentum particles in a circular machine perform betatron oscillation with respect to their off-momentum reference orbit. Since the focusing is also affected by the momentum offset, the tunes of these particles are different. The change of tune with momentum is called the chromaticity ξ, and is defined as

$$Q' = \frac{\partial Q}{\partial(\frac{\Delta p}{p})} \tag{2.15}$$

If the chromaticity of a machine is non-zero, the momentum spread of a beam therefore gives rise to a tune spread.

2.1.3 Emittance and Twiss Parameters of a Beam

The emittance is a measure of the beam size and divergence. The statistical definition of emittance[35], which has the advantage of being independent of the detailed distribution of particles within the beam, is given by

$$\varepsilon = \sqrt{\langle x^2 \rangle \langle x'^2 \rangle - \langle x\, x' \rangle} \tag{2.16}$$

where $\langle \cdot \rangle$ denote average over all particles. Here, x and x' are the offsets with respect to the centre of the beam. The emittance is defined for the reference momentum, so any additional displacement due to momentum deviation and dispersion has to be subtracted.

The beam can be considered matched to a machine, independent of its distribution, if $\langle x^2 \rangle$, $\langle x\, x' \rangle$ and $\langle x'^2 \rangle$ are invariant under the transformation given in Eq. (2.11). In other words, if its basic phase space shape is the same after each turn in the machine. This is fulfilled if

$$\langle x^2 \rangle = \varepsilon\beta, \quad \langle x\, x' \rangle = -\varepsilon\alpha, \quad \langle x'^2 \rangle = \gamma\varepsilon \tag{2.17}$$

and it therefore makes sense to define the Twiss parameters of the beam in this way. (Where there is a possible confusion, Twiss parameters of the beam and the lattice will be separated using bar and tilde signs, i.e. $\bar{\beta}$ for the lattice beta and $\tilde{\beta}$ for the beam beta).

The emittance can therefore be calculated from the r.m.s. beam size as

$$\varepsilon = \frac{\sigma^2}{\tilde{\beta}} \tag{2.18}$$

if the beta function of the beam is known. For a stable beam in a circular machine, the beam beta function is given by the lattice. In a transfer line, one can determine the beam beta function by measuring the beam size at several locations and use the propagation equation for beta functions in Eq. (2.12).

If there is a non-zero dispersion, the extra widening of the beam due to its momentum spread has to be subtracted to calculate the emittance. Eq. (2.18) then becomes

$$\varepsilon = \frac{\sigma^2 - \sigma_p^2 \tilde{D}^2}{\tilde{\beta}} \tag{2.19}$$

where relative momentum spread is defined as

$$\sigma_{\mathrm{p}}^2 = \langle \left(\frac{\Delta p}{p} \right)^2 \rangle \tag{2.20}$$

There are also other definitions of emittance, based e.g. on the area in phase space containing a certain percentage of particles. It is however usually hard to experimentally determine these emittances without making assumptions on the beam distribution.

The emittance as defined above is a conserved quantity at fixed energy, but not during acceleration. This is because the phase space coordinates x and x', which are generally used

in accelerator physics, are not canonical coordinates. The canonical conjugate momentum to x is

$$p_x \approx p\ x' \propto\ \beta_L\gamma_L\ x' \tag{2.21}$$

but since for a constant beam energy the difference is only a fixed factor, p_x is seldom used. The normalised emittance

$$\epsilon_N = \beta_L\gamma_L\epsilon, \tag{2.22}$$

contains the relativistic factor $\beta_L\gamma_L$, and is ideally a conserved quantity. As will be discussed later, there are however some processes that can lead to its increase.

2.1.4 Filamentation and Emittance Increase at Injection

Since the beam has a tune spread, due e.g. to chromaticity, particles move around their phase space ellipses with slightly different velocities. Therefore, any coherent phase space structure in the beam will eventually decohere, and leave just the elliptic shape governed by the Twiss parameters. The process is called filamentation.

As an example, one can consider a pencil beam where all particles initially have an offset a with respect to the centre. Without tune spread the beam would oscillate coherently forever, according to the formula

$$x = a\cos\nu n \tag{2.23}$$

However, if the particles in the beam have, for example, a Gaussian distribution of tunes with standard distribution σ_ν the average position would follow

$$\bar{x} = \int_{-\infty}^{\infty} a\cos\nu n\ \ \frac{e^{-\frac{(\nu-\nu_0)^2}{2\sigma_\nu^2}}}{\sqrt{2\pi}\sigma_\nu}\,d\nu = a\ e^{-\frac{n^2\sigma_\nu^2}{2}}\ \cos\nu_0 n \tag{2.24}$$

i.e. the average beam position decays with time. The characteristic decay time is given by the inverse on the tune spread σ_ν, and the exact way the signal decays depend on the tune distribution. In the special case of a Gaussian tune distribution, the amplitude decay is also Gaussian.

In case the beam is resonantly excited by a driving term, this decoherence effect limits the coherent response. The effect is called Landau damping, and stabilises the beam against certain instabilites where the driving term is itself proportional to the coherent motion of the beam (so-called collective instabilities[36]).

The amplitude of the individual particles does not decrease with time. It is only the mean position of the beam in phase space that changes. If fact, the emittance is growing in the process. In the case of the pencil beam, the initial emittance is zero, since all particles are concentrated in one point. With time, the tune spread gives rise to a phase spread, and the beam starts to get a spatial distribution. Eventually, the particles are evenly distributed

in phase and the beam looks like a doughnut. At this point, the average position of the beam is no more oscillating, but the effective beam size has increased significantly.

This is the reason why it is very important to steer the beam onto the closed orbit at injection into a circular machine. However, also errors in the Twiss parameters and dispersion of the injected beam leads to filamentation and emittance blow-up. The r.m.s. emittance increase due to different injection errors can be calculated analytically. For a beam steering error, it is given by

$$\frac{\Delta\varepsilon}{\varepsilon} \approx \frac{1}{2}\frac{(\Delta x)^2 + (\bar{\beta}\Delta x' + \bar{\alpha}\Delta x)^2}{\varepsilon\bar{\beta}}, \tag{2.25}$$

where Δx and $\Delta x'$ are the errors in beam position and angle, respectively. For a betatron function mismatch

$$\frac{\Delta\varepsilon}{\varepsilon} \approx \frac{1}{2}(\tilde{\beta}\bar{\gamma} + \bar{\beta}\tilde{\gamma} - 2\bar{\alpha}\tilde{\alpha} - 2), \tag{2.26}$$

where, as mentioned before, barred parameters refer to the lattice and parameters with a tilde refer to the beam. For an error in dispersion function, the emittance increase is given by

$$\frac{\Delta\varepsilon}{\varepsilon} \approx \sigma_{\mathrm{p}}^2\frac{1}{2}\frac{(\Delta D)^2 + (\bar{\beta}\Delta D' + \bar{\alpha}\Delta D)^2}{\varepsilon\bar{\beta}} \tag{2.27}$$

It is interesting to note that the relative emittance increase due to beam steering and dispersion function errors are inversely proportional to the beam emittance, whereas the betatron mismatch contribution is independent of the original emittance. Moreover, the emittance increase due to a dispersion function error is quadratic in the momentum spread. Since the LHC beam will have a small emittance and large momentum spread, this hints that correcting steering and dispersion function errors will be especially important.

2.1.5 Machine Resonances

The magnets of a real machine always have some field errors. The effect of these errors is that particles get an extra kick when passing the magnet. The magnitude and direction of this kick depends on the particle position. Since the position varies from turn to turn due to the betatron oscillations, the average effect of these kicks cancel over many turns in most cases. There are however, some cases where the kicks add up. The general condition for such a resonant behaviour is[33]

$$m\,Q_x \pm n\,Q_y = P \tag{2.28}$$

where m, n and P are integers. The value

$$N = n + m \tag{2.29}$$

is called the order of the resonance. The value N defines the field component driving the resonance, which will have $2N$ poles. The distribution of these errors in the machine, on the other hand, is described by the P. When P is a multiple of the periodicity of the magnet lattice in the machine, the resonance is called systematic, and is likely to be strong. The lowest order field multipoles errors are normally largest, and therefore the lowest order resonances are the most dangerous.

The resonance condition defines lines in tune space, and can be visualised in a tune diagram (see Fig. 2.1). The position in tune space where a machine is operated is called the working point, and should be chosen far from low-order resonance lines.

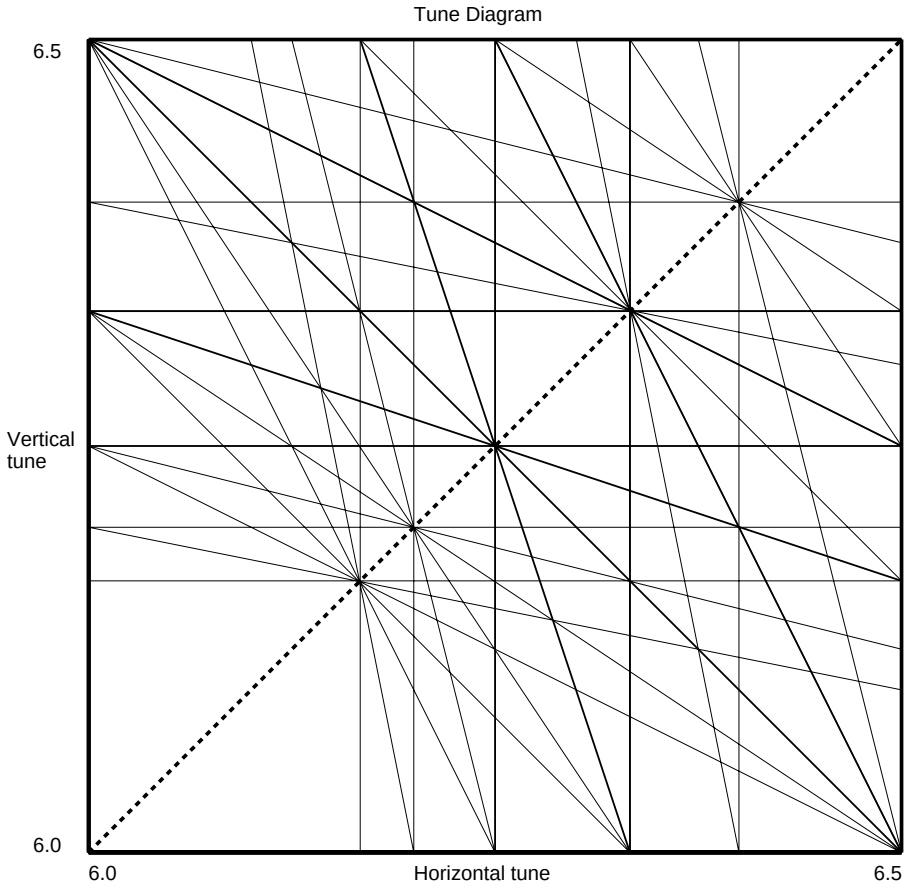

Figure 2.1: Tune diagram showing the region of tune space where the CERN PS is operated. Resonance lines up to sixth order are drawn.

2.1.6 Linear Coupling

The resonance where $Q_x = Q_y$ is called the linear coupling resonance and is driven by skew quadrupole field components. Skew quadrupoles and solenoidal fields couple the motion

in the two planes. A simple machine model with constant focusing strength yields the equations[33]

$$\begin{aligned} x'' + K_x\, x &= -b\, y' - k_s\, y \\ y'' + K_y\, y &= b\, x' - k_s x \end{aligned} \tag{2.30}$$

where k_s gives the effect of the skew quadrupoles (position coupling), and b the effect of solenoids (velocity coupling). If $\delta = K_x - K_y$ is small (close to the resonance), the equations of motion have the general solution

$$\begin{aligned} x &= A\, e^{j(K+\eta/2)s} - \frac{B(\eta-\delta)}{\sqrt{(k_s/K)^2 + b^2}} e^{j(K-\eta/2)s + j\phi} \\ y &= B\, e^{j(K-\eta/2)s} + \frac{A(\eta-\delta)}{\sqrt{(k_s/K)^2 + b^2}} e^{j(K+\eta/2)s - j\phi} \end{aligned} \tag{2.31}$$

where A and B are complex constants, $K = (K_x + K_y)/2$ and

$$\eta = \sqrt{\delta^2 + (k_s/K)^2 + b^2} \tag{2.32}$$

$$\phi = \arctan(K\, b/k_s) \tag{2.33}$$

From Eq. (2.31), the two normal modes of oscillation can be found by setting A or B to zero. In real space, the normal modes describe ellipses whose major axes are inclined by an angle α with respect to the horizontal plane, where

$$\tan\alpha = \frac{-\delta \pm \sqrt{\delta^2 + (k_s/K)^2}}{k_s/K} \tag{2.34}$$

Because of this effect, a circulating beam in a coupled machine is also tilted by the same angle.

The frequency separation of the two modes is given by η. The smallest possible separation occurs when $\delta = 0$ and is given by the magnitude

$$C = \sqrt{(k_s/K)^2 + b^2} \tag{2.35}$$

of the coupling. Thus, the coupling strength can be measured by changing the focusing in the two planes to find the minima, and measure the frequency separation.

The tilt of the normal modes give rise to an apparent amplitude interchange between horizontal and vertical plane, with a frequency given by η, i.e. the frequency difference between the two normal modes.

2.1.7 Collective Effects

So far, it was assumed that particles in the beam do not interact among themselves. This is an assumption with limited validity. The effects of the charge distribution within the beam on the beam itself are called space charge effects, and are usually separated in longitudinal and transverse phenomena.

Transverse Space Charge

There are two types of space charge interactions in the transverse plane, direct and indirect. The direct space charge is the Coulomb interaction of the charged particles among themselves. Since particles of equal charge repell each other, this is a defocusing effect. For an unbunched beam with uniform spatial distribution in a smooth machine with constant beam cross section, all particles see the same tune shift[36]

$$\Delta Q = -\frac{\lambda r_0 R}{2\varepsilon_N \beta_L \gamma_L^2} \tag{2.36}$$

where λ is the line charge of the beam, r_0 is the classical radius of the beam particle, R is the radius of the machine, β_l and γ_L the Lorenz parameters. With a more realistic particle distribution, the space charge force depends on particle position, and the result is a tune spread.

The indirect space charge effect is due to the interaction of the beam with its image charge on the conducting vacuum pipe. If the beam is off-centre, the distribution of image charges on the pipe surface will be uneven. The field produced by the unbalanced image charges exerts a force on the beam, that tends to draw it even closer to the chamber. It is therefore also a defocusing effect. The magnitude of the effect depends on the shape of the vacuum chamber and magnet pole pieces (i.e. the distribution of conducting and magnetic material around the beam), and is parametrised by the transverse impedance (measured in Ω/m).

Whereas the indirect space charge applies also to the beam as a whole, the direct space charge is only seen by individual particles in the bunch. This means that if the entire beam is oscillating coherently, the oscillation frequency will be sensitive to the indirect space charge effect, but not the direct. Thus, coherent beam oscillations can not be used to simulate the motion of particles inside the bunch in the presence of space charge. In particular, the tune as measured by kicking the beam and measuring its coherent oscillation frequency is not necessarily the same as the tune of particles inside the bunch.

If the beam is bunched, the line charge is not constant. Thus particles will see a different defocusing force depending on their longitudinal position within the bunch. This creates a tune spread within the bunch, which can be quite large.

Longitudinal Space Charge

There is also a direct space charge effect in the longitudinal plane. However, since the bunches are often much longer than their transverse dimensions, this effect is usually small. The interaction with the conducting chamber, on the other hand, is a very important effect. As mentioned before, a beam moving inside a conducting chamber induces an image current in the chamber wall. If the chamber has a constant cross-section and is perfectly conducting, the longitudinal image current distribution is a copy of the longitudinal charge distribution in the beam, when the beam velocity is close to the speed of light.

However, poor conductivity and discontinuities in the beam pipe act as an impedance for the wall currents and and can extract energy from the beam. If the impedance is

reactive, the energy is returned to the beam at a later time. In certain cases, this can lead to instabilities.

The longitudinal impedance of a machine is usually quoted as Z/n where Z is the impedance in Ohms and n is the ratio $\omega/\omega_{\text{rev}}$. This because at higher frequencies, the beam is less sensitive to the impedance, since the Landau damping is more efficient.

2.2 Pick-up Working Principles

In any accelerator or storage ring, pick-ups are standard diagnostic devices to measure the position of the beam inside the vacuum chamber. The working principle of a pick-up is to measure the relative strength of different field components induced by the beam, and the design of the instrument depends on which field that is measured.

2.2.1 Electrostatic Pick-ups

A typical electrostatic pick-up is shown schematically in Fig. 2.2 and consists of four electrodes around the beam. The passing beam induces a voltage on each of these electrodes. If the electrode is a button with radius a, the induced voltage is[37]

$$u(\omega) = i_b\left(\omega\right)\frac{a^2}{2\beta_L c}\frac{\omega/C}{j\omega + \frac{1}{RC}} \tag{2.37}$$

for a centred beam. Here, i_b is the beam current, R the load impedance and C is the capacitance of the electrode with respect to ground, which is usually a few pF. In order to get a sufficient low frequency response, the load must therefore be quite high.

The relation between the output voltage from an electrode and the beam current is called the transfer impedance

$$Z(\omega) = \frac{u(\omega)}{i_b(\omega)} \tag{2.38}$$

and is a function of beam position.

If the beam is not centred, a higher voltage will be induced on those electrodes that are closer to the beam. For small beam offsets one can obtain the beam position relative to the centre of the pick-up by combining the four signals as

$$\bar{x} \approx P_x\frac{R-L}{T+B+L+R} \tag{2.39}$$

and

$$\bar{y} \approx P_y\frac{T-B}{T+B+L+R}. \tag{2.40}$$

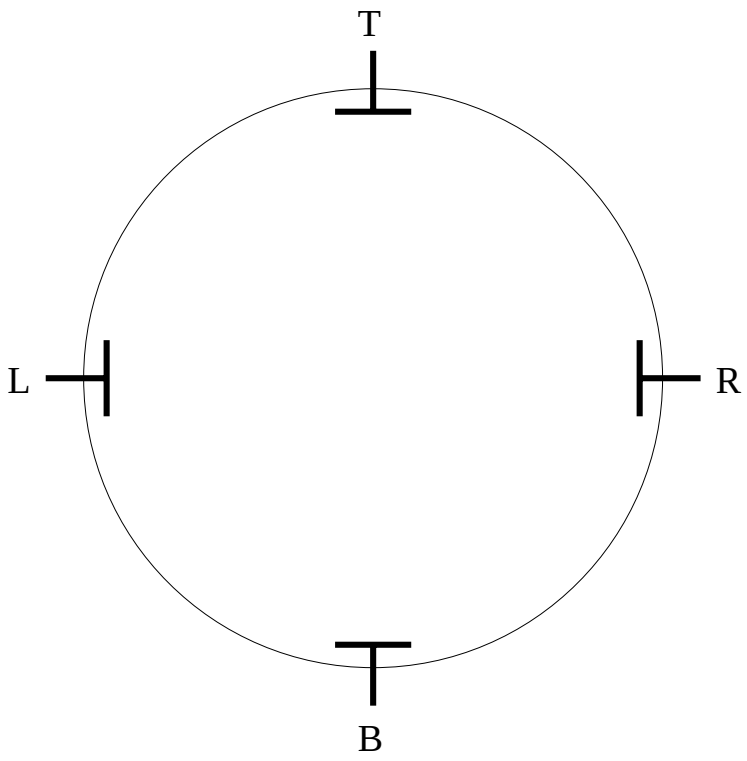

Figure 2.2: A typical electrostatic position pick-up with four buttons.

where P_x and P_y factors determined by the pick-up geometry. In the round geometry discussed above, they are simply given by the radius r of the pick-up. The division by

$$T + B + L + R \propto i_b, \tag{2.41}$$

is performed to remove the dependence on the beam current i_b. The linear relation is an approximation valid for small deviations from the centre. For large offsets, non-linear terms will become important. Position pick-ups are however usually designed to be as linear as possible.

A fourth signal can be extracted by combining the four electrode signals as

$$\Xi = \frac{R - T + L - B}{T + B + L + R}. \tag{2.42}$$

This is the so-called quadrupole signal. It originates from the non-linearity of the pick-up (more exactly, the quadratic term in beam position), and is approximately proportional to[26]

$$\kappa = \sigma_x^2 - \sigma_y^2 + \bar{x}^2 - \bar{y}^2, \tag{2.43}$$

which is referred to as the quadrupole moment.

2.2.2 Magnetic Pick-ups

Magnetic pick-ups measure the magnetic flux by means of the current induced in loops arranged around the beam. The flux is defined as:

$$\Phi = \iint_S \vec{B} \cdot d\vec{S} \tag{2.44}$$

where S is the area enclosed by the loop. The flux depends on the beam current as

$$\Phi = M\, i_b \tag{2.45}$$

where M is called the mutual inductance, and is a function of beam position. The induced voltage is given by

$$u = -\frac{\partial}{\partial t}\Phi \tag{2.46}$$

and if the loop is loaded with an impedance R, the voltage over the load is

$$u(\omega) = i_b(\omega)\, \frac{M}{L}\, \frac{R\,\omega}{\omega - j\frac{R}{L}} \tag{2.47}$$

where L is the self-inductance of the loop. Contrary to the case of an electrostatic pick-up, the load has to be small in order to achieve an good low frequency response.

In a standard magnetic position pick-up, the loops are arranged to measure the $\hat{\theta}$-component of the field (see Fig. 2.3). With this configuration, the relative magnitude of the signals induced are similar to the electrostatic case, and the output signals are combined in the same way to obtain the position in the two planes.

Magnetic pick-ups generally give lower signals than electrostatic ones, but have the advantage that they are relatively insensitive to losses, which perturbs the electrostatic pick-up signals by depositing charge on the electrodes. Therefore, magnetic position pick-ups are mainly used in machines where losses are a problem.

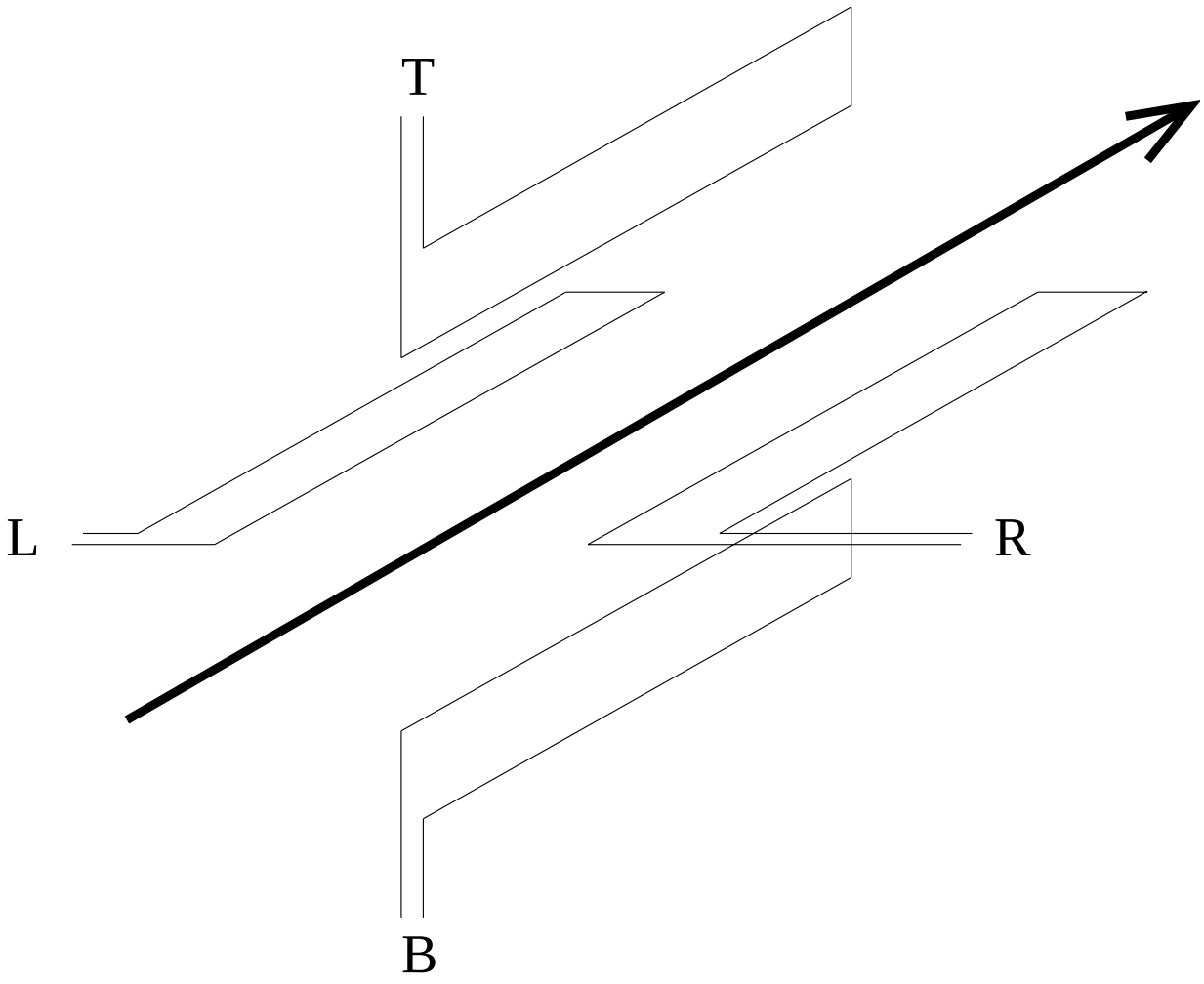

Figure 2.3: A typical magnetic position pick-up. The four antenna loops measure the azimuthal field components induced by the beam. The arrow symbolises the beam.

"Do not worry about your difficulties in mathematics. I can assure you that mine are still greater."

Albert Einstein

Chapter 3

Analytical Field Calculations

3.1 Introduction

A derivation of the couplings of a pick-up inevitably starts with the calculation of the particular field that the pick-up is sensitive to.

In the ultra-relativistic limit, the fields created by a beam of particles inside a smooth conducting pipe are purely transverse[38]. Therefore, field calculations can be reduced to only the two transverse coordinates. The transfer impedances of an electrostatic pick-up are usually calculated via the image current distribution induced by the beam on the inside of the conducting vacuum pipe. In a cylindrical pipe of diameter d, this distribution is

$$J_{\mathrm{w}}(d,\theta) = \frac{i_{\mathrm{b}}}{2\pi d}\left(1 + 2\left[\frac{\bar{x}}{d}\cos\theta + \frac{\bar{y}}{d}\sin\theta + \left(\frac{\sigma_x^2 - \sigma_y^2}{d^2} + \frac{\bar{x}^2 - \bar{y}^2}{d^2}\right)\cos 2\theta + \ldots\right]\right). \quad (3.1)$$

where θ is the azimuthal angle. Although this result has often been derived assuming a Gaussian beam distribution[26, 39], it is in fact completely independent of the exact distribution of the particles in the beam[40]. For a given electrode position, Eq. (3.1) gives the relative magnitude of different signal components. What is important for the measurement of the quadrupole moment is that on a given electrode the component containing the beam size information is a very small part of the total signal. It could be argued that the pick-up could be made more sensitive to the beam size by optimising the beam pipe and electrode geometry, but the simple fact that the total image current equals the total beam current means that there will always be a strong common-mode component in the electrode signal. This is an inherent property of all electrostatic pick-ups, but is not necessarily true for magnetic ones.

3.2 Magnetic Field Induced by a Particle Beam

3.2.1 Infinite Beam in Free Space

Under quasi-static conditions, the magnetic field created by a current distribution $\vec{J}$ is given by the formula[41]

$$\vec{B}(\vec{r}) = \frac{\mu_0}{4\pi} \iiint \frac{\vec{J}(\vec{r'}) \times (\vec{r} - \vec{r'})}{\left|\vec{r} - \vec{r'}\right|^3} \, dx' \, dy' \, dz' \tag{3.2}$$

where $\vec{r'} = x'\hat{x} + y'\hat{y} + z'\hat{z}x'$ are the source coordinates and $\vec{r} = x\hat{x} + y\hat{y} + z\hat{z}$ is the point where the field is measured. If it is assumed that the current distribution is an infinitely long relativistic particle beam of constant cross section, aligned with the z axis, then $J = J(x, y)\,\hat{z}$ and

$$\vec{B}(x, y, z) = \frac{\mu_0}{4\pi} \iiint \frac{J(x', y')\big((y - y')\hat{x} - (x - x')\hat{y}\big)}{\big((x - x')^2 + (y - y')^2 + (z - z')^2\big)^{3/2}} \, dz' \, dx' \, dy' \tag{3.3}$$

A partial integration over z from minus to plus infinity can then be performed, leaving

$$\vec{B}(x, y) = \frac{\mu_0}{2\pi} \iint \frac{J(x', y') \cdot \big((y - y')\hat{x} - (x - x')\hat{y}\big)}{(x - x')^2 + (y - y')^2} \, dx' \, dy' \tag{3.4}$$

It is useful to Taylor expand the integrand with respect to the source coordinates, which gives the result

$$\begin{aligned} &\vec{B}(x, y) = \\ &\quad = \frac{\mu_0}{2\pi} \iint \sum_{i=0}^{\infty} \sum_{j=0}^{\infty} J(x', y') \, x'^i \, y'^j \frac{1}{i!j!} \left[\frac{\partial^{i+j}}{\partial x'^i \partial y'^j} \frac{(y - y')\hat{x} - (x - x')\hat{y}}{(x - x')^2 + (y - y')^2} \right]_{\substack{x'=0 \\ y'=0}} dx' \, dy' \end{aligned} \tag{3.5}$$

The term in brackets can then be rewritten using the trivial relation

$$\frac{\partial f(x - x')}{\partial x'} = -\frac{\partial f(x - x')}{\partial x} \tag{3.6}$$

after which x' and y' can be set to zero, yielding the solution

$$\vec{B}(x, y) = \frac{\mu_0}{2\pi} \sum_{i=0}^{\infty} \sum_{j=0}^{\infty} \underbrace{\iint J(x', y') \, x'^i \, y'^j \, dx' \, dy'}_{\text{source}} \cdot \underbrace{\frac{(-1)^{i+j}}{i!\, j!} \frac{\partial^{i+j}}{\partial x^i \partial y^j} \frac{y\hat{x} - x\hat{y}}{x^2 + y^2}}_{\text{field}} \tag{3.7}$$

where field and source properties have been conveniently separated.

3.2.2 Relation Between Beam Moments and Field Multipoles

The expression for the magnetic field in Eq. (3.7) can be written in short form as

$$\vec{B}(x,y) = \sum_{i=0}^{\infty}\sum_{j=0}^{\infty} m_{ij}\,\vec{B}_{ij} \tag{3.8}$$

where the quantities

$$m_{ij} = \iint J(x',y')\,x'^{i}\,y'^{j}\,dx'\,dy' \tag{3.9}$$

are the so-called moments[42] of the current distribution $J(x,y)$. The number $i+j$ is the order of the moment. The $\vec{B}_{ij}$ terms correspond to field multipoles of order $i+j$. The lowest order beam moments and the corresponding magnetic field components are listed in Tab. 3.1.

Moment	Related beam parameter	$\vec{B}$-field component
$m_{00} = \iint J(x,y)\,dx\,dy$	Total beam current	$-m_{00}\frac{\mu_0}{2\pi}\frac{1}{\rho}\hat{\theta}$
$m_{10} = \iint x\,J(x,y)\,dx\,dy$	Horizontal beam position	$-m_{10}\frac{\mu_0}{2\pi}\left(\frac{\cos\theta}{\rho^2}\hat{\theta} - \frac{\sin\theta}{\rho^2}\hat{\rho}\right)$
$m_{01} = \iint y\,J(x,y)\,dx\,dy$	Vertical beam position	$-m_{01}\frac{\mu_0}{2\pi}\left(\frac{\sin\theta}{\rho^2}\hat{\theta} + \frac{\cos\theta}{\rho^2}\hat{\rho}\right)$
$m_{20} = \iint x^2\,J(x,y)\,dx\,dy$	Horizontal beam width	$-m_{20}\frac{\mu_0}{2\pi}\left(\frac{\cos 2\theta}{\rho^3}\hat{\theta} - \frac{\sin 2\theta}{\rho^3}\hat{\rho}\right)$
$m_{11} = \iint x\,y\,J(x,y)\,dx\,dy$	Beam tilt (coupling)	$-2m_{11}\frac{\mu_0}{2\pi}\left(\frac{\sin 2\theta}{\rho^3}\hat{\theta} + \frac{\cos 2\theta}{\rho^3}\hat{\rho}\right)$
$m_{02} = \iint y^2\,J(x,y)\,dx\,dy$	Vertical beam width	$m_{20}\frac{\mu_0}{2\pi}\left(\frac{\cos 2\theta}{\rho^3}\hat{\theta} - \frac{\sin 2\theta}{\rho^3}\hat{\rho}\right)$
$m_{30} = \iint x^3\,J(x,y)\,dx\,dy$	-	$-m_{30}\frac{\mu_0}{2\pi}\left(\frac{\cos 3\theta}{\rho^4}\hat{\theta} - \frac{\sin 3\theta}{\rho^4}\hat{\rho}\right)$
$m_{21} = \iint x^2\,y\,J(x,y)\,dx\,dy$	-	$-3m_{21}\frac{\mu_0}{2\pi}\left(\frac{\sin 3\theta}{\rho^4}\hat{\theta} + \frac{\cos 3\theta}{\rho^4}\hat{\rho}\right)$
$m_{12} = \iint x\,y^2\,J(x,y)\,dx\,dy$	-	$3m_{12}\frac{\mu_0}{2\pi}\left(\frac{\cos 3\theta}{\rho^4}\hat{\theta} - \frac{\sin 3\theta}{\rho^4}\hat{\rho}\right)$
$m_{03} = \iint y^3\,J(x,y)\,dx\,dy$	-	$m_{03}\frac{\mu_0}{2\pi}\left(\frac{\sin 3\theta}{\rho^4}\hat{\theta} + \frac{\cos 3\theta}{\rho^4}\hat{\rho}\right)$

Table 3.1: Summary of current density moments of a beam, and their corresponding field components in cylindrical coordinates.

There exists a general theorem[43] stating that any distribution can be reconstructed if all its moments are known. This have lead to attempts at TRIUMF to build octupole, hexapole and even higher order mode pick-ups measuring wall current distributions in the beam pipe[44, 45, 46]. However, as pointed out by Nassibian[47], it is impossible to obtain all beam moments by measuring the field around the beam, since there are $k+1$ moments of a given order, but not more than two independent multipole field components.

What can be measured are not the moments directly, but the field components. From the strength of a given field component, one can deduce the value for certain combinations of those moments producing that particular field component. These combinations of moments are the multipole moments given in Tab. 3.2.

Multipole moment	Multipole name	Corresponding $\vec{B}$-field component
$i_b = \iint J(x,y)\,dx\,dy$	Monopole	$-i_b\,\frac{\mu_0}{2\pi}\frac{1}{\rho}\hat{\theta}$
$i_b\,\bar{x} = \iint x\,J(x,y)\,dx\,dy$	Horizontal dipole	$-i_b\,\bar{x}\,\frac{\mu_0}{2\pi}\left(\frac{\cos\theta}{\rho^2}\hat{\theta} - \frac{\sin\theta}{\rho^2}\hat{\rho}\right)$
$i_b\,\bar{y} = \iint y\,J(x,y)\,dx\,dy$	Vertical dipole	$-i_b\,\bar{y}\,\frac{\mu_0}{2\pi}\left(\frac{\sin\theta}{\rho^2}\hat{\theta} + \frac{\cos\theta}{\rho^2}\hat{\rho}\right)$
$i_b\,\kappa = \iint (x^2-y^2)\,J(x,y)\,dx\,dy$	Normal quadrupole	$-i_b\,\kappa\,\frac{\mu_0}{2\pi}\left(\frac{\cos 2\theta}{\rho^3}\hat{\theta} - \frac{\sin 2\theta}{\rho^3}\hat{\rho}\right)$
$i_b\,\kappa' = \iint 2\,x\,y\,J(x,y)\,dx\,dy$	Skew quadrupole	$-i_b\,\kappa'\,\frac{\mu_0}{2\pi}\left(\frac{\sin 2\theta}{\rho^3}\hat{\theta} + \frac{\cos 2\theta}{\rho^3}\hat{\rho}\right)$
$i_b\,\zeta = \iint (x^3 - 3\,x\,y^2)\,J(x,y)\,dx\,dy$	Normal sextupole	$-i_b\,\zeta\,\frac{\mu_0}{2\pi}\left(\frac{\cos 3\theta}{\rho^4}\hat{\theta} - \frac{\sin 3\theta}{\rho^4}\hat{\rho}\right)$
$i_b\,\zeta' = \iint (3\,y\,x^2 - y^3)\,J(x,y)\,dx\,dy$	Skew sextupole	$-i_b\,\zeta'\,\frac{\mu_0}{2\pi}\left(\frac{\sin 3\theta}{\rho^4}\hat{\theta} + \frac{\cos 3\theta}{\rho^4}\hat{\rho}\right)$

Table 3.2: Summary of multipole moments of a beam, and their corresponding field component in cylindrical coordinates.

3.2.3 Influence of a Conducting Boundary

Writing down the expression for the field including components up to sextupole yields

$$\begin{aligned}\vec{B}(\rho,\theta) = -i_b\,\frac{\mu_0}{2\pi}\Bigg[&\frac{1}{\rho}\hat{\theta} + \bar{x}\left(\frac{\cos\theta}{\rho^2}\hat{\theta} - \frac{\sin\theta}{\rho^2}\hat{\rho}\right) + \bar{y}\left(\frac{\sin\theta}{\rho^2}\hat{\theta} + \frac{\cos\theta}{\rho^2}\hat{\rho}\right) + \\ &+ \kappa\left(\frac{\cos 2\theta}{\rho^3}\hat{\theta} - \frac{\sin 2\theta}{\rho^3}\hat{\rho}\right) + \kappa'\left(\frac{\sin 2\theta}{\rho^3}\hat{\theta} + \frac{\cos 2\theta}{\rho^3}\hat{\rho}\right) + \\ &+ \zeta\left(\frac{\cos 3\theta}{\rho^4}\hat{\theta} - \frac{\sin 3\theta}{\rho^4}\hat{\rho}\right) + \zeta'\left(\frac{\sin 3\theta}{\rho^4}\hat{\theta} + \frac{\cos 3\theta}{\rho^4}\hat{\rho}\right) + \ldots\Bigg] \quad (3.10)\end{aligned}$$

If the current density is enclosed in a perfectly conducting cylindrical pipe with inner radius d, image currents will be induced on the inside of the pipe, as mentioned before. These currents also induce a magnetic field. Since this field has no sources inside the pipe, it can be expressed in a standard multipole expansion as

$$\begin{aligned}\vec{B}_{\text{wall}}(\rho,\theta) = &\,b_1\left(\cos\theta\;\hat{\theta} + \sin\theta\;\hat{\rho}\right) + b_2\left(\sin\theta\;\hat{\theta} - \cos\theta\;\hat{\rho}\right) + \\ &+ c_1\left(\rho\;\cos 2\theta\;\hat{\theta} + \rho\;\sin 2\theta\;\hat{\rho}\right) + c_2\left(\rho\;\sin 2\theta\;\hat{\theta} - \rho\;\cos 2\theta\;\hat{\rho}\right) + \\ &+ d_1\left(\rho^2\;\cos 3\theta\;\hat{\theta} + \rho^2\;\sin 3\theta\;\hat{\rho}\right) + d_2\left(\rho^2\;\sin 3\theta\;\hat{\theta} - \rho^2\;\cos 3\theta\;\hat{\rho}\right) + \ldots \quad (3.11)\end{aligned}$$

As the radial component of the total magnetic field has to vanish at the perfectly conducting boundary, the coefficients can be found by term-wise identification, and the total field inside the pipe is given by

$$\begin{aligned}\vec{B}_{\mathrm{tot}}(\rho,\theta) = \\ -i_b\frac{\mu_0}{2\pi}\Bigg[\frac{1}{\rho}\hat{\theta} + \left(1+\frac{\rho^2}{d^2}\right)\left(\bar{x}\frac{\cos\theta}{\rho^2}+\bar{y}\frac{\sin\theta}{\rho^2}\right)\hat{\theta} - \left(1-\frac{\rho^2}{d^2}\right)\left(\bar{x}\frac{\sin\theta}{\rho^2}-\bar{y}\frac{\cos\theta}{\rho^2}\right)\hat{\rho} + \\ + \left(1+\frac{\rho^4}{d^4}\right)\left(\kappa\frac{\cos 2\theta}{\rho^3}+\kappa'\frac{\sin 2\theta}{\rho^3}\right)\hat{\theta} - \left(1-\frac{\rho^4}{d^4}\right)\left(\kappa\frac{\sin 2\theta}{\rho^3}-\kappa'\frac{\cos 2\theta}{\rho^3}\right)\hat{\rho} + \\ + \left(1+\frac{\rho^6}{d^6}\right)\left(\zeta\frac{\cos 3\theta}{\rho^4}+\zeta'\frac{\sin 3\theta}{\rho^4}\right)\hat{\theta} - \left(1-\frac{\rho^6}{d^6}\right)\left(\zeta\frac{\sin 3\theta}{\rho^4}-\zeta'\frac{\cos 3\theta}{\rho^4}\right)\hat{\rho} + \ldots\Bigg] \quad (3.12)\end{aligned}$$

The radial components of the field are suppressed by the presence of the conducting boundary, whereas the azimuthal components are enhanced. It is interesting to see that Eq. (3.1) can be derived from this result by calculating the field at the conducting boundary

$$\vec{B}_{\mathrm{tot}}(\rho,\theta) = -\frac{\mu_0\, i_{\mathrm{b}}\,\hat{\theta}}{2\pi d}\left[1+2\left(\bar{x}\frac{\cos\theta}{d}+\bar{y}\frac{\sin\theta}{d}\right)+2\left(\kappa\frac{\cos 2\theta}{d^2}+\kappa'\frac{\sin 2\theta}{d^2}\right)+\ldots\right] \quad (3.13)$$

and using the fact that the current induced on a conducting boundary is proportional to the tangential component of the magnetic field.

3.3 Conceptual Quadrupole Pick-up Design

3.3.1 Basic Design Idea

A big difference between magnetic and electric coupling is the fact that using magnetic coupling, not only the magnitude of the field can be measured, but also its direction. Thus, for the design of a magnetic pick-up, there is an extra degree of freedom. Magnetic pick-ups are traditionally made to couple to the azimuthal field component. From the conjecture between the azimuthal field component at the boundary and the wall current distribution, one can infer that a magnetic pick-up measuring the azimuthal field component will always have a similar behaviour to an electrostatic pick-up. In particular, the output signal will have a similar dependence on beam current, position and size. Therefore, there is not much to be gained by designing a quadrupole pick-up as a 'traditional' magnetic position pick-up.

However, from the above derivation of the beam-induced magnetic field it can be seen that the monopole field mode, that is the origin of the common-mode signal in 'conventional' quadrupole pick-ups, does not have any $\hat{\rho}$ component. Thus, one can avoid to couple to the monopole mode by building a pick-up that measures B_ρ.

This is achieved by shaping the antenna loops as a cylinder around the beam, as shown in Fig. 3.1. To be sensitive to the normal quadrupole mode (corresponding to κ) the loops

should be situated at 45° to the horizontal plane, since the field strength is maximum there. A pick-up with loops aligned with the horizontal and vertical planes would measure the skew quadrupole mode (corresponding to κ').

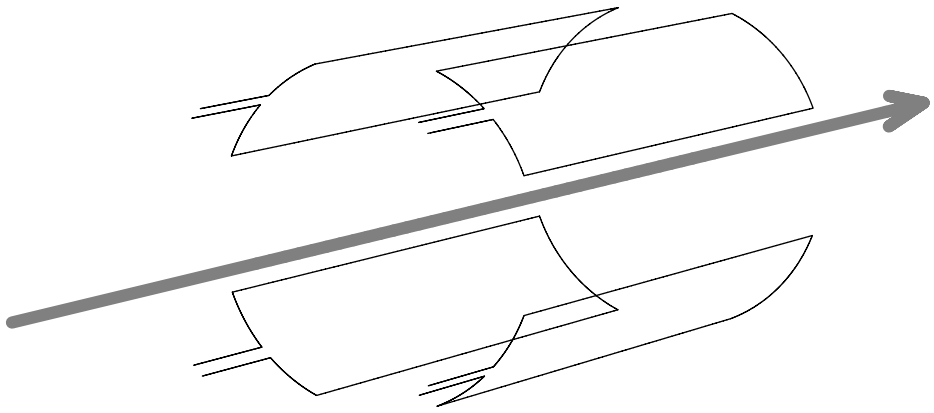

Figure 3.1: Arrangement of antenna loops to couple to the radial component of the magnetic field. The arrow symbolises the beam.

By building a pick-up in this way, the requirements on dynamic range and common mode rejection in the electronics analysing the pick-up signals are considerably relieved. But suppressing the common mode signal also means that the pick-up loses its ability to measure the beam current, which is needed to normalise the other signals. However, dedicated beam current monitors are part of the standard diagnostic equipment of any machine, so this it not a problem.

When the common-mode (intensity) signal is removed, the next strongest signal is normally the dipole signal. But the dipole signal is proportional to beam position, and vanishes when the beam is centred. In this case, the quadrupole signal is the dominating signal on the output of the antenna loops.

3.3.2 Inductive Coupling to the Beam

The mutual inductance between the beam and an antenna loop is defined as the magnetic flux through the loop per unit beam current. If the loop is oriented to measure the radial field component, the mutual inductance can be expanded

$$M_{\mathrm{b}} = M^{(x)}x + M^{(y)}y + M^{(\kappa)}\kappa + M^{(\kappa')}\kappa' + M^{(\zeta)}\zeta + M^{(\zeta')}\zeta' + \ldots \tag{3.14}$$

where each coefficient $M^{(\cdot)}$ is given by the corresponding field components in Eq. (3.12).

If the pick-up loops are situated at a distance ρ from the centre, at 45° the horizontal plane, and with an opening angle as seen from the centre of ϕ, the mutual inductances corresponding to dipole terms in the field expansion are given by

$$M_{bn}^{(x)} = \frac{\mu_0}{2\pi}\int_{\frac{n\pi}{2}+\frac{\pi}{4}-\frac{\phi}{2}}^{\frac{n\pi}{2}+\frac{\pi}{4}+\frac{\phi}{2}} \left(1-\frac{\rho^2}{d^2}\right)\frac{\sin\theta}{\rho^2}\,\rho d\theta = \\ = \frac{\mu_0}{2\pi}\underbrace{\left(\sin\frac{n\pi}{2}+\cos\frac{n\pi}{2}\right)}_{s_n^{(x)}=\pm 1}\sqrt{2}\left(1-\frac{\rho^2}{d^2}\right)\frac{\sin\frac{\phi}{2}}{\rho} \quad (3.15)$$

and

$$M_{bn}^{(y)} = -\frac{\mu_0}{2\pi}\int_{\frac{n\pi}{2}+\frac{\pi}{4}-\frac{\phi}{2}}^{\frac{n\pi}{2}+\frac{\pi}{4}+\frac{\phi}{2}} \left(1-\frac{\rho^2}{d^2}\right)\frac{\cos\theta}{\rho^2}\,\rho d\theta = \\ = \frac{\mu_0}{2\pi}\underbrace{\left(\sin\frac{n\pi}{2}-\cos\frac{n\pi}{2}\right)}_{s_n^{(y)}=\pm 1}\sqrt{2}\left(1-\frac{\rho^2}{d^2}\right)\frac{\sin\frac{\phi}{2}}{\rho} \quad (3.16)$$

per unit pick-up length and unit beam displacement. For the quadrupole terms, the mutual inductances are

$$M_{bn}^{(\kappa)} = \frac{\mu_0}{2\pi}\int_{\frac{n\pi}{2}+\frac{\pi}{4}-\frac{\phi}{2}}^{\frac{n\pi}{2}+\frac{\pi}{4}+\frac{\phi}{2}} \left(1-\frac{\rho^4}{d^4}\right)\frac{\sin 2\theta}{\rho^3}\,\rho d\theta = \frac{\mu_0}{2\pi}\underbrace{\cos n\pi}_{s_n^{(\kappa)}=\pm 1}\left(1-\frac{\rho^4}{d^4}\right)\frac{\sin\phi}{\rho^2} \quad (3.17)$$

and

$$M_{bn}^{(\kappa')} = -\frac{\mu_0}{2\pi}\int_{\frac{n\pi}{2}+\frac{\pi}{4}-\frac{\phi}{2}}^{\frac{n\pi}{2}+\frac{\pi}{4}+\frac{\phi}{2}} \left(1-\frac{\rho^4}{d^4}\right)\frac{\cos 2\theta}{\rho^3}\,\rho d\theta = 0 \quad (3.18)$$

per unit length and unit quadrupole antenna moment. Finally, for the sextupole modes, the coupling inductances are

$$M_{bn}^{(\zeta)} = \frac{\mu_0}{2\pi}\int_{\frac{n\pi}{2}+\frac{\pi}{4}-\frac{\phi}{2}}^{\frac{n\pi}{2}+\frac{\pi}{4}+\frac{\phi}{2}} \left(1-\frac{\rho^6}{d^6}\right)\frac{\sin 3\theta}{\rho^4}\,\rho d\theta = \\ = \frac{\mu_0}{2\pi}\underbrace{\left(-\sin\frac{3n\pi}{2}+\cos\frac{3n\pi}{2}\right)}_{s_n^{(\zeta)}=\pm 1}\frac{\sqrt{2}}{3}\left(1-\frac{\rho^6}{d^6}\right)\frac{\sin\frac{3\phi}{2}}{\rho^3} \quad (3.19)$$

and

$$M_{bn}^{(\zeta')} = -\frac{\mu_0}{2\pi}\int_{\frac{n\pi}{2}+\frac{\pi}{4}-\frac{\phi}{2}}^{\frac{n\pi}{2}+\frac{\pi}{4}+\frac{\phi}{2}} \left(1-\frac{\rho^6}{d^6}\right)\frac{\cos 3\theta}{\rho^4}\,\rho d\theta = \\ = \frac{\mu_0}{2\pi}\underbrace{\left(\sin\frac{3n\pi}{2}+\cos\frac{3n\pi}{2}\right)}_{s_n^{(\zeta')}=\pm 1}\frac{\sqrt{2}}{3}\left(1-\frac{\rho^6}{d^6}\right)\frac{\sin\frac{3\phi}{2}}{\rho^3} \quad (3.20)$$

per unit length and unit sextupole antenna moment. It should be noted that for each field component the magnitude of the coupling is the same for all loops, but has different signs. Moreover, the sign functions s_x, s_y and s_κ are orthogonal. This will be used to separate the dipole and quadrupole signals by combining the output signals from the four antenna loops. For the sextupole mode, however, $s_n^{(\zeta)} \propto s_n^{(x)}$ and $s_n^{(\zeta')} \propto s_n^{(y)}$ (since n is an integer). This means that the influence of the sextupole moment can not be separated from the dipole signal. The sextupole mode coupling will therefore constitute a non-linear response to beam position. The couplings to the beam are plotted in Fig. 3.2.

3.3.3 Inductive Coupling Between Loops

The current induced in the antenna loop also give rise to a magnetic field. This field act back on the loop itself (self inductance) as well as on the other loops (mutual inductance). The effect can contribute significantly to the total transfer impedance of the pick-up, and has to be quantified.

By symmetry all loops have the same internal coupling parameters, so it is sufficient to study one loop. Assuming again that the pick-up is infinitely long, the field induced by the loop inside a conducting pipe of diameter d can be written as the sum of four source terms

$$\vec{B}_{\text{loop}}(x,y) = \\ = -\frac{\mu_0}{2\pi}\left(\frac{(x-\rho\cos\frac{\phi}{2})\,\hat{y}-(y-\rho\sin\frac{\phi}{2})\,\hat{x}}{(x-\rho\cos\frac{\phi}{2})^2+(y-\rho\sin\frac{\phi}{2})^2} - \frac{(x-\rho\cos\frac{\phi}{2})\,\hat{y}-(y+\rho\sin\frac{\phi}{2})\,\hat{x}}{(x-\rho\cos\frac{\phi}{2})^2+(y+\rho\sin\frac{\phi}{2})^2}\right) + \\ + \frac{\mu_0}{2\pi}\left(\frac{(x-\frac{d^2}{\rho}\cos\frac{\phi}{2})\,\hat{y}-(y-\frac{d^2}{\rho}\sin\frac{\phi}{2})\,\hat{x}}{(x-\frac{d^2}{\rho}\cos\frac{\phi}{2})^2+(y-\frac{d^2}{\rho}\sin\frac{\phi}{2})^2} - \frac{(x-\frac{d^2}{\rho}\cos\frac{\phi}{2})\,\hat{x}-(y+\frac{d^2}{\rho}\sin\frac{\phi}{2})\,\hat{y}}{(x-\frac{d^2}{\rho}\cos\frac{\phi}{2})^2+(y+\frac{d^2}{\rho}\sin\frac{\phi}{2})^2}\right) \quad (3.21)$$

where, for convenience, the coordinate system has been aligned so that the x axis cuts right through the loop (see Fig. 3.3). The first term is the field contribution of the current in the two loop wires, and the second term is the contribution of their image currents on the conducting chamber.

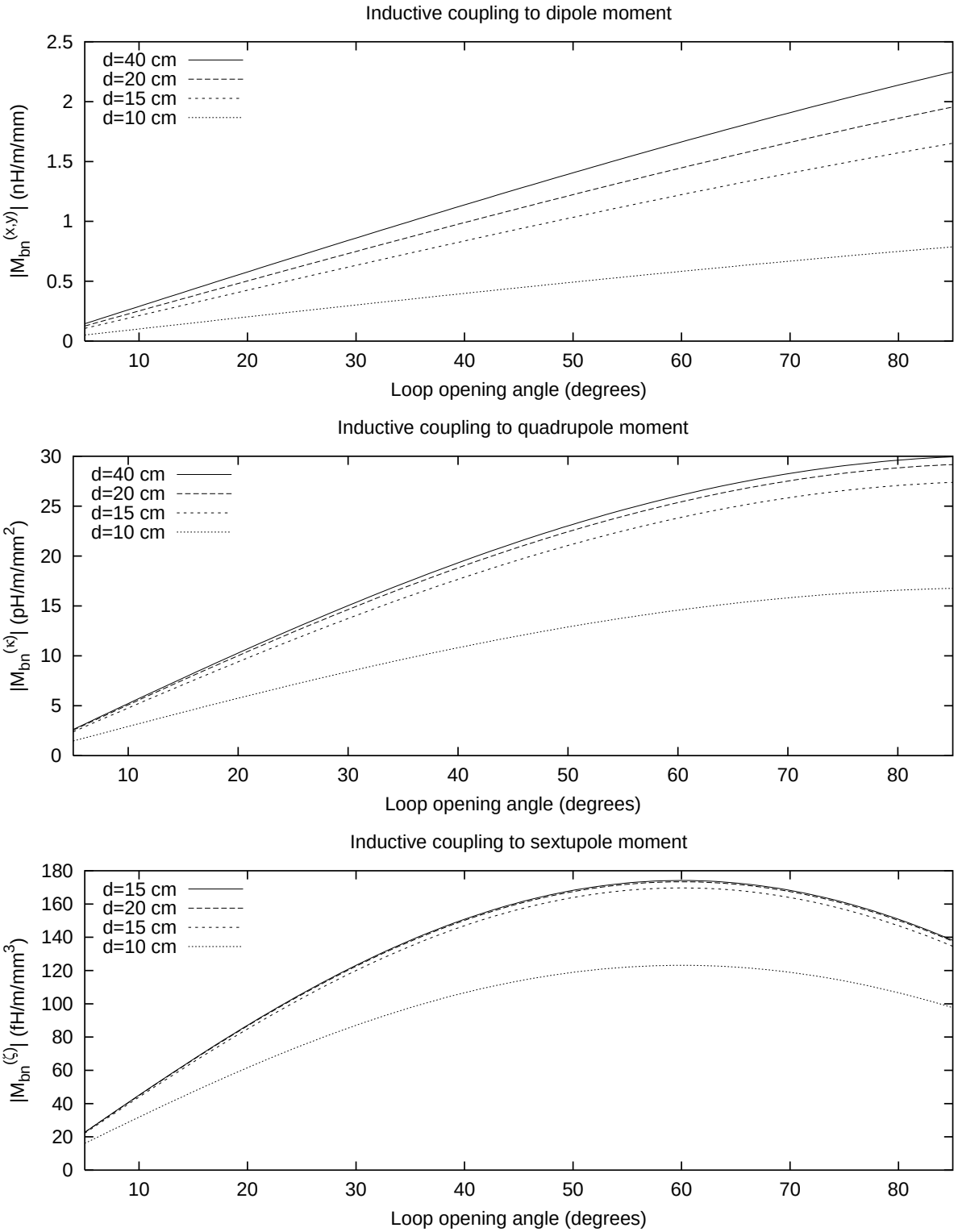

Figure 3.2: Analytical results for the inductive coupling from the beam to the antenna loop for dipole, quadrupole and sextupole moment (per unit pick-up length). The wire radius was 2 mm and the antenna position 8.15 cm. Results for some different positions d of the conducting boundary are shown.

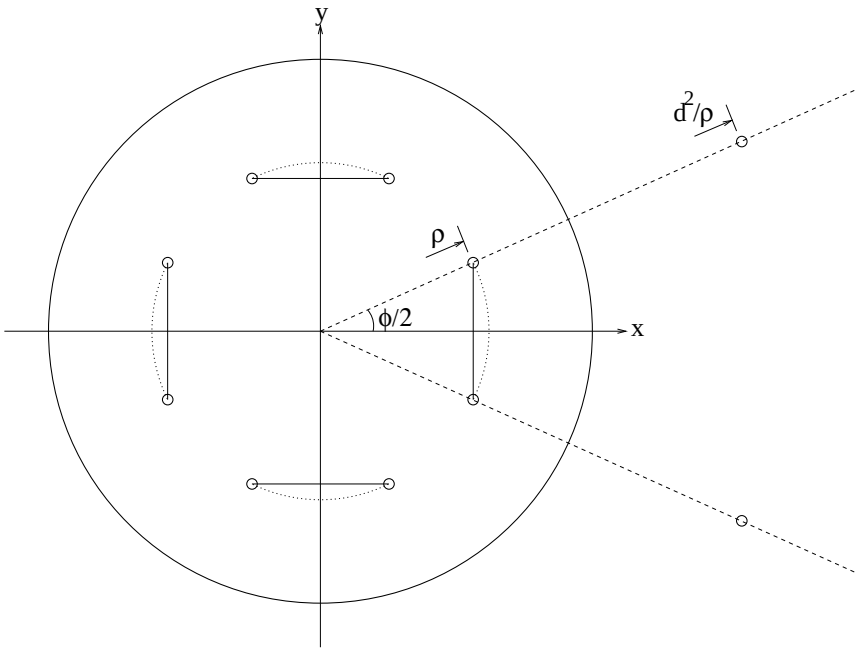

Figure 3.3: Geometry used to calculate the loop inductances. Since the total flux is independent of the integration path, the integration is performed along straight lines between loop wires (rather than following the curve of constant ρ) to simplify the calculation.

The loop self-inductance per unit length is then given by

$$M_{\text{self}} = \int_{-\rho\sin\frac{\phi}{2}}^{\rho\sin\frac{\phi}{2}} \vec{B}_{\text{loop}}(\rho\cos\frac{\phi}{2}, y)\cdot(-\hat{x})\,dy = \frac{\mu_0}{2\pi}\left(2\log\frac{2\rho\sin\frac{\phi}{2}-a}{a} + \log\frac{1-2\frac{\rho^2}{d^2}+\frac{\rho^4}{d^4}}{1-2\frac{\rho^2}{d^2}\cos\phi+\frac{\rho^4}{d^4}}\right) \quad (3.22)$$

where it is assumed that the antenna wire is perfectly conducting (no inner inductance). This allows to terminate the integration of the divergent source terms at the surface of the wire. The first term gives the self-inductance without conducting chamber, and the second the effect of the conducting chamber. The presence of the chamber reduces the loop inductance.

The mutual inductance between adjacent loops per unit length is given by

$$M_{\text{adj}} = \int_{-\rho\sin\frac{\phi}{2}}^{\rho\sin\frac{\phi}{2}} \vec{B}_{\text{loop}}(x, \rho\cos\frac{\phi}{2}) \cdot \hat{y}\, dx = \\ = \int_{\rho\sin\frac{\phi}{2}}^{-\rho\sin\frac{\phi}{2}} \vec{B}_{\text{loop}}(x, -\rho\cos\frac{\phi}{2}) \cdot (-\hat{y})\, dx = \\ = \frac{\mu_0}{4\pi}\left(2\log\frac{1}{\cos\phi} + \log\frac{1 + 2\frac{\rho^4}{d^4}\cos 2\phi + \frac{\rho^8}{d^8}}{1 + 2\frac{\rho^4}{d^4} + \frac{\rho^8}{d^8}}\right) \quad (3.23)$$

and the mutual inductance between opposite loops

$$M_{\text{opp}} = \int_{\rho\sin\frac{\phi}{2}}^{-\rho\sin\frac{\phi}{2}} \vec{B}_{\text{loop}}(-\rho\cos\frac{\phi}{2}, y) \cdot (-\hat{x})\, dy = \\ = \frac{\mu_0}{2\pi}\left(2\log\frac{1}{\cos\frac{\phi}{2}} + \log\frac{1 + 2\frac{\rho^2}{d^2}\cos\phi + \frac{\rho^4}{d^4}}{1 + 2\frac{\rho^2}{d^2} + \frac{\rho^4}{d^4}}\right) \quad (3.24)$$

Here as well, the first term gives the mutual inductance without chamber, and the second the effect of the conducting chamber. The presence of the chamber reduces the mutual loop inductances as well. Note that, in the above calculation, the reference direction is chosen inwards for the self inductance and outwards for the mutual inductances. This is done to obtain positive quantities, and the sign will be written out explicitly in later calculations. The various inductances are plotted in Fig. 3.4. The coupling factors $k_{\text{adj}} = M_{\text{adj}}/M_{\text{self}}$ and $k_{\text{opp}} = M_{\text{opp}}/M_{\text{self}}$, plotted in Fig. 3.5, are a measure of how correlated the currents in the two loops are. It can be seen that the coupling factor between adjacent loops become large for ϕ close to 90°.

It should be pointed out that it was assumed above that the current distribution on the antenna wire is uniform. This is not true in general, but the effect of a non-uniform distribution is small for a wire that is thin compared to the dimensions of the pick-up.

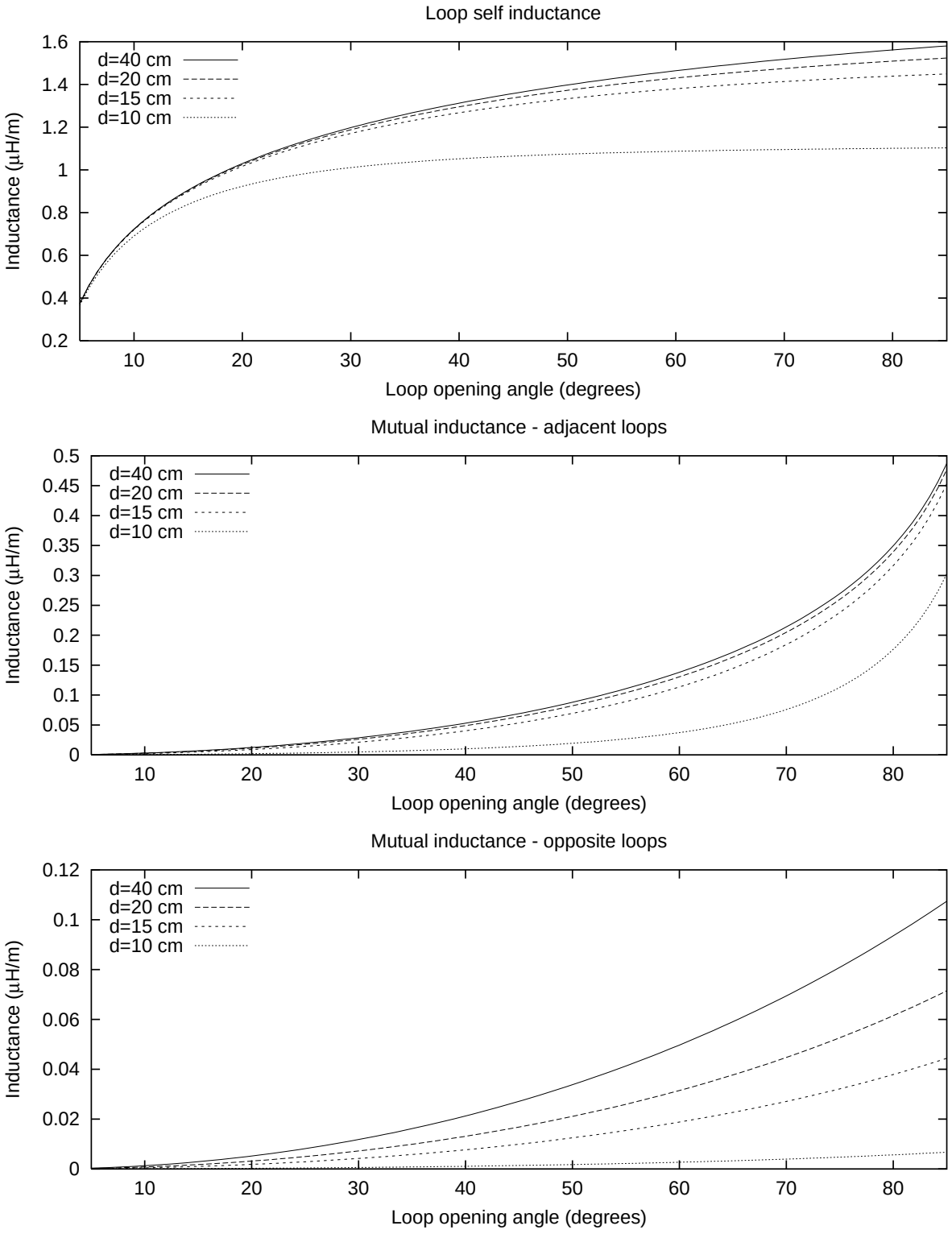

Figure 3.4: Analytic results for the mutual inductances (per unit pick-up length) between loops in the pick-up as a function of the antenna loop opening angle ϕ, for some different positions d of the conducting boundary. The wire radius was 2 mm and the antenna position 8.15 cm.

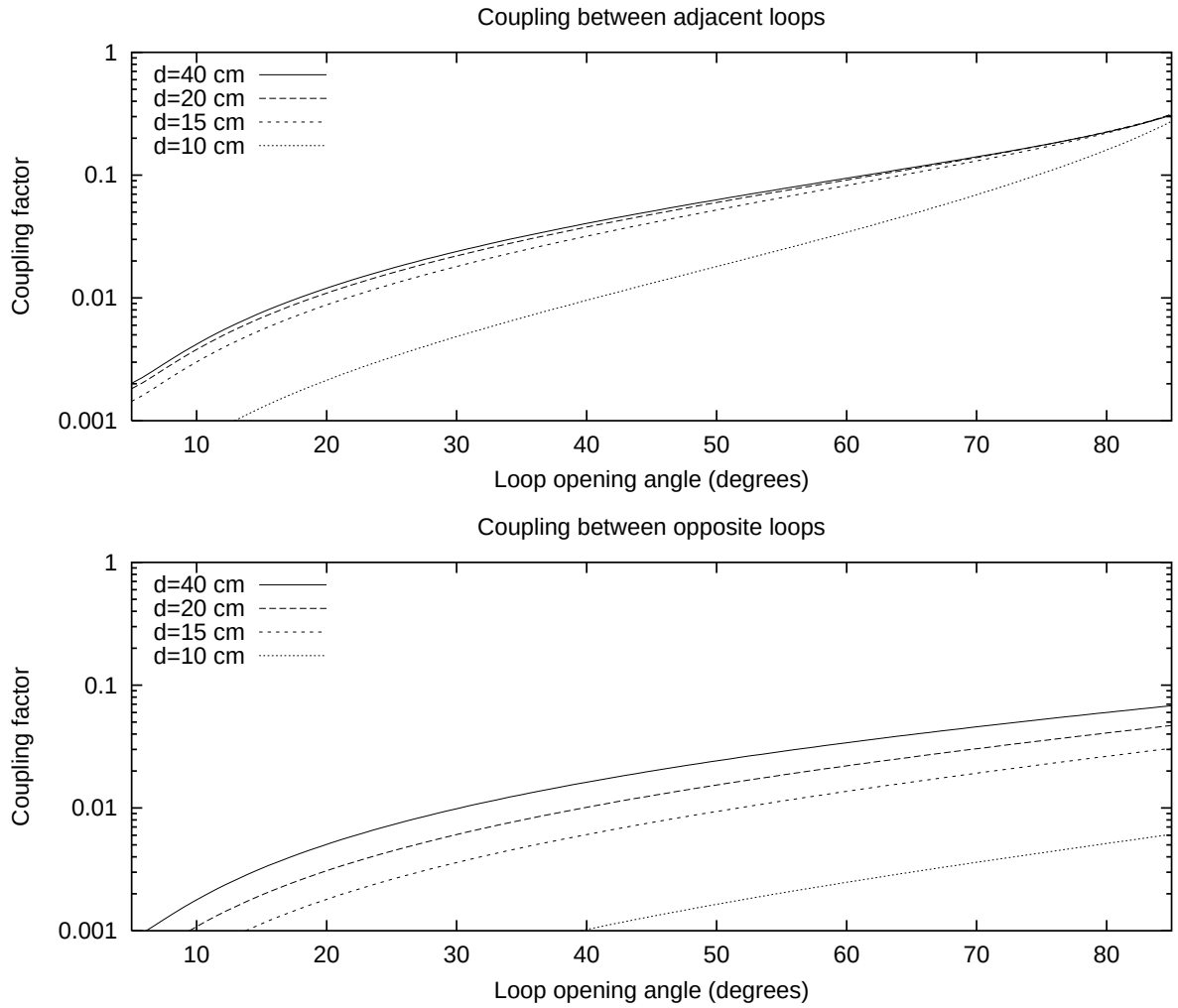

Figure 3.5: Coupling factors (ratio between mutual and self inductance) between loops in the pick-up, for some different positions d of the conducting boundary. The wire radius was 2 mm and the antenna position 8.15 cm.

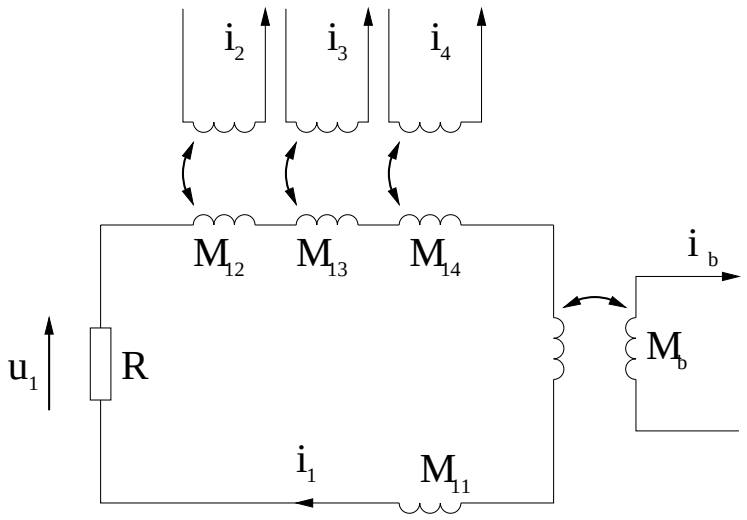

Figure 3.6: Simplified model of one loop in the pick-up, including the inductive coupling to the beam and between loops. The output signal is the voltage u over the load resistor.

3.3.4 Antenna Loop Transfer Impedances

To evaluate the effect of the inter-loop coupling on the transfer impedances, one can make an equivalent circuit of the antenna loops as in Fig. 3.6. The current i_1 in the circuit is given by the equation.

$$j\omega\, l\, M_{11}\, i_1 + i_1\, R - j\omega\, l\, M_{12}\, i_2 - j\omega\, l\, M_{13}\, i_3 - j\omega\, l\, M_{14}\, i_4 - j\omega\, l\, M_{\mathrm{b}1}\, i_{\mathrm{b}} = 0 \qquad (3.25)$$

where the pick-up length l has been introduced. The negative sign of the mutual inductances, due to the direction of the flux, are here written out explicitly. Due to symmetry, the circuit is the same for all loops, and the equations for the other loops can be obtained by simply shifting indices.

$$-j\omega\, l\, M_{21}\, i_1 + j\omega\, M_{22}\, i_2 + i_2\, R - j\omega\, l\, M_{23}\, i_3 - j\omega\, l\, M_{24}\, i_4 - j\omega\, l\, M_{\mathrm{b}2}\, i_{\mathrm{b}} = 0 \qquad (3.26)$$

$$-j\omega\, l\, M_{31}\, i_1 - j\omega\, l\, M_{32}\, i_2 + j\omega\, l\, M_{33}\, i_3 + i_3\, R - j\omega\, l\, M_{34}\, i_4 - j\omega\, l\, M_{\mathrm{b}3}\, i_{\mathrm{b}} = 0 \qquad (3.27)$$

$$-j\omega\, l\, M_{41}\, i_1 - j\omega\, l\, M_{42}\, i_2 - j\omega\, l\, M_{43}\, i_3 + j\omega\, l\, M_{44}\, i_4 + i_4\, R - j\omega\, l\, M_{\mathrm{b}4}\, i_{\mathrm{b}} = 0 \qquad (3.28)$$

Using the calculated inductances, this can be written in matrix form as

$$\begin{pmatrix} M_{\mathrm{self}} - j\frac{R}{l\omega} & -M_{\mathrm{adj}} & -M_{\mathrm{opp}} & -M_{adj} \\ -M_{\mathrm{adj}} & M_{\mathrm{self}} - j\frac{R}{l\omega} & -M_{\mathrm{adj}} & -M_{opp} \\ -M_{\mathrm{opp}} & -M_{\mathrm{adj}} & M_{\mathrm{self}} - j\frac{R}{l\omega} & -M_{\mathrm{adj}} \\ -M_{\mathrm{adj}} & -M_{\mathrm{opp}} & -M_{\mathrm{adj}} & M_{\mathrm{self}} - j\frac{R}{l\omega} \end{pmatrix} \cdot \begin{pmatrix} i_1 \\ i_2 \\ i_3 \\ i_4 \end{pmatrix} = \begin{pmatrix} M_{\mathrm{b}1} \\ M_{\mathrm{b}2} \\ M_{\mathrm{b}3} \\ M_{\mathrm{b}4} \end{pmatrix} i_{\mathrm{b}} \qquad (3.29)$$

which gives, when $M_{\mathrm{b}m} \to M_{\mathrm{b}m}^{(\kappa)}\,\kappa = s_m^{(\kappa)}|M_{\mathrm{b}m}^{(\kappa)}|\,\kappa$, the transfer impedance

$$Z_m^{(\kappa)} = \frac{i_m^{(\kappa)}\,R}{\kappa\,i_b} = \frac{s_m^{(\kappa)}\,|M_{bm}^{(\kappa)}|\,R}{M_{\mathrm{self}} + 2\,M_{\mathrm{adj}} - M_{\mathrm{opp}}} \cdot \frac{\omega}{\omega - j\omega_{\mathrm{lf}}^{(\kappa)}},$$

$$\omega_{\mathrm{lf}}^{(\kappa)} = \frac{R/l}{M_{\mathrm{self}} + 2\,M_{\mathrm{adj}} - M_{\mathrm{opp}}} \tag{3.30}$$

for the quadrupole moment, and similarly for the dipole moments

$$Z_m^{(x)} = \frac{i_m^{(x)}\,R}{x\,i_b} = \frac{s_m^{(x)}\,|M_{bm}^{(x)}|\,R}{M_{\mathrm{self}} + M_{\mathrm{opp}}} \cdot \frac{\omega}{\omega - j\omega_{\mathrm{lf}}^{(x)}}, \qquad \omega_{\mathrm{lf}}^{(x)} = \frac{R/l}{M_{\mathrm{self}} + M_{\mathrm{opp}}} \tag{3.31}$$

$$Z_m^{(y)} = \frac{i_m^{(y)}\,R}{y\,i_b} = \frac{s_m^{(y)}\,|M_{bm}^{(y)}|\,R}{M_{\mathrm{self}} + M_{\mathrm{opp}}} \cdot \frac{\omega}{\omega - j\omega_{\mathrm{lf}}^{(y)}}, \qquad \omega_{\mathrm{lf}}^{(y)} = \frac{R/l}{M_{\mathrm{self}} + M_{\mathrm{opp}}} \tag{3.32}$$

and sextupole moments

$$Z_m^{(\zeta)} = \frac{i_m^{(\zeta)}\,R}{\zeta\,i_b} = \frac{s_M^{(\zeta)}\,|M_{bm}^{(\zeta)}|\,R}{M_{\mathrm{self}} + M_{\mathrm{opp}}} \cdot \frac{\omega}{\omega - j\omega_{\mathrm{lf}}^{(\zeta)}}, \qquad \omega_{\mathrm{lf}}^{(\zeta)} = \frac{R/l}{M_{\mathrm{self}} + M_{\mathrm{opp}}} \tag{3.33}$$

$$Z_m^{(\zeta')} = \frac{i_m^{(\zeta')}\,R}{\zeta'\,i_b} = \frac{s_m^{(\zeta')}\,|M_{bm}^{(\zeta')}|\,R}{M_{\mathrm{self}} + M_{\mathrm{opp}}} \cdot \frac{\omega}{\omega - j\omega_{\mathrm{lf}}^{(\zeta')}}, \quad \omega_{\mathrm{lf}}^{(\zeta')} = \frac{R/l}{M_{\mathrm{self}} + M_{\mathrm{opp}}} \tag{3.34}$$

The transfer impedances are high pass filters, and the cut-off frequency for the quadrupole transfer impedance is different from that of the dipole and sextupole transfer impedances, due to the effect of the inter-loop coupling.

When written in the above form, the transfer impedance in the pass-band has no explicit dependence on the pick-up length. The cut-off frequency, however, depends on this length. But the low-frequency cut-off is usually a fixed design parameter, so it is useful to re-write the expressions for the transfer impedances on the form

$$Z_m^{(\cdot)} = s_m^{(\cdot)}|M_{bm}^{(\cdot)}|\,l\,\omega_{\mathrm{lf}}^{(\cdot)}\,\frac{\omega}{\omega - j\omega_{\mathrm{lf}}^{(\cdot)}} \tag{3.35}$$

It then appears as if the transfer impedance in the pass-band is linear in the pick-up length, and independent of the inter-loop couplings, if the cut-off frequency is required to be constant.

However, often the small load R is obtained by impedance transformation of another fixed load R_{out} (typically $50\,\Omega$). Then, $R = R_{\mathrm{out}}/N^2$, and the demand of a constant low frequency cut-off translates into the turns ratio N in the impedance transformer.

$$\omega_{\mathrm{lf}}^{(\cdot)} = \frac{R_{\mathrm{out}}/N^2/l}{M_{\mathrm{eff}}^{(\cdot)}} = \omega_0 \to N = \sqrt{\frac{R_{\mathrm{out}}/l}{\omega_0\,M_{\mathrm{eff}}^{(\cdot)}}} \tag{3.36}$$

where M_{eff} denotes the effective self impedance, including loop coupling effects. Taking into account that the transformer also increases the measured voltage by a factor N, the transfer impedance is then

$$Z_m^{(\cdot)} = s_m^{(\cdot)} |M_{bm}^{(\cdot)}| \sqrt{\frac{\omega_0 \, R_{\text{out}} \, l}{M_{\text{eff}}^{(\cdot)}}} \, \frac{\omega}{\omega - j\omega_0} \tag{3.37}$$

It can be seen from the expressions of the transfer impedances, since $M_{\text{adj}} > M_{\text{opp}}$, that the dipole transfer impedance has the highest cut-off frequency, and is therefore the limiting factor. The transfer impedances for constant dipole cut-off frequency $\omega_{\text{lf}}^{(x)}$ are plotted in Fig. 3.7 as functions of the loop opening angle ϕ. As expected, a large angle ϕ gives a stronger coupling to the beam. The dipole transfer impedance increases approximately linearly, whereas the quadrupole transfer impedance levels off and eventually drops. This behaviour of the quadrupole coupling is due to two things. The quadrupole inductance to the beam saturate for large angles, because the flux lines of the quadrupole field mode are concentrated in the centre of the antenna loops. Also, the mutual inductance between adjacent loop, which reduces the quadrupole transfer impedance, becomes large for large opening angles. Since strong inter-loop coupling also increases the sensitivity to misalignments, the opening angle of the loop should not be unnecessarily large. As the peak in the transfer impedance is rather broad, the angle can be chosen significantly smaller than the optimal value without much loss of sensitivity.

3.3.5 Pick-up Transfer Impedances

The transfer impedances for the full pick-up are obtained by summing the signals of the four loops, using the sign function $s_m^{(\cdot)}$ for the mode. The total transfer impedance to each loop is

$$Z_n = Z_n^{(x)} \, \bar{x} + Z_n^{(y)} \, \bar{y} + Z_n^{(\kappa)} \, \kappa + Z_n^{(\kappa')} \, \kappa' + Z_n^{(\zeta)} \, \zeta + Z_n^{(\zeta')} \, \zeta' + \ldots \tag{3.38}$$

and when summing the four loops using the sign functions of the different moments

$$Z_{\Delta_{\text{H}}} = \sum_{n=1}^{4} s_n^{(x)} \, Z_n = 4 \, |Z_n^{(x)}| \, \bar{x} + 4 \, |Z_n^{(\zeta)}| \, \zeta + \cdots = Z_{\Delta_{\text{H}}}^{(x)} \, \bar{x} + Z_{\Delta_{\text{H}}}^{(\zeta)} \, \zeta + \ldots \tag{3.39}$$

$$Z_{\Delta_{\text{V}}} = \sum_{n=1}^{4} s_n^{(y)} \, Z_n = 4 \, |Z_n^{(y)}| \, \bar{y} - 4 \, |Z_n^{(\zeta')}| \, \zeta' + \cdots = Z_{\Delta_{\text{V}}}^{(y)} \, \bar{y} - Z_{\Delta_{\text{V}}}^{(\zeta')} \, \zeta' + \ldots \tag{3.40}$$

$$Z_{\Xi} = \sum_{n=1}^{4} s_n^{(\kappa)} \, Z_n = 4 |Z_n^{(\kappa)}| \, \kappa + \cdots = Z_{\Xi}^{(\kappa)} \, \kappa + \ldots \tag{3.41}$$

where the pick-up transfer impedances $Z_{\Delta_{\text{H}}}^{(x)}$, $Z_{\Delta_{\text{V}}}^{(y)}$, $Z_{\Xi}^{(\kappa)}$, $Z_{\Delta_{\text{H}}}^{(\zeta)}$ and $Z_{\Delta_{\text{V}}}^{(\zeta')}$ have been introduced.

3.3.6 Pick-up Nonlinearity

Since the signal from the sextupole moment can not be separated from the dipole signal, it is interesting to understand what information this term contains. The definitions

$$\zeta = \iint (x^3 - 3xy^2)\, J(x,y)\, dx\, dy \tag{3.42}$$

$$\zeta' = \iint (3x^2y - y^2)\, J(x,y)\, dx\, dy \tag{3.43}$$

can be expanded as

$$\begin{aligned}\zeta = \bar{x}^3 - 3\,\bar{x}\,\bar{y}^2 + 3\,\bar{x}\,(\sigma_x^2 - \sigma_y^2) - 6\,\bar{y} \iint (x-\bar{x})(y-\bar{y})\, J(x,y)\, dx\, dy \\ - 3 \iint (x-\bar{x})(y-\bar{y})^2\, J(x,y)\, dx\, dy + \iint (x-\bar{x})^3\, J(x,y)\, dx\, dy\end{aligned} \tag{3.44}$$

$$\begin{aligned}\zeta' = 3\,\bar{y}\,\bar{x}^2 - \bar{y}^3 + 3\,\bar{y}\,(\sigma_x^2 - \sigma_y^2) + 6\,\bar{y} \iint (x-\bar{x})(y-\bar{y})\, J(x,y)\, dx\, dy \\ + 3 \iint (x-\bar{x})^2(y-\bar{y})\, J(x,y)\, dx\, dy - \iint (y-\bar{y})^3\, J(x,y)\, dx\, dy\end{aligned} \tag{3.45}$$

where the integrals represent higher order moments with respect to the beam centre, rather then the pick-up centre. These higher-order moments vanish if the beam is uncoupled (no x-y correlation) and symmetric around its centre. If these conditions are fulfilled, the pick-up transfer impedances can be written as

$$\Delta_{\mathrm{H}} = i_b\,\bar{x}\,\left(Z^{(x)}_{\Delta_{\mathrm{H}}} + Z^{(\zeta)}_{\Delta_{\mathrm{H}}}\,\left(\bar{x}^2 - 3\,\bar{y}^2 + 3\,(\sigma_x^2 - \sigma_y^2)\right) + \dots\right) \tag{3.46}$$

$$\Delta_{\mathrm{V}} = i_b\,\bar{y}\,\left(Z^{(y)}_{\Delta_{\mathrm{V}}} + Z^{(\zeta')}_{\Delta_{\mathrm{V}}}\,\left(\bar{y}^2 - 3\,\bar{x}^2 - 3\,(\sigma_x^2 - \sigma_y^2)\right) + \dots\right) \tag{3.47}$$

$$\Xi = i_b\left(Z^{(\kappa)}_{\Xi}\,(\bar{x}^2 - \bar{y}^2 + \sigma_x^2 - \sigma_y^2) + \dots\right) \tag{3.48}$$

As mentioned before, the sextupolar transfer impedance defines the non-linearity in the position response of Δ_{H} and Δ_{V}, and also their sensitivity to the beam sizes. It is interesting to note that the system of equations can, at least in a region where the non-linear terms are small, be solved numerically to obtain $\bar{x}$, $\bar{y}$ and $\sigma_x^2 - \sigma_y^2$. Another important remark is that, though some assumptions about the beam distribution was made to obtain the result for the Δ_{H} and Δ_{V}, the result for Ξ is independent of the beam distribution (apart from the neglected higher order terms).

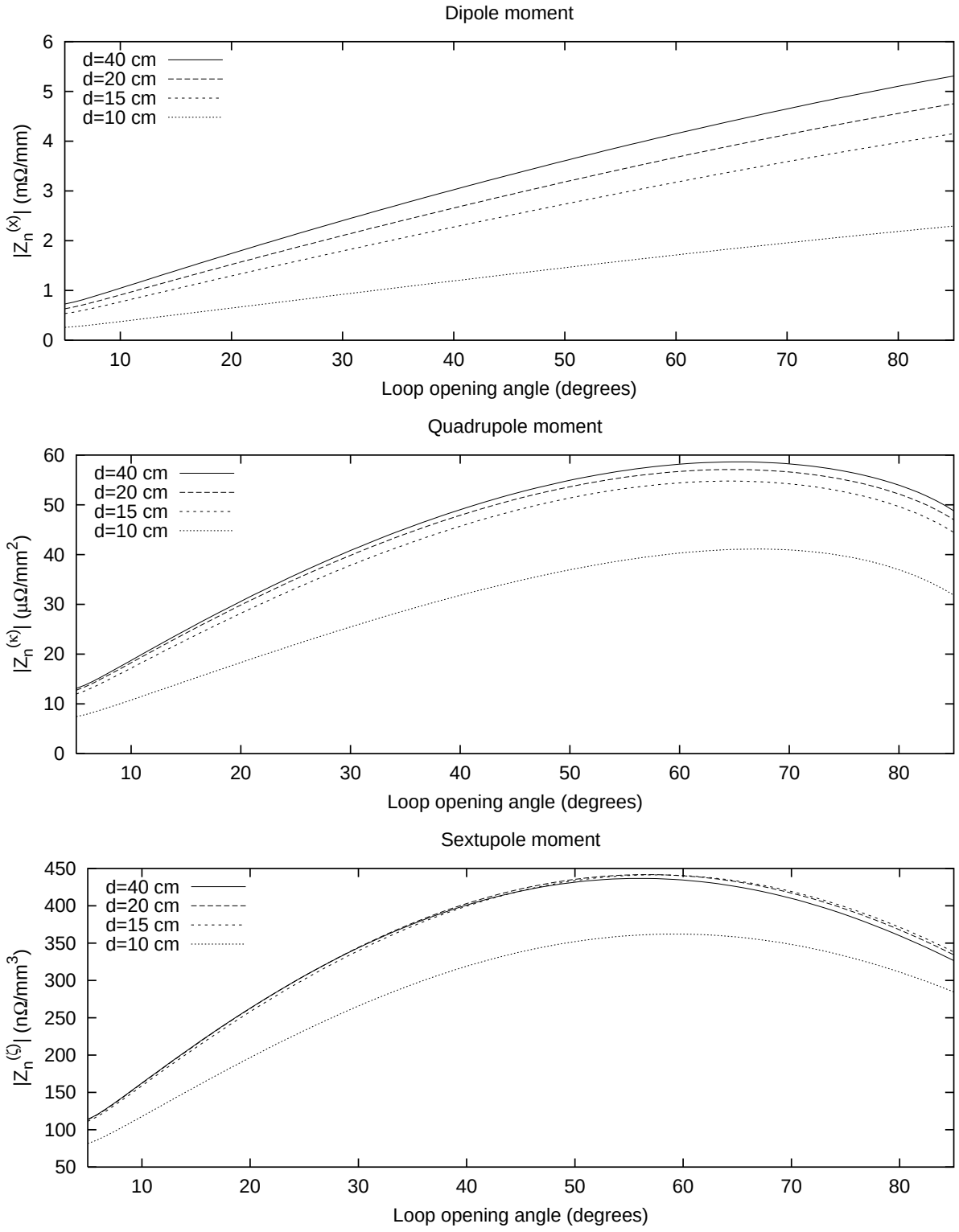

Figure 3.7: Analytic results for the transfer impedances corresponding to the different antenna moments as a function of the loop opening angle ϕ, with a fixed low frequency cut-off at 75 kHz for the dipole transfer impedance. The antenna wire radius was 2 mm and the loop situated at 8.15 cm from the centre. The active length of the pick-up was 40 cm. Results for some different positions ρ of the conducting boundary are shown.

3.3.7 The Effect to Alignment Errors

The loop wires can not be positioned with infinite precision. Alignment errors will reduce the theoretically infinite common mode rejection of the pick-up to a finite value. They influence the transfer impedance both by changing the direct coupling to the beam, and by changing the inter-loop couplings. If the loop coupling is relatively weak (small coupling factor), the dominating effect will come from the change in the direct beam coupling.

The change in the direct beam coupling due to a small displacement $\Delta\vec{x}$ of one of the antenna rods is given by

$$|\Delta M| = |\Delta\Phi| \approxeq |\vec{B} \times \Delta\vec{x}| \tag{3.49}$$

The largest parasitic effect naturally comes from the monopole components in the field expansion, since it is the strongest field component at the location of the loop. However, since this component is independent of beam position and dimensions, its effect is just to shift the zero level in the output signals. This can be rather easily corrected for, if the shifts are known from bench measurements. The parasitic effect from the dipole moments are worse in that respect, since they make the quadrupole signal dependent on position. This is much more complicated to correct for in the measured data. This term should therefore be kept very small.

"It is not enough to succeed.
Others must fail."

Gore Vidal

Chapter 4

Applications of Quadrupole Pick-ups

4.1 Understanding the Quadrupole Signal

4.1.1 Signal Components

The quadrupole moment κ of a beam measured by a quadrupole pick-up can be expanded in terms of its optical parameters as

$$\kappa = \sigma_x^2 - \sigma_y^2 + x^2 - y^2 = \underbrace{\varepsilon_x\beta_x - \varepsilon_y\beta_y}_{\text{betatron part}} + \underbrace{\sigma_p^2 D_x^2 - \sigma_p^2 D_y^2}_{\text{dispersion part}} + \underbrace{x^2 - y^2}_{\text{position part}} \tag{4.1}$$

assuming linear optics with no coupling between planes (in the case of coupling, the beta function is not well-defined). In a ring, the quadrupole moment of a beam can be measured over several consecutive turns. If the beam is initially misadapted in terms of Twiss functions, dispersion, position or injection angle, the value of κ will be oscillating. Using the known evolution of the different parameters as a function of machine turn, on can derive (see Appendix B)

$$\begin{aligned}\kappa_n = {} & \bar{\beta}_x(\varepsilon_x + \Delta\varepsilon_x) - \bar{\beta}_y(\varepsilon_y + \Delta\varepsilon_y) + \bar{D}_x^2\,\sigma_{\mathrm{p}}^2 + \bar{x}^2 - \bar{y}^2 \\ & + \bar{\beta}_x\left(\varepsilon_x\delta_{\beta_x}\cos(2\nu_x n - \phi_{\beta_x}) + \sigma_{\mathrm{p}}^2\delta_{D_x}^2\cos(2\nu_x n - 2\phi_{D_x}) + \delta_x^2\cos(2\nu_x n - 2\phi_x)\right) \\ & - \bar{\beta}_y\left(\varepsilon_y\delta_{\beta_y}\cos(2\nu_y n - \phi_{\beta_y}) + \sigma_{\mathrm{p}}^2\delta_{D_y}^2\cos(2\nu_y n - 2\phi_{D_y}) + \delta_y^2\cos(2\nu_y n - 2\phi_y)\right) \\ & + \sqrt{\bar{\beta}_x}\left(\sigma_{\mathrm{p}}^2 D_x\,\delta_{D_x}\cos(\nu_x n - \phi_{D_x}) + \bar{x}\,\delta_x\cos(\nu_x n - \phi_x)\right) \\ & - \sqrt{\bar{\beta}_y}\,\bar{y}\,\delta_y\sin(\nu_y n - \phi_y)\end{aligned} \tag{4.2}$$

where n is the number of machine revolutions. The terms have been ordered so that each line corresponds to one oscillation frequency. The first line contain the constant terms,

which corresponds to the steady state that will be reached once the oscillating part have been damped away (decohered). It differs from the steady state solution that would have been reached if the beam was matched by the emittance blow-up terms $\Delta\varepsilon_x$ and $\Delta\varepsilon_x$, which are given by

$$\Delta\varepsilon_x \approx \varepsilon_x \frac{{\delta_{\beta_x}}^2}{2} + \sigma_{\mathrm{p}}^2 \frac{{\delta_{D_x}}^2}{2} + \frac{{\delta_x}^2}{2} \tag{4.3}$$

$$\Delta\varepsilon_y \approx \varepsilon_y \frac{{\delta_{\beta_y}}^2}{2} + \sigma_{\mathrm{p}}^2 \frac{{\delta_{D_y}}^2}{2} + \frac{{\delta_y}^2}{2} \tag{4.4}$$

The second and third line in Eq. (4.2) are signal components oscillating at twice the horizontal and vertical betatron frequencies, respectively. Such an oscillation can be caused by all three kinds of mismatch: dispersion, betatron, and beam steering. The fourth and fifth lines are components at the betatron frequencies. They arise from dispersion mismatch or mistering, but only if the lattice dispersion and/or closed orbit is non-zero at the location of the pick-up. This is the reason for the absence of any vertical dispersion mismatch signal at the betatron frequency.

It is interesting to note that if the quadrupole pick-up also measures the beam position, its contribution to the quadrupole signal can be quantified and subtracted off on a turn-by-turn basis. When the beam position terms are suppressed, the signal component at the horizontal betatron frequency gives the horizontal dispersion mismatch. The dispersion mismatch can also be measured separately, by changing the beam momentum and recording the change in position. Once it is known, its contribution to the signal can be subtracted as well, and hence the betatron mismatch can be extracted from the phase and amplitude of the signals at twice the betatron frequencies.

4.1.2 Effects of Space Charge

Space charge effects modify the way the measured quadrupole moment behave as a function of machine turn. Notably, the oscillation frequencies will change. A very important point is that the beam width terms (betatron and dispersion) are sensitive to the direct space charge, whereas the frequencies of terms relating to beam position are sensitive only to the indirect space charge effect.

This means that the oscillation frequencies of the beam width terms are not the same as for the position terms. There is not even any *a priori* reason that the dispersion term and the betatron term should be shifted in frequency by the same amount. Individual particles contribute to the betatron signal as a function of their betatron amplitude, which is approximately independent of the longitudinal position of the particle in the bunch. The same particles contribute to the dispersion term as a function of its momentum offset. But particles with a high momentum offset are likely to be longitudinally close to the bunch centre and therefore see a higher space charge.

A practical consequence of this is that, in the presence of space charge, the dispersion term in the quadrupole moment can not be measured separately by changing the energy of

the beam and recording its displacement, since the propagation of off-momentum particles inside the beam is not the same as for an off-momentum beam.

The extra tune spread due to the direct space charge also make the decoherence of the beam width oscillations proceed much faster than the decoherence of a coherent beam oscillation.

4.2 Review of Previous Results

4.2.1 Emittance Measurement in LINACs

The first published experimental results using quadrupole pick-ups were produced at SLAC[26]. R. Miller et al used the quadrupole signal from strip-line position pick-ups spaced regularly in the lattice of the Linear Collider (SLC) to determine the emittance and Twiss parameters of the electron beam.

In the absence of dispersion, the quadrupole moment κ measured by the pick-up is given by

$$\kappa - \bar{x}^2 + \bar{y}^2 = \sigma_x^2 - \sigma_y^2 = \beta_x \varepsilon_x - \beta_y \varepsilon_y \tag{4.5}$$

where the position terms have been moved to the left to indicate that it is assumed that their contribution is subtracted. The Twiss beta function at the pick-up can be related to the Twiss parameters at an arbitrary upstream point (denoted with subset zero) as

$$\beta = C^2\,\beta_0 - 2\,S\,C\,\alpha_0 + S^2\,\gamma_0 \tag{4.6}$$

where S and C are components of the transfer matrix from the reference point to the location of the pick-up. Hence,

$$\kappa = C_x^2\,\beta_{x0}\,\varepsilon_x - 2\,S_x\,C_x\,\alpha_{x0}\,\varepsilon_x + S_x^2\,\gamma_{x0}\,\varepsilon_x - C_y^2\,\beta_{y0}\,\varepsilon_y + 2\,S_y\,C_y\,\alpha_{y0}\,\varepsilon_y - S_y^2\,\gamma_{y0}\,\varepsilon_y \tag{4.7}$$

and with several pick-ups available, one can build a matrix equation of the form

$$\vec{k} = A \cdot \vec{e} \tag{4.8}$$

where the vector $\vec{k}$ contains the measured quadrupole moments corrected for beam position

$$\vec{k} = \begin{pmatrix} \kappa_1 - \bar{x}_1^2 + \bar{y}_1^2 \\ \kappa_2 - \bar{x}_2^2 + \bar{y}_2^2 \\ \vdots \\ \kappa_n - \bar{x}_n^2 + \bar{y}_n^2 \end{pmatrix} \tag{4.9}$$

and $\vec{e}$ is the six-component vector containing the emittance and Twiss parameters at the reference point

$$\vec{e} = \begin{pmatrix} \beta_{x0}\,\varepsilon_x \\ \alpha_{x0}\,\varepsilon_x \\ \gamma_{x0}\,\varepsilon_x \\ \beta_{y0}\,\varepsilon_y \\ \alpha_{y0}\,\varepsilon_y \\ \gamma_{y0}\,\varepsilon_y \end{pmatrix} \tag{4.10}$$

If six or more independent measurements are available, the matrix equation can be inverted (or solved in the least square sense) to obtain $\vec{e}$. Then, the relation between the Twiss parameters

$$\gamma = \frac{1+\alpha^2}{\beta} \tag{4.11}$$

can be used to calculate the emittances, that are given by

$$\varepsilon_x = \sqrt{e_1 e_3 - e_2^2}, \qquad \varepsilon_y = \sqrt{e_4 e_6 - e_5^2} \tag{4.12}$$

and the Twiss parameters then follow trivially as

$$\beta_x = \frac{e_1}{\sqrt{e_1 e_3 - e_2^2}}, \qquad \alpha_x = \frac{e_2}{\sqrt{e_1 e_3 - e_2^2}} \tag{4.13}$$

$$\beta_y = \frac{e_4}{\sqrt{e_4 e_6 - e_5^2}}, \qquad \alpha_y = \frac{e_5}{\sqrt{e_4 e_6 - e_5^2}} \tag{4.14}$$

$$\tag{4.15}$$

More recently, the SLAC experiment was repeated at Los Alamos, to measure the emittance of electron beams from the Advanced Free Electron Laser[40] and the Sub-Picosecond Accelerator[48, 49, 28, 50]. In both cases quadrupole pick-ups were used as measurement tools since they measure the true second moment of the beam, without assumptions on the beam distribution. This was important since the electron beams considered were non-thermalised and highly non-Gaussian.

It was realised that in many cases, the matrix A obtained is numerically very ill-conditioned[51]. This makes the measurement sensitive to both measurement errors and errors in the matrix itself, which are unavoidable due to limited knowledge of the optics. This problem could be reduced by optimising the pick-up locations and the intermediate optics. In practice, this was done using a single pick-up, by changing the optics of the line between shots. This solution is, however, incompatible with parasitic emittance measurement.

4.2.2 Energy Spread Measurement in Rings

In the SLC damping rings, strip-line position pick-ups have been used to minimise the energy spread of the injected LINAC beam[27]. In this case, the pick-ups were placed in positions with large horizontal dispersion. As in the previous case, the quadrupole moment was measured for a single bunch and the position contribution subtracted, yielding

$$\kappa - \bar{x}^2 + \bar{y}^2 = \sigma_x^2 - \sigma_y^2 = \beta_x \varepsilon_x - \beta_y \varepsilon_y + D_x^2 \sigma_{\mathrm{p}}^2 \tag{4.16}$$

Keeping the emittance constant, the RF phase was then varied to find the minimum of the signal, which corresponds to the smallest momentum spread. An absolute value of the momentum spread was not extracted from the measurement.

4.2.3 Study of Beam Size Oscillations in Rings

Measurements of beam size oscillations in a circular machine using quadrupole pick-ups were first performed in the Anti-proton Accumulator (AA) at CERN. By observing certain frequency components in the quadrupole signal, it was possible to diagnose transverse quadrupole instabilities that were causing beam loss in the coasting, unbunched beam[29]. The pick-up used for this was an existing resonant vertical pick-up, where the two plates had been coupled in common mode and made resonant at the quadrupole frequency (twice the betatron frequency) and the signal from the pick-up was studied using a spectrum analyser in fixed frequency receiver mode. Since the beam was unbunched, the common-mode signal filtered out by the high-pass characteristic of the pick-up, and was therefore not a problem.

The stability of the beam against quadrupole excitations was also studied by measuring the quadrupole beam transfer function. This was done by exciting the beam with a quadrupole kicker and measure the response as a function of frequency. The same type of measurement were later made also in the Low Energy Anti-proton Ring (LEAR)[31].

The use of quadrupole pick-ups in the AA was further extended to determine and correct injection mismatch by measuring the phase and amplitude of the beam width oscillations it causes[30]. For this, a non-resonant electrostatic pick-up was used. Common-mode rejection was a big issue, since the beam was bunched and therefore gave very strong signal components at the revolution frequency harmonics. To overcome the problem, the signal was again analysed in frequency domain using spectrum analysers in receiver mode, making use of the frequency separation between quadrupole and common-mode signals to suppress the common-mode.

The corrections of the measured mismatch were made empirically, by measuring the response of deliberate quadrupole perturbations and use this information to calculate corrections. The beam position contribution was not corrected for, so the beam had to be carefully steered to keep this contribution smaller than the beam size oscillations that were measured.

Similar measurement have since been performed in the Anti-proton Accumulator at Fermilab[52].

4.2.4 Discussion on Previous Results

A few general remarks can be made on the previously reported use of quadrupole pick-ups. First, there is a quite clear separation in the signal analysis between LINACs and rings. In LINACs, the data has been analysed in time domain (single bunch), which is imperative since the beam passes only once, whereas in circular machines the data was studied in frequency domain (with the exception of the SLC damping rings). Single-bunch treatment makes it possible to subtract the contribution of the beam position to obtain the quadrupole moment with respect to the beam centre, from which the emittance can be calculated if enough data is available.

The reason why single bunch treatment was so far not attempted a ring was probably that the ratio between aperture and beam-size generally is larger in rings than in LINACs. Therefore, it is much harder to obtain a sufficient common-mode rejection in rings. Hence the need for a frequency analysis to separate the oscillating quadrupole signal from the common-mode.

Apart from this problem, the single bunch emittance measurement method developed at SLAC is easily adaptable for circular machines.

4.3 Further Possible Applications in Rings

4.3.1 Measurement of Steady-State Emittance

Using two pick-ups

If two pick-ups are available in the machine, and the circulating beam is stable, the two pick-up signals are constant and given by

$$\kappa_1 - \bar{x}_1^2 + \bar{y}_1^2 = \sigma_{x1}^2 - \sigma_{y1}^2 = \epsilon_x \beta_{x1} - \epsilon_y \beta_{y1} \tag{4.17}$$

$$\kappa_2 - \bar{x}_2^2 + \bar{y}_2^2 = \sigma_{x2}^2 - \sigma_{y2}^2 = \epsilon_x \beta_{x2} - \epsilon_y \beta_{y2} \tag{4.18}$$

assuming that there is no dispersion. The equations can be written in matrix form as

$$\begin{pmatrix} \kappa_1 - \bar{x}_1^2 + \bar{y}_1^2 \\ \kappa_2 - \bar{x}_2^2 + \bar{y}_2^2 \end{pmatrix} = \begin{pmatrix} \beta_{x1} & -\beta_{y1} \\ \beta_{x2} & -\beta_{y2} \end{pmatrix} \cdot \begin{pmatrix} \epsilon_x \\ \epsilon_y \end{pmatrix} \tag{4.19}$$

In order for the matrix equation to be numerically stable, it should be as diagonal as possible, i.e. $\beta_{x1} \gg \beta_{y1}$ and $\beta_{y2} \gg \beta_{x2}$. The solution to the system of equations is given by

$$\epsilon_x = \frac{-\beta_{y2}(\kappa_1 - \bar{x}_1^2 + \bar{y}_1^2) + \beta_{y1}(\kappa_2 - \bar{x}_2^2 + \bar{y}_2^2)}{\beta_{y1}\beta_{x2} - \beta_{x1}\beta_{y2}} \tag{4.20}$$

$$\epsilon_y = \frac{-\beta_{x2}(\kappa_1 - \bar{x}_1^2 + \bar{y}_1^2) + \beta_{x1}(\kappa_2 - \bar{x}_2^2 + \bar{y}_2^2)}{\beta_{y1}\beta_{x2} - \beta_{x1}\beta_{y2}} \tag{4.21}$$

Thus, measuring the emittance of a stable circulating beam with quadrupole pick-ups is theoretically straightforward.

The statistical error due to statistical fluctuations in the measurement of κ can be reduced by averaging over many consecutive beam passages. The dominating errors will therefore be systematic, coming from offsets in the pick-ups and errors in the beta functions. These can be reduced e.g. by measuring the ratios β_{x1}/β_{x2} and β_{y1}/β_{y2} by comparing the amplitude of coherent oscillations measured by the two pick-ups. Also, if there is a non-zero dispersion at the pick-up locations, its contribution has to be subtracted from the measured quadrupole moments. If the correction is large, errors in the dispersion and momentum spread can contribute significantly to the systematic errors.

These error sources are the same as for any other measurement of stable-beam emittance, and the accuracy can therefore be expected to be comparable to these methods.

Using three pick-ups

If three pick-ups are available in a circular machine

$$\kappa_1 - \bar{x}_1^2 + \bar{y}_1^2 = \epsilon_x\beta_{x1} - \epsilon_y\beta_{y1} + D_{x1}^2\sigma_{\mathrm{p}}^2 \tag{4.22}$$

$$\kappa_2 - \bar{x}_2^2 + \bar{y}_2^2 = \epsilon_x\beta_{x2} - \epsilon_y\beta_{y2} + D_{x2}^2\sigma_{\mathrm{p}}^2 \tag{4.23}$$

$$\kappa_3 - \bar{x}_3^2 + \bar{y}_3^2 = \epsilon_x\beta_{x3} - \epsilon_y\beta_{y3} + D_{x3}^2\sigma_{\mathrm{p}}^2 \tag{4.24}$$

where the dispersion also has been included. In matrix form, the equation is

$$\begin{pmatrix} \kappa_1 - \bar{x}_1^2 + \bar{y}_1^2 \\ \kappa_2 - \bar{x}_2^2 + \bar{y}_2^2 \\ \kappa_3 - \bar{x}_3^2 + \bar{y}_3^2 \end{pmatrix} = \begin{pmatrix} \beta_{x1} & -\beta_{y1} & D_{x1}^2 \\ \beta_{x2} & -\beta_{y2} & D_{x2}^2 \\ \beta_{x3} & -\beta_{y3} & D_{x3}^2 \end{pmatrix} \cdot \begin{pmatrix} \epsilon_x \\ \epsilon_y \\ \sigma_{\mathrm{p}}^2 \end{pmatrix} \tag{4.25}$$

which can be solved for the emittances and the momentum spread if the matrix is non-singular. Again, the matrix should be as orthogonal as possible for a numerically stable implementation. Since the beta functions are always positive, the best solution is to have $\beta_{x1} \gg \beta_{y1}$, $\beta_{y2} \gg \beta_{x2}$ $D_{x1} = D_{x2} = 0$, $D_{x3}^2 \gg \beta_{x3}$ and $D_{x3}^2 \gg \beta_{y3}$. This would make the matrix near-diagonal, but these conditions might not be easy to satisfy in practice. As in the previous case, random errors can be suppressed by averaging over many turns, so systematic errors arising from erroneous input parameters are the main issue for the accuracy of the measurement.

4.3.2 Measuring Emittance and Matching by Matrix Inversion

As already pointed out, the SLAC method can be directly applied in rings if the quadrupole moment of the beam can be measured on a single-bunch basis. This measurement would only be necessary at injection, since after filamentation the beam is stable and the previously discussed method can be used. An advantage in a ring is that since the beam is circulating, each pick-up can be used several times on the same bunch, so six separate pick-ups are not necessary. However, at least two pick-ups are needed to disentangle the

horizontal and vertical contributions. In order to make the matrix A as well-conditioned as possible, one pick-up should be be positioned at a location with a large horizontal and small vertical beta function and the other at a location where the opposite applies, just as for the emittance measurement on a stable beam discussed before.

Another important advantage with performing the measurement in a ring is that the matrix A is a function of only a few parameters, namely the beta function at the pick-ups, their separation in phase, and the machine tunes[1]. The tunes and the pick-up phase separations can be determined experimentally by measuring phase differences and frequency of coherent oscillations in the two planes. Similarly, in each plane, the ratio of beta functions at the two pick-ups can be determined, as pointed out previously. There are therefore only two parameters, namely the horizontal and vertical beta function at one of the pick-ups, that needs to be taken from theory or a separate measurement The uncertainties in the matrix A should therefore be less than in the LINAC case.

The optimum positioning of the two pick-ups needed would be the same as in the previous case in terms of beta functions. Moreover, if the phase advance between pick-ups is a multiple of 90°, the phase term between the two pick-ups vanishes, leading to a partial de-coupling of the matrix equation. The 90° phase separation is, however, not a requirement.

4.3.3 Measuring Emittance and Matching using a Model Fit

Although the matrix inversion method is a good idea, it has some drawbacks. It is not straightforward to include dispersion and momentum spread measurement in the method, as the dispersion term transforms in a different way than the betatron term, so the dispersion contribution to the beam width have to be measured separately. As discussed previously, this is not straightforward in the presence of space charge. Another problem linked to space charge is that the tune used in constructing the matrix should be the tune of particles inside the bunch. But this tune is different from the tune measured from coherent beam oscillations.

The best way to determine this tune is from the oscillations themselves. This can be done if the emittances and matching parameters are determined by fitting the expected beam signals to the data with variable tunes, rather than using the matrix method that uses fixed tunes. In such a fit, it is also possible to include the horizontal dispersion in the analysis. The sensitivity to noise is slightly increased with a fit method, since there are more degrees of freedom as compared to the matrix inversion method.

This method can be regarded as an extension to the previously discussed method for stable beams, since the emittances, and if possible the momentum spread, are determined from the constant part of the signals, while the various mismatches are given by the oscillating part. If the lattice dispersion is non-zero, the horizontal dispersion can be separated from the horizontal betatron mismatch using the signal at the betatron frequency. It is, however, not possible to disentangle a vertical dispersion mismatch from a vertical

[1]The matrix also depend on the Twiss alpha, but this is zero in straight section of the CPS machine.

betatron mismatch, due to the lack of non-zero vertical lattice dispersion in conventional rings. Fortunately, unless the injection line has large vertical bending magnets, one does not expect a significant vertical dispersion mismatch.

If two pick-ups are available, where at least one is at a location of non-zero lattice dispersion, the emittances, betatron mismatches and the horizontal dispersion mismatch can be determined with this method, if the momentum spread is known. With three pick-ups, properly located, also the momentum spread can be determined. The requirements on pick-up locations are in principle the same as in the previous sections.

4.3.4 Measurement of Coupling

In an uncoupled machine the transverse beam characteristics are given by the second order moments in horizontal and vertical phase space

$$\langle x^2 \rangle, \quad \langle x\, x' \rangle, \quad \langle x'^2 \rangle, \quad \langle y^2 \rangle, \quad \langle x\, y' \rangle, \quad \langle y'^2 \rangle. \tag{4.26}$$

If there is coupling between the planes, the motion in the two planes can not be separated, and a four-dimensional transverse phase space notation is needed. Therefore, the extra moments

$$\langle x\, y \rangle, \quad \langle x\, y' \rangle, \quad \langle x'\, y \rangle, \quad \langle x'\, y' \rangle, \tag{4.27}$$

are required to characterise the beam. One of these coupled moments can be measured directly with a skew quadrupole pick-up, since the skew quadrupole moment is given by

$$\kappa' = 2\langle x\, y \rangle \tag{4.28}$$

This moment is gives the tilt angle of the beam ellipse in real space, which can be used to quantify the coupling.

In a coupled machine, injection matching becomes more complicated, since it is not sufficient to match the beam in each plane separately. In particular, if an uncoupled beam is injected into a coupled machine, it is always mismatched. A signature of coupling mismatch is coherent beam width oscillations occurring at the beating frequency between the two normal modes of oscillation. This can be observed with a normal quadrupole pick-up.

4.4 Implementation in the PS machine

4.4.1 Pick-up Locations

The lattice of the CPS is a FOFDOD[2] lattice with 10 super-periods of 10 FD magnets each. The beta function, plotted in Fig. 4.1, is almost constant in the drift spaces between

[2]FOFDOD defines the magnet sequence, where F stands for focusing quadrupole, D for defocusing quadrupole and O for straight section

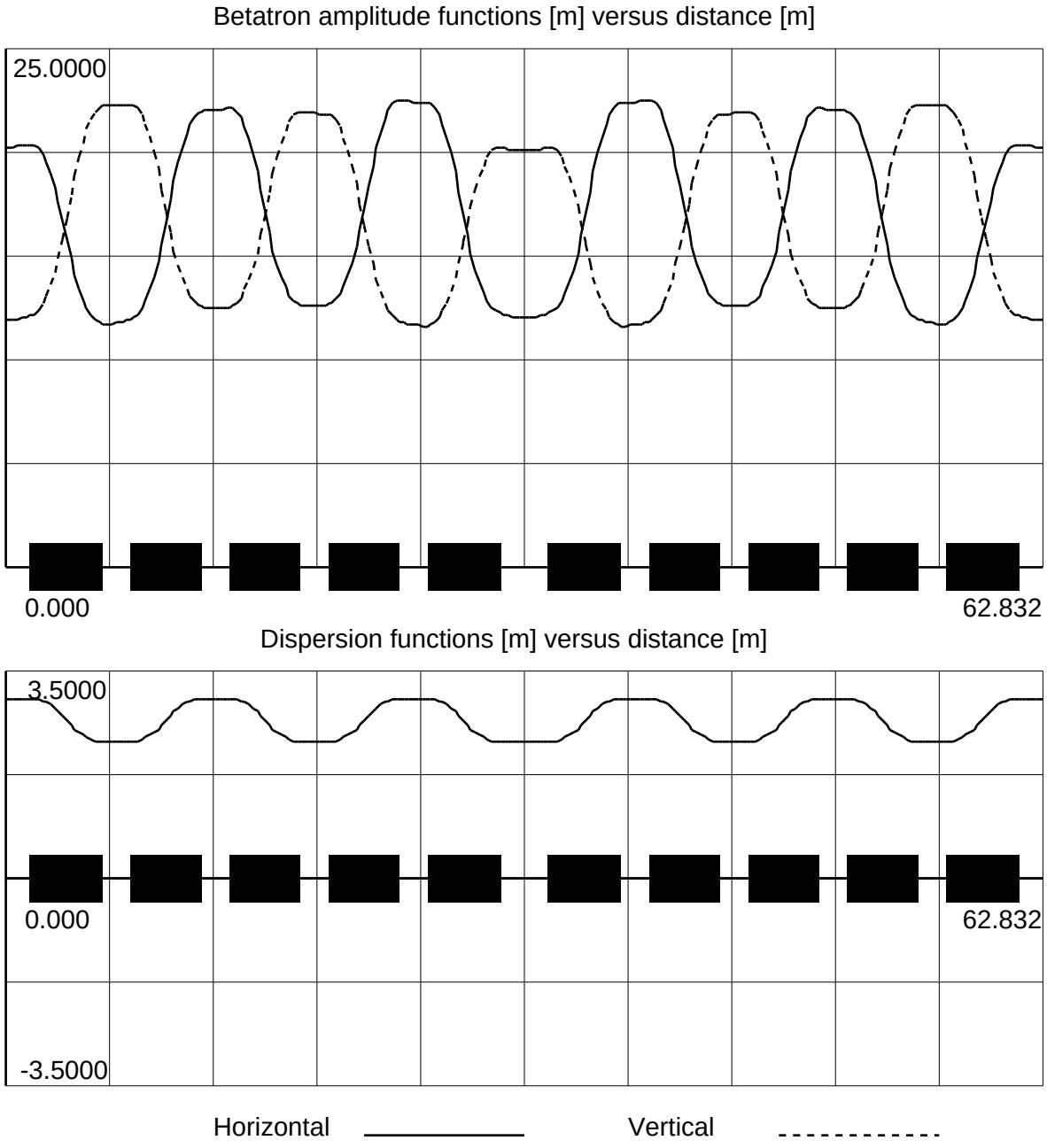

Figure 4.1: Lattice Twiss and dispersion functions for one super-period of the PS machine. The blocks show the position of the combined function magnets.

magnets, with alternating large and small values in consecutive sections. When the horizontal beta is large, the vertical is small and vice versa. Since there are only two groups of locations, odd and even straight sections, with significantly different optical parameters, it does not make sense to install more that two pick-ups in the machine. However, these two locations comply with the requirements for different beta functions. Moreover, the nearly flat beta function in the straight section means that the beam cross section is constant in the pick-ups. It was found best to install the two pick-ups in consecutive straight sections, since by minimising the distance and the number of magnets between the pick-ups, their separation in betatron phase becomes almost insensitive to the variations in the machine tune due, e.g. to space charge.

4.4.2 Error sensitivity

A comparative study of the fit and matrix method for measuring emittance and matching was performed for the setup in the PS. Reconstructing the emittances and Twiss parameters from simulated data with random errors show that both methods perform quite well.

There is not a clear cut winner between the two. When $Q_x = Q_y = 6.25$, both methods fail. This is because the quadrupole moment has a periodicity of 2 turns, yielding only four independent measurements, which is not enough to determine all the free parameters. When the tunes in the two planes are exactly equal, the fit method sometimes fail to converge to the right tune in one of the planes. The result is a systematic error in the matching only. For most combinations of tunes the methods perform approximately equally well (see Fig. 4.2). However, if the space charge detuning is large, or the tunes in the matrix is wrong for another reason, the matrix method give large systematic errors. This is seen in both the emittance and Twiss parameters In this case, the fit method is superior.

An analytical study of the error sensitivity of the matrix method based on singular value decomposition is given in Appendix C. It yields a statistical r.m.s. error in the measured emittance of $\sigma_\varepsilon = 0.015\,\mu$m for the PS setup, if the noise level in the measured quadrupole moment is $0.5\,\text{mm}^2$ and data from six machine turns are used in the analysis. This fits well with the simulations. The small value again indicates that systematic errors, due e.g. to pick-up offsets and input parameters, will dominate the final error.

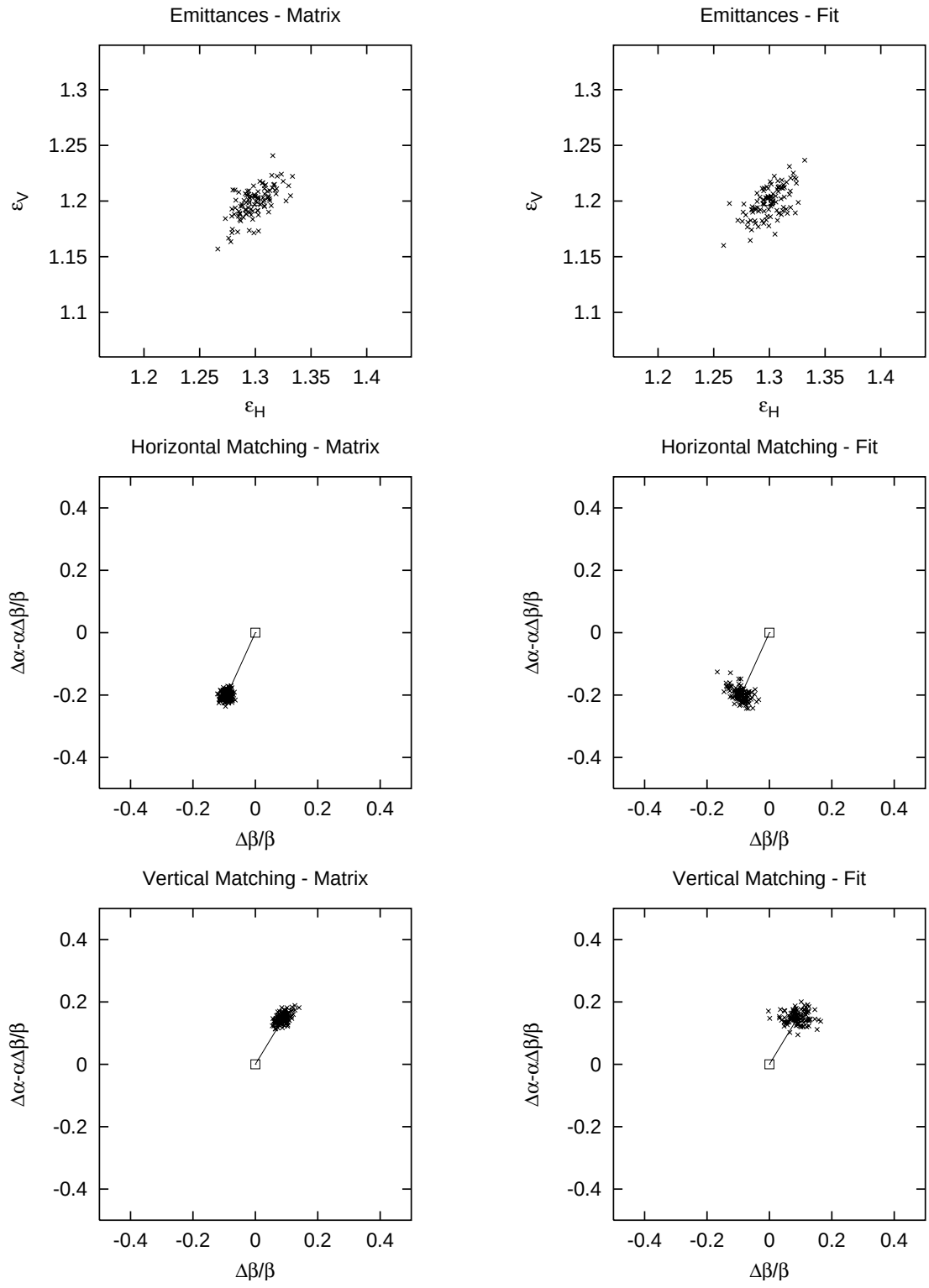

Figure 4.2: Analysis of simulated data with matrix and fit method. Data from six machine turns were used. Tunes: $Q_x = 0.200$, $Q_y = 0.190$. Noise level in quadrupole moment (r.m.s.): σ_κ=0.5 mm^2. No space charge detuning. The emittance should be in the centre of the graphs, and the mismatch at the end of the indicated line. Both methods perform about equally well.

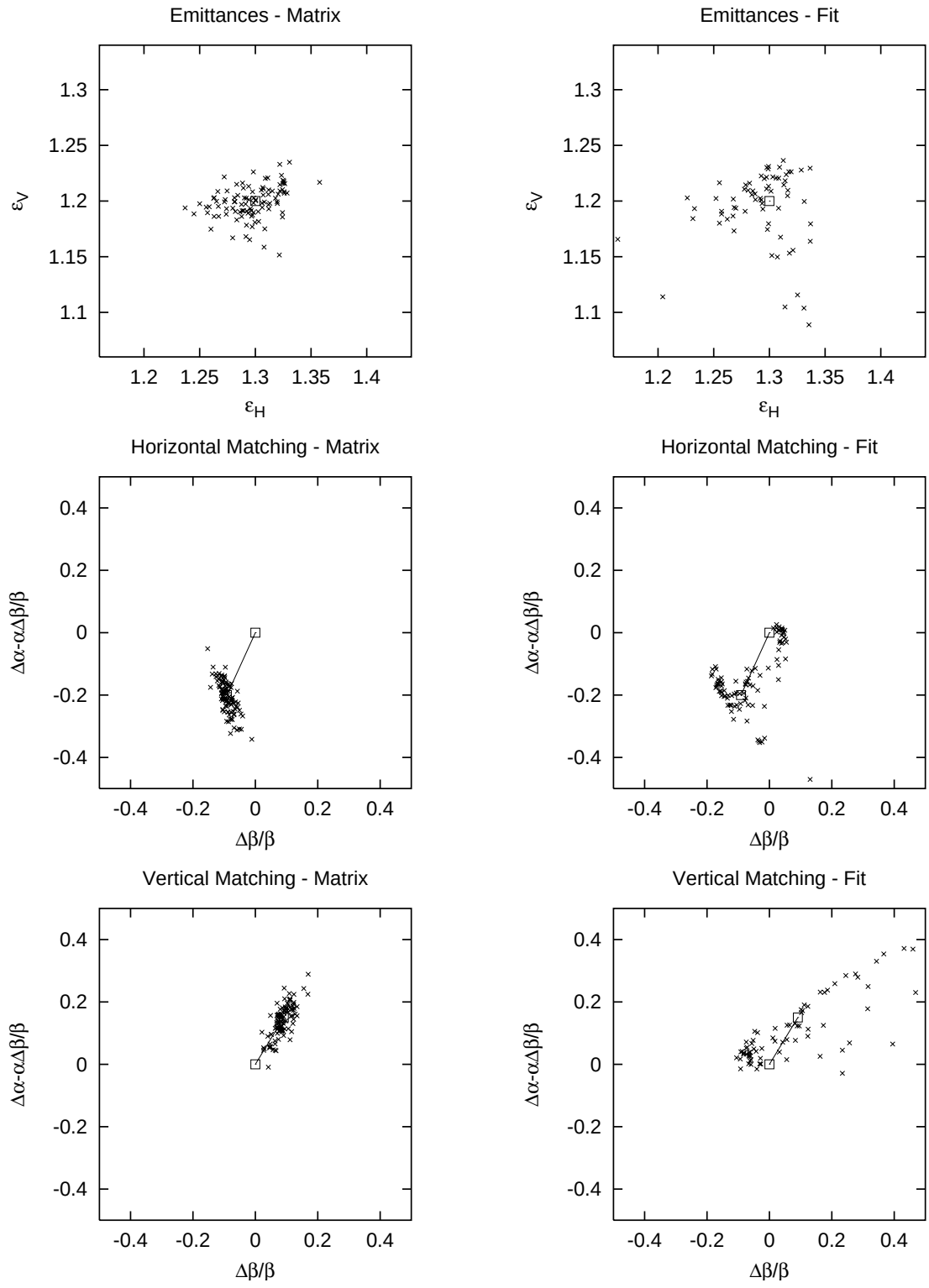

Figure 4.3: Analysis of simulated data with matrix and fit method. Data from six machine turns were used. Tunes: $Q_x = 0.240$, $Q_y = 0.240$. Noise level in quadrupole moment (r.m.s.): σ_κ=0.5 mm^2. No space charge detuning. Sometimes the fit method fails to find the right tunes, and therefore give the wrong mismatch. The emittance results are comparable for the two methods.

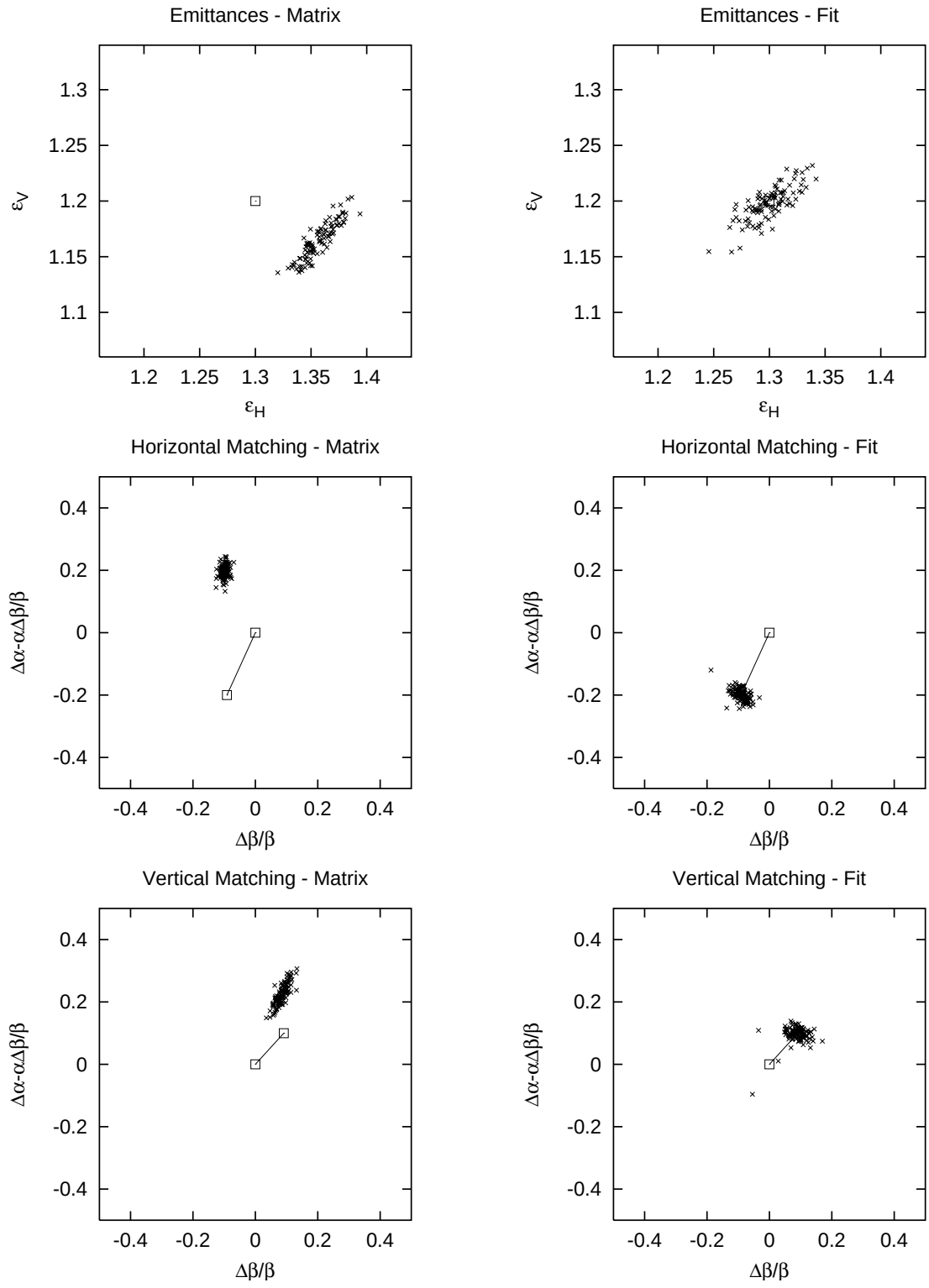

Figure 4.4: Analysis of simulated data with matrix and fit method. Data from six machine turns were used. Tunes: $Q_x = 0.210$, $Q_y = 0.230$. Noise level in quadrupole moment (r.m.s.): σ_κ=0.5 mm^2. Space charge detuning: $\Delta Q_x = -0.060$, $\Delta Q_y = -0.100$. The matrix method give large systematic errors, since it is using the wrong tune.

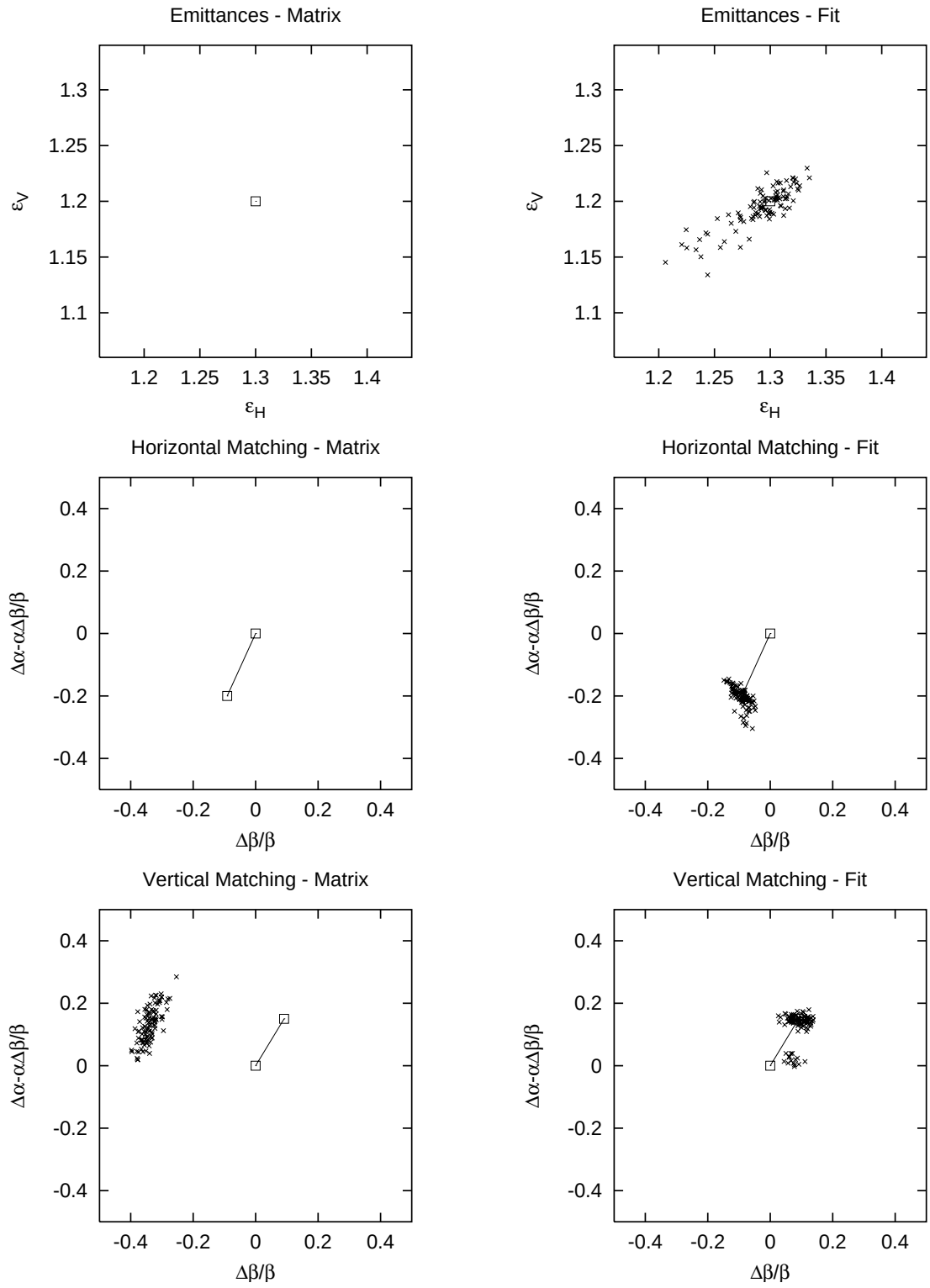

Figure 4.5: Analysis of simulated data with matrix and fit method. Data from six machine turns were used. Tunes: $Q_x = 0.240$, $Q_y = 0.240$. Noise level in quadrupole moment (r.m.s.): σ_κ=0.5 mm^2. Space charge detuning: $\Delta Q_x = -0.060$, $\Delta Q_y = -0.100$. Since the tunes is close to a quarter, the matrix is ill-conditioned. The emittance and horizontal matching calculated with the matrix method matching are off the scale (the emittance was in some cases even imaginary).

"To invent, you need a good imagination
and a pile of junk."

Thomas Alva Edison

Chapter 5

Design of a Magnetic Quadrupole Pick-up

5.1 The First Pick-up Prototype

The very first prototypes, built to prove the principle of common-mode suppression by coupling to the radial field component, were made from tin-cans and metal wire. It was, however, realised that the precision obtained in this way was not sufficient, and it was therefore decided to directly build a full-scale prototype which could eventually be installed in the machine for tests with beam. To fit the PS, this pick-up had to have an aperture of 145 mm, which effectively sets the smallest possible inscribed radius of the antenna loops. The antenna loops were moved a little further from the centre to make place for a ceramic vacuum chamber between the loops and the beam. This gives the advantage that the antenna loops and its readout transformers are outside of the vacuum, and there is no need for signal feed-throughs. This is important since a magnetic pick-up requires a small load impedance, and the small parasitic series resistance introduced by feed-throughs can significantly affect the low frequency response. On the other hand, the distance between the loops and the beam increases with the addition a ceramic layer, which means somewhat lower signal levels. An existing ceramic tube of suitable dimensions (inner diameter 140 mm, length 508 mm) was re-used for the purpose. It had been part of a position monitor in the PS Booster, and had a thick copper layer with electrodes cut out on the inside and embedded signal feed-throughs from each electrode to the outside. The copper layer was chemically removed, and replaced by a thin layer of titanium to avoid static charges building up on the ceramic. The signal feed-throughs had to be retained since they formed part of the vacuum seal. This was not an ideal situation, but was judged acceptable since they were made of non-magnetic material, and the use of an existing ceramic significantly cut the cost and production time for the prototype.

Four antenna loops were placed at 45° angle to the horizontal plane, held tightly in

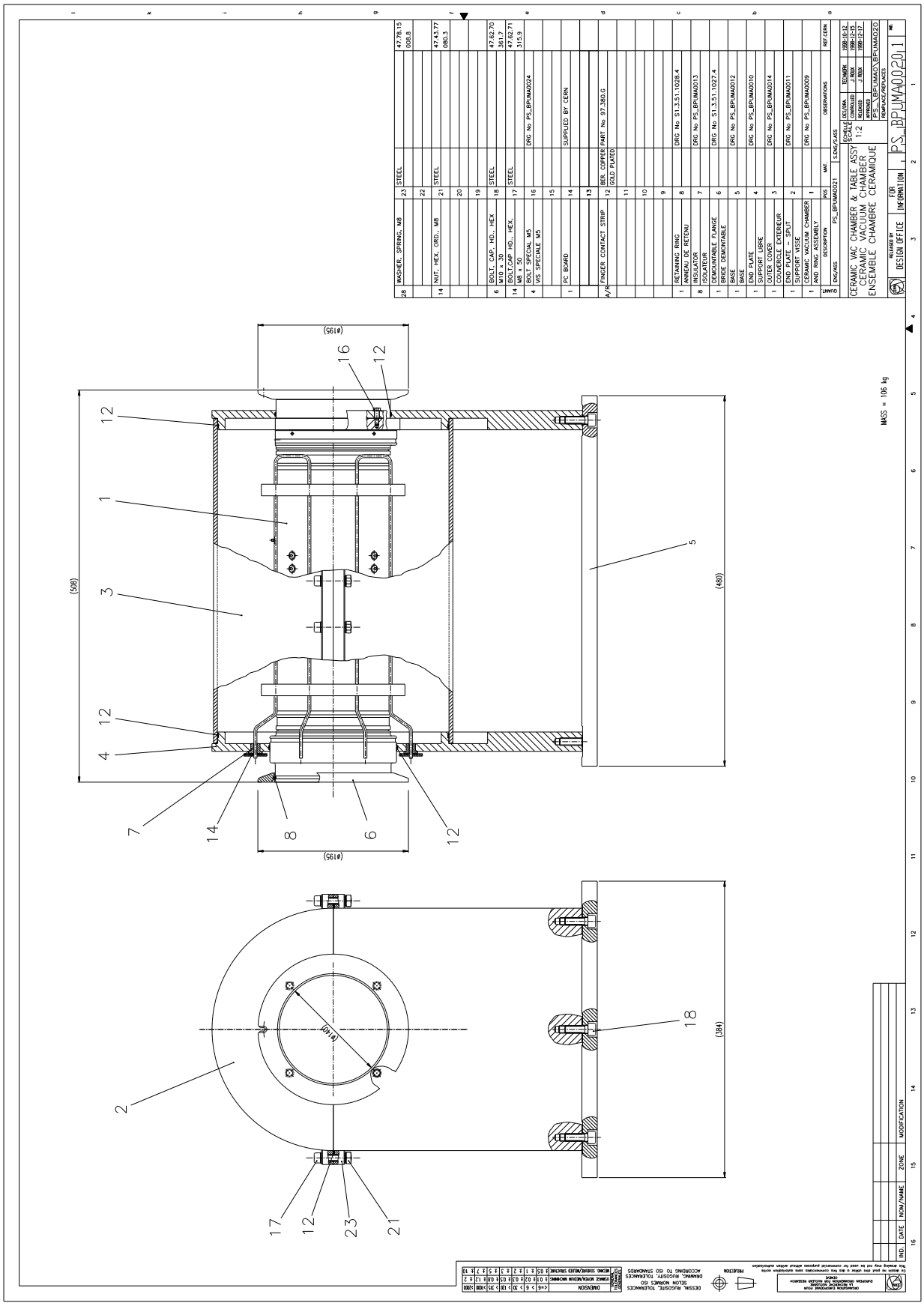

Figure 5.1: CAD drawing of the first prototype pick-up, based on an existing ceramic tube.

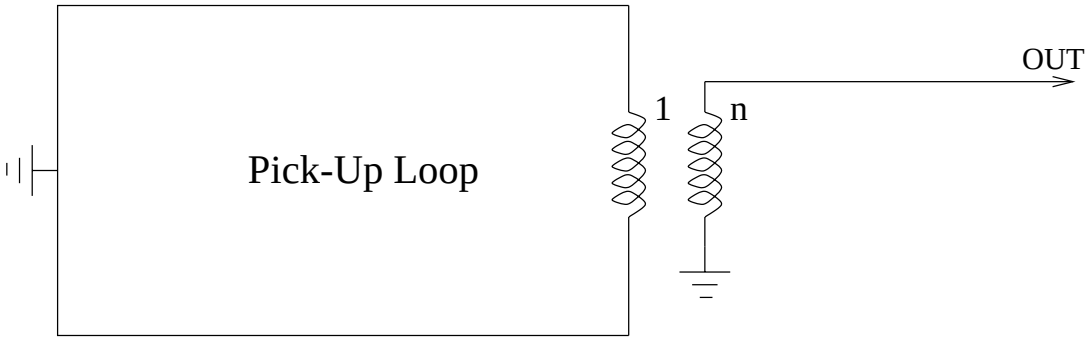

Figure 5.2: Schematic layout of the antenna loop of the first machine prototype. The same design was also tested on the lab prototype.

place by a plastic collar. Although the theoretical prediction showed a maximum of the coupling to the quadrupole mode for a loop opening angle ϕ of about $60-70^\circ$ (depending on the antenna wire thickness a), 45° was chosen to avoid any problems caused by inter-loop coupling.

To ensure continuity for the wall currents and shield against outside noise, a cylindrical copper casing was built around the ceramic and the loops. The radius of the conducting cylinder was set to 150 mm, a bit less than twice the distance from the antenna loops to the centre of the pick-up. This corresponds roughly to the theoretical threshold value where no more sensitivity to the quadrupole moment is gained by increasing the radius. The casing was made in two halves, so that it could (in principle) be dismantled without breaking the vacuum once the pick-up was installed. To ensure good electrical contact between parts, spring contacts were used in all contact surfaces and joints.

The antenna loops of the first prototype pick-up were made from a bent copper rod and had a fairly simple design. One of the short ends of the loop was connected to ground (i.e. to the beam pipe), and in the other end the loop current was measured using a simple current transformer (see Fig. 5.2). This layout is the simplest possible that produces a symmetric loop. An asymmetric loop would give problems at high frequencies due to path length differences for the induced signals. The transformer was a high-mu core with a 15 turn winding, threaded onto the the copper rod of the antenna loop. Its secondary side was connected directly to a $50\,\Omega$ cable, giving a total down-transformed load to the antenna loop of about 200 mΩ. For an estimated loop inductance of about 500 nH, this would give a low frequency cut-off at 75 kHz.

After some bench tests in the laboratory, that gave encouraging (although not perfect) results, the prototype was installed in the PS machine to be tested with beam.

5.2 The Lab Prototype

To study the impact of different design details, and to perfect the final design, a second prototype was built for lab measurements. This lab prototype inherited many of the design parameters from the first prototype (notably its dimensions), but with the important simplification that it did not include any ceramic, since it was not built to be installed in the machine.

The main difference from the first prototype was the inclusion of four thin metal vanes, placed in the electric symmetry planes of the quadrupole field mode (i.e. at 45° to the horizontal plane) in order to shorten the path for the wall current and thereby reduce the effect of the abrupt step in the conducting boundary.

The lab prototype was used to understand and optimise the electrical properties of the pick-up, in order to arrive at the best design of the antenna loops and their read-out transformers. The first design to be tested was the one used in the machine prototype (see Fig. 5.2). Since this version was found to have a relatively poor common-mode rejection, the ground point was moved to the transformer end of the loop. To keep the symmetry, this required an arrangement of three readout transformers (see Fig. 5.3).

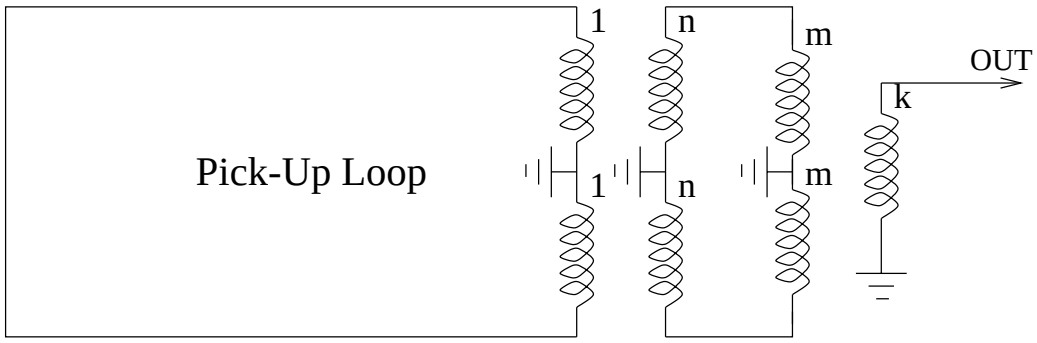

Figure 5.3: Schematic layout of the improved version of the antenna loop design. To move the ground connection to the transformer end of the loop, three separate transformers were needed to make the current read-out symmetric.

The attention was then turned to the influence of the pick-up on the beam. It was found that by connecting the far end of the loop to ground via a suitably chosen resistor (see Fig. 5.4), high frequency strip-line resonances in the loop could be damped.

Once the basic design was fixed, the optimum winding ratios on the three transformers were studied. It was found best to have the first two transformers perform the impedance transformation with a winding ratio of 1:21, while letting the last transformer take the difference between the two signals on a constant impedance level (the winding ratios were 10+10:14 turns).

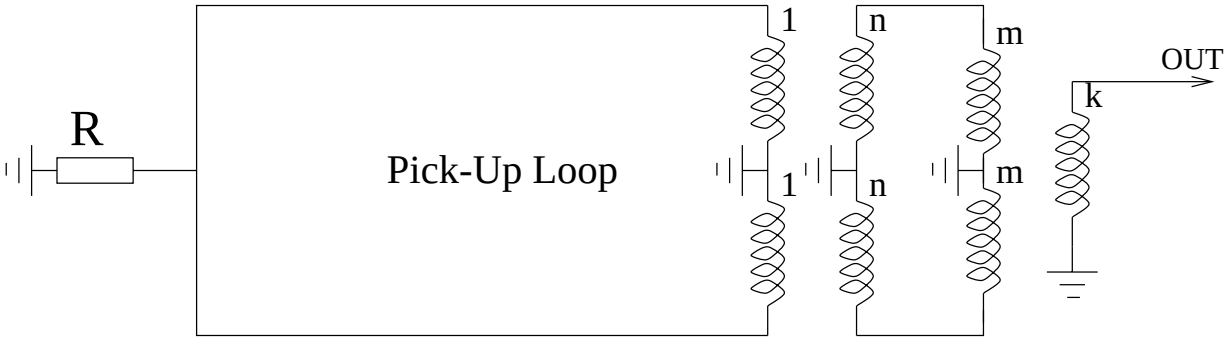

Figure 5.4: Schematic layout of the final antenna loop design. The termination resistor was chosen to 200Ω*, and the transformer windings* $n = 21$*,* $m = 10$ *and* $k = 14$*.*

5.3 The Final Optimised Pick-up

With the experience gained from the studies on the prototype, a final design was developed. It was built on the lab prototype design, which was modified to accommodate a ceramic vacuum chamber. The four antenna loops were made of two parallel, interconnected rods made of copper-beryllium alloy for its good conductivity and mechanical rigidity. They were held in position with a good precision by ceramic insulators in each end of the pick-up. In the far end of each loop, the inter-connection between rods was made with a bar of copper, the centre of which was connected to ground via the termination resistor. In the transformer end, the copper-beryllium bars were fed through to the outside of the cavity, where the transformer arrangement for the read-out was housed inside a brass block. As in the case of the first prototype, the inside of the ceramic was coated with a thin resistive layer to remove any static charges deposited by the passing beam. In the final version, however, this layer was also optimised to also act as a screen to reduce the longitudinal impedance of the pick-up (see Chapter 7.1). The first pick-up built on the final design had a low resistivity coating of about $3.5\,\Omega$ optimised to yield the best possible screening effect compatible with the required bandwidth of the pick-up. Since this version was not performing well in terms of common-mode rejection, a high resistivity coating of about $80\,\Omega$ was finally chosen. A drawing of the final design pick-up is shown in Fig. 5.5.

5.4 Auxiliary Electronics

5.4.1 Hybrid

The signals from the four pick-up loops were connected to a hybrid circuit that produces the composite signals corresponding to beam position and quadrupole moment. Due to the special pick-up geometry, the signal combination is different from the case of an electrostatic

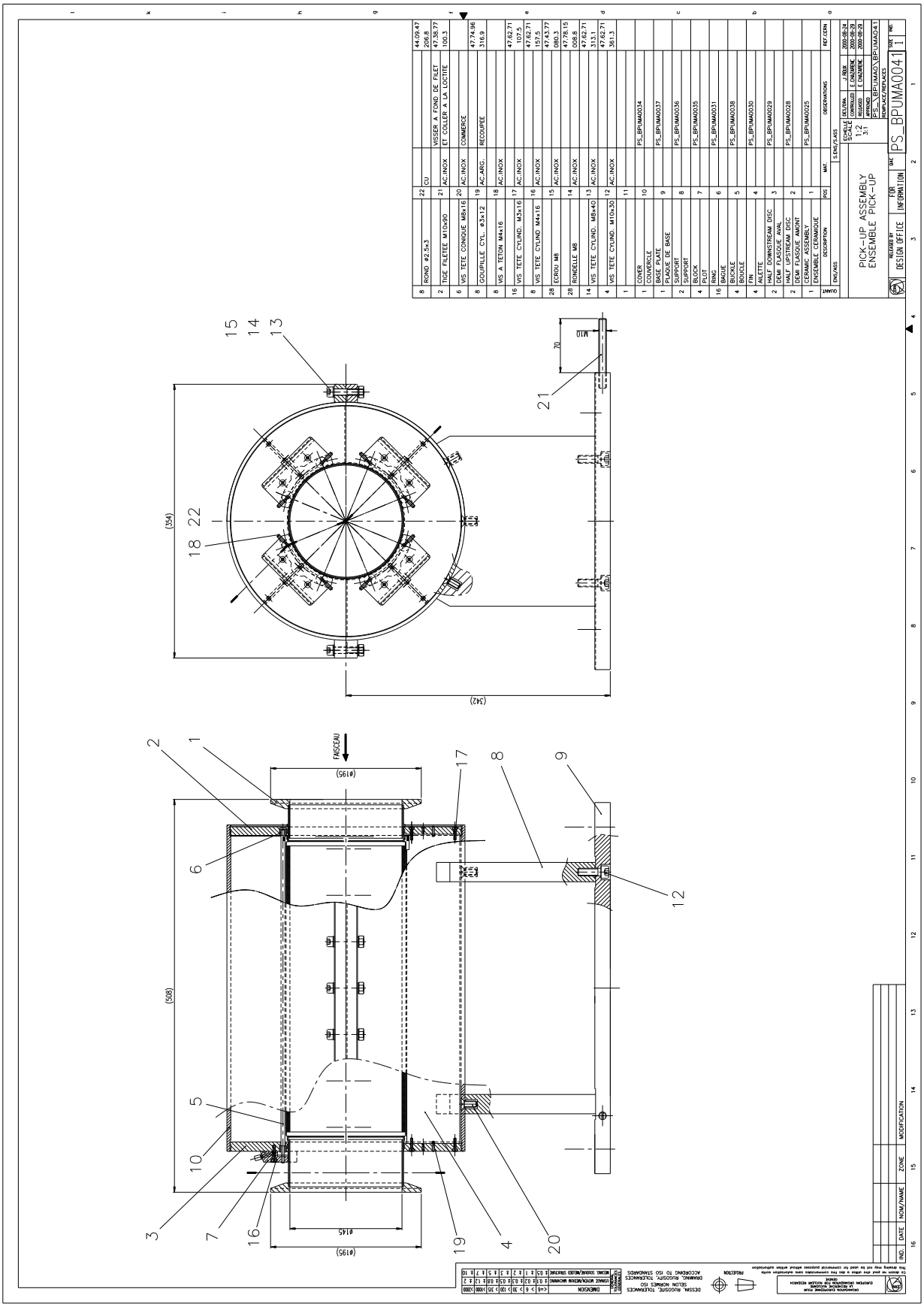

Figure 5.5: CAD drawing of the final pick-up design.

pick-up.

$$\begin{aligned} \Delta_{\mathrm{H}} &\propto TR-BR-BL+TL \\ \Delta_{\mathrm{V}} &\propto TR+BR-BL-TL \\ \Xi &\propto TR-BR+BL-TL \end{aligned} \tag{5.1}$$

where TR is the top right loop, BL the bottom left etc. The Σ signal is zero by design, and was not used. Note especially the configuration for the Δ signals where Δ_{V}, for example, is not the difference between the top two loops and the bottom two loops, as might be intuitively expected. This is a consequence of the fact that it is the radial field component that is measured.

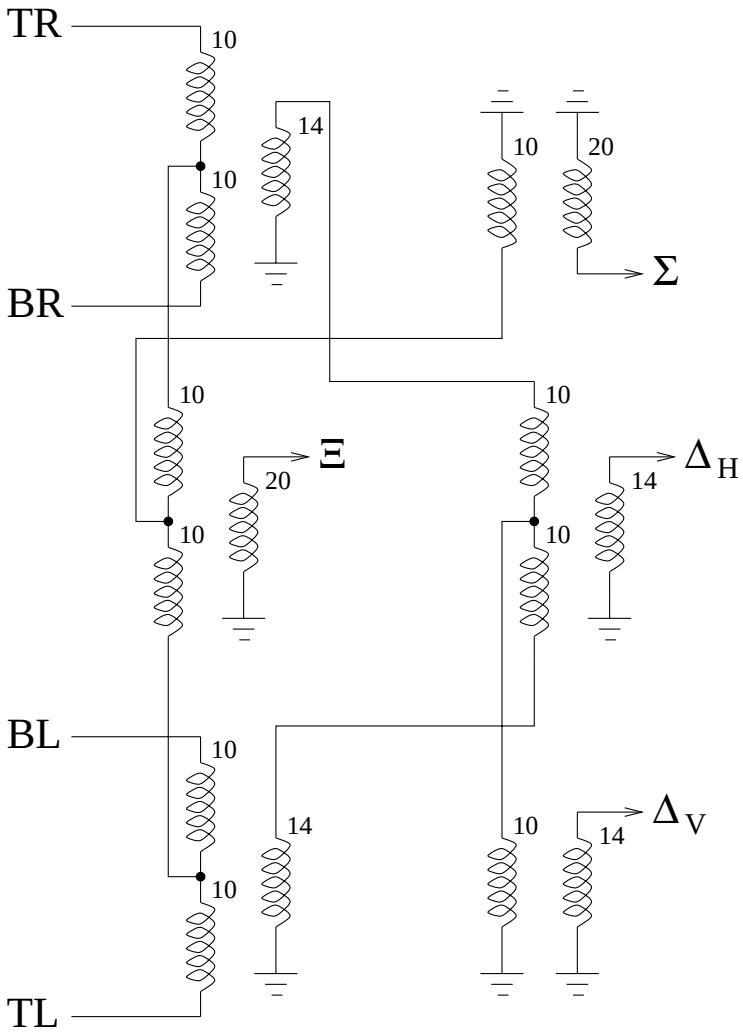

Figure 5.6: Schematic layout of the hybrid circuit. For the machine prototype, the circuit could be bypassed to enable the study of individual antenna loop signals.

The hybrid circuit design is shown in Fig. 5.6. Since the magnetic pick-up has a low impedance, no active elements were needed in the hybrid. It is therefore not sensitive to radiation, which means it can be placed very close to the pick-up. This is favourable for the common-mode rejection.

However, since the pick-up is already suppressing the common-mode signal, the requirements on the hybrid are not very strict. One could in principle suppress the hybrid and measure the signal from each antenna loop individually. To enable this possibility, the hybrid of the machine prototype could be bypassed by remote-controlled switches. However, the use of a hybrid is more practical, and these switches were therefore suppressed in the final version to simplify the circuit.

5.4.2 Amplifiers

Due to the small transfer impedances of the pick-up, the signals must be amplified before they can be sent through the rather long cables (100 m) to the data acquisition equipment. The amplifiers for this purpose were located under the machine, protected from radiation. For the prototype pick-up, 40dB amplifiers with a bandwidth of 30 MHz and a noise level of 2.3 $\mathrm{nV/Hz^{1/2}}$ were used. For the final pick-up installation, these were changed to specially developed low-noise amplifiers with a switchable gain, where one gain setting was optimised for the LHC beam intensity, and the other was a high gain channel built to enable future attempts to measure the matching also of stacked LHC lead ions, that will be injected into the PS from the LEAR machine.

"Computers are useless. They can only give you answers."

Pablo Picasso

Chapter 6

Bench Measurement and Simulation Methods

6.1 The Wire Method of Simulating a Beam

A relativistic particle beam moving at nearly the speed of light induce purely transverse transverse fields inside a smooth conducting beam pipe. The effect of the beam on its surroundings can therefore be simulated using a wire through the vacuum chamber to produce a TEM waveguide[38]. This is a standard method which was utilised in both bench measurements and simulations.

6.1.1 Transfer Impedance Measurement

The transfer impedances parametrises the sensitivity of the pick-up to beam position, size etc. They can be measured by recording the ratio of pick-up output voltage and wire current as a function of wire position. The general expression for the transfer impedance is, as discussed previously

$$\frac{U}{I} = Z_{\text{tot}} = Z^{(0)} + Z^{(x)}\, x + Z^{(y)}\, y + Z^{(\kappa)}\, \kappa + Z^{(\kappa')}\, \kappa' + Z^{(\zeta)}\, \zeta + Z^{(\zeta')}\, \zeta' + \dots \tag{6.1}$$

which, for a thin wire (line current) at transverse position (r, θ) in polar coordinates, yields

$$\frac{U}{I} = Z_{\text{tot}} = Z^{(0)} + Z^{(x)}\, r\cos\theta + Z^{(y)}\, r\sin\theta + Z^{(\kappa)}\, r^2\cos 2\theta + Z^{(\kappa')}\, r^2\sin 2\theta + \\ + Z^{(\zeta)}\, r^3\cos 3\theta + Z^{(\zeta')}\, r^3\sin 3\theta + \dots \tag{6.2}$$

One can of course measure the response of the pick-up for a large number of points distributed over the entire interesting region of (r, θ) space, and then fit the expression to the

data to obtain the impedances. However, there are some simplified ways to determine the transfer impedances, making use of the particular form of Eq. (6.2).

If the wire position is rotated around the pick-up centre with a fixed offset r, the different transfer impedances can be identified from the Fourier transform of the response as a function of azimuth θ. This method was used to study the first prototype.

Alternatively, one can keep the azimuthal angle fixed, and measure the response along a straight line. If the angle is well chosen, the individual transfer impedances can then be found as the coefficients in a polynomial in the variable r, fitted to the data. This was the way the lab prototype and the final version pick-up were studied.

6.1.2 Longitudinal Impedance

The longitudinal impedance of an object can be determined using a centred (coaxial) wire, by measuring the signal transmission (scattering parameter) through the structure, and compare with a smooth vacuum chamber of the same length. The conversion from scattering parameter to impedance is necessarily model-dependent, since the measured quantity is not directly the induced longitudinal voltage, but the attenuation and phase shift of the transmitted TEM-wave. There are several different formulae for the conversion, depending on the model used. If the object is much smaller than a wavelength, the lumped impedance approximation[53]

$$Z = 2Z_c \frac{1 - \frac{s_{21,\mathrm{OBJ}}}{s_{21,\mathrm{REF}}}}{\frac{s_{21,\mathrm{OBJ}}}{s_{21,\mathrm{REF}}}} \tag{6.3}$$

can be used. Here, $s_{21,\mathrm{OBJ}}$ is the forward scattering parameter of the object under test, $s_{21,\mathrm{REF}}$ is the same parameter for a smooth pipe of equal length, and Z_c is the characteristic impedance of the coaxial transmission line formed by the pipe and the wire. For homogeneously distributed impedances that are long compared to the wavelength, a better approximation is given by

$$Z = -2Z_c \ln \frac{s_{21,\mathrm{OBJ}}}{s_{21,\mathrm{REF}}}, \tag{6.4}$$

and if the electrical length l of the distributed impedance is known, an even better estimate can be obtained with[54]

$$Z = -2Z_c \ln \frac{s_{21,\mathrm{OBJ}}}{s_{21,\mathrm{REF}}} \left(1 + \mathrm{i}\, \frac{\ln \frac{s_{21,\mathrm{OBJ}}}{s_{21,\mathrm{REF}}}}{2\omega l/c} \right). \tag{6.5}$$

All the above formulae are approximations valid only for impedances that are small compared to the characteristic impedance Z_c of the transmission line. The fact that there is not a unique formula illustrates a fundamental limitation with the coaxial wire method: it is not possible to determine the longitudinal impedance if the structure under test is

considered as a 'black box'. For simple structures like the above cases of localised or homogeneously distributed impedances, this is not a problem. For more complicated structures, like the quadrupole pick-up considered here, it can however be hard to interpret the s-parameter result, and one usually resorts to using one of the above formulae based on simple cases as an approximation. It should, however, be noted that the Taylor expansions of the above formulae are all identical to first order in $\Delta s_{21} = s_{21,\mathrm{OBJ}} - s_{21,\mathrm{REF}}$. This condition coincides with the basic assumption in the derivation of these formulae: that the impedance should be small. Therefore, for small impedances ($Z \ll Z_c$) all three formulae give the same result. Likewise, for very large impedances ($Z \gg Z_c$) all three formulae fail, and hence the choice of formula is only important for intermediate impedances. Since the aim of the bench measurements and simulations of the pick-up was rather to minimise than to accurately determined the value of the impedance, this limitation of the coaxial wire method was not really a problem. The impedance of the final pick-up was so small that all formulas gave approximately the same result. To be consistent, all impedance values presented in this report were interpreted using the log-formula in (6.4).

Another problem with the wire method is that the presence of the conducting wire changes the electro-magnetic properties of the object being studied. The waves of the TEM mode created by the wire can be reflected when it sees a local impedance, whereas the real beam only excite non-propagating field modes at frequencies below the cut-off frequency of the beam pipe. Therefore, if several localised impedances are present, multiple reflections of the TEM-wave can occur, which show up as "false" impedance peaks in the measurement. Again, since the reflections are related to the magnitude of the longitudinal impedance, this problem is not so severe if one is mainly interested in minimising the impedance, rather than determining its exact value.

6.2 Bench Measurement Setup

The devices for holding the wire in place at each end of the pick-up were made in such a way that the wire could easily be moved to any position in the transverse (r, θ) plane. At first, a pulse generator and an oscilloscope was used to simulate a beam bunch and record the response. This time-domain measurement setup was later changed to a frequency-domain setup using a network analyser as combined current source and measurement instrument. Using two different analyser models, frequencies ranging from 10 kHz to 3 GHz could be studied. The network analyser was controlled and read out over its GPIB interface using a LabView program specially developed for the purpose.

To obtain as good matching as possible between the 50 Ω source and the coaxial line formed by the pick-up and the wire, matching resistors were added in series with the wire at the entry and exit of the pick-up (see Fig. 6.1).

Good matching is of prime importance especially to extract an absolute value of the longitudinal impedance from the s-parameter measurements. Any mismatch give rise to reflections which result in apparent impedance peaks at wavelengths where destructive interference occurs. In practice, however, good matching is not so easy to obtain over a

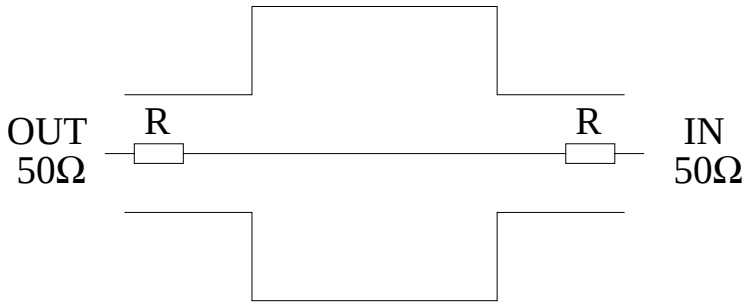

Figure 6.1: Setup for the lab measurements. The wire transverse position of the wire could be moved to measure the transfer impedances. At the input and output, the TEM waveguide formed by the beam-pipe and the wire was matched to the 50 Ω cable using the resistors R.

large frequency band.

6.3 The HFSS Simulation Program

6.3.1 Program Description and Functionality

Since prototypes are expensive to build, most studies of the pick-up properties were done by simulations. The High Frequency Structure Simulator[55] (HFSS) program, used for this purpose, simulates the electro-magnetic properties of structures by the Finite Element Method (FEM). It has a graphical user interface very similar to a CAD program, where a model of the structure can be drawn and a number of ports specified. The program then calculates the scattering parameters for the N-port in a chosen frequency range.

The simulation process has two main stages. First, the finite element mesh is created and optimised, and then a frequency sweep can be performed to study the frequency dependence of the s-parameters. The initial tetrahedra mesh is created using the available vertices in the model. It is very coarse and has to be refined in order to achieve an accurate result. A so-called adaptive mesh refinement is therefore performed. The mesh is refined by iteratively solving the problem and splitting the tetrahedra containing the highest field energy into smaller ones. This procedure makes sure that the mesh is only refined in areas where it is needed. In order for the adaptive refinement to work, the initial mesh has to be reasonable, so that the power distribution is approximately correct. That means, generally, that the initial tetrahedra should not have too large aspect ratios (ratio between longest and shortest side), since the basic FEM approximation of interpolating the fields inside the tetrahedra from its values at the vertices then becomes invalid. The initial mesh can be improved, if needed, by adding extra vertices to the original model (seeding the mesh). The adaptive refinement is terminated when the changes in the simulated s-parameters between two iterations are below a pre-defined threshold.

The frequency sweep which follows can be performed in two ways. Either the problem

is solved exactly for each discrete point in the desired frequency range, or an approximate frequency dependence can be calculated from the solution at one given frequency. If the mesh is properly optimised and the frequency range reasonably narrow, the two methods give the same result. The approximate solution is however faster if many points within the range are to be calculated.

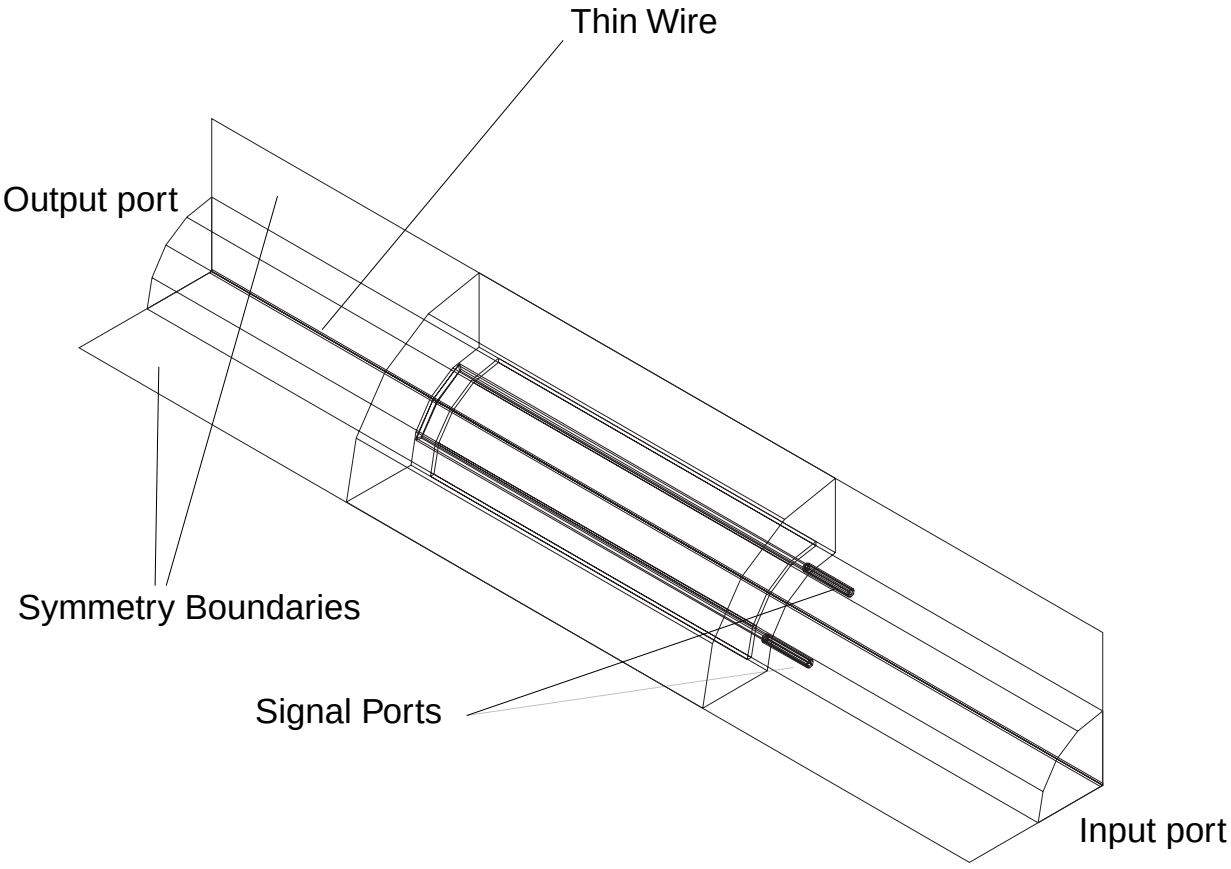

Figure 6.2: HFSS model of the pick-up. Only one quarter of the pick-up was modelled, and symmetry boundaries were used to reduce the computing time.

6.3.2 Modelling the Pick-up Structure

To obtain a stable mesh with a reasonable number of mesh points, in order to achieve an accurate result without requiring too much CPU time, the pick-up model was simplified as much as possible. All unnecessary details very suppressed, and thin objects were modelled as 2D sheets to avoid a too detailed mesh. Also, all metallic surfaces were assumed to be perfectly conducting, except in cases where this could falsify the result (i.e. for longitudinal impedance determination). The transformer arrangement for the read-out of the loops was

replaced by two ports with a characteristic impedance set to one half of the total antenna load. Also, a port in each end of the vacuum chamber was provided to feed in the beam current. The model is shown in Fig. 6.2.

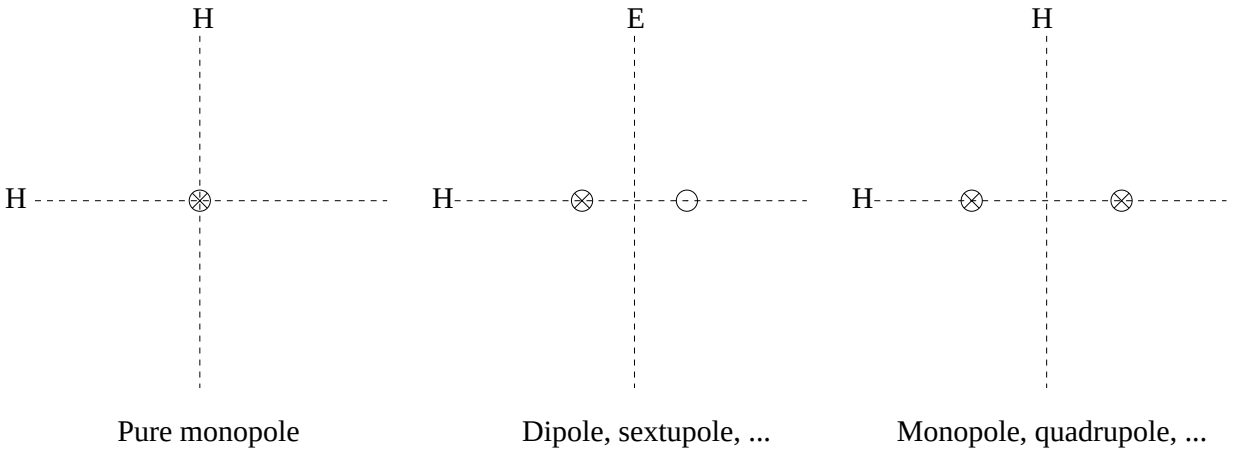

Figure 6.3: Transverse wire locations used to produce different field modes in the pick-up. The circles denote the antenna wires (cross indicates that the current is going into the page), and the dashed lines show the symmetry planes. Using the symmetry, only the quarter of the pick-up needed to be modelled in the simulation program. The first setup produces only the monopole fields mode. The second produces dipole, sextupole etc, and the third produces monopole, quadrupole etc.

Since HFSS cannot simulate particle beams, the beam was substituted by a thin wire, just as in the lab measurements. The four-fold symmetry of the structure was also used in order to reduce the problem size and save computing time. Thus, only one quadrant of the pick-up was simulated, and appropriate boundary conditions imposed at the cuts (see Fig. 6.3). For the simulations of longitudinal impedance with the coaxial wire method, two H-boundaries and an centred wire was used. In order to determine the transfer impedances, an offset wire was needed. Two different boundary settings were required to determine all the interesting transfer impedances. With one H-type and one E-type boundary, non-zero dipole and sextupole moments are produced. Similarly, an offset beam with two H-type boundaries produce non-zero monopole and quadrupole moments. The corresponding transfer impedances were determined by simulating several wire positions and fitting a polynomial to the result to separate the different couplings.

6.3.3 Eliminating Systematic Mesh Effects

The HFSS program allows for the addition or subtraction of a length l of matched transmission line to any port in the model, with subsequent re-calculation of the scattering parameters using the analytical formula

$$\tilde{s}_{21} = e^{\gamma l} \cdot s_{21} \tag{6.6}$$

where $\gamma = \alpha + j\beta$ is the propagation constant. This constant is calculated by the program from a 2D model of the port. Since the subtraction of a matched transmission line of the same length as the pick-up is equivalent to the division by the reference s-parameter in (6.4), this was initially used to obtain the quantity $s_{21,\mathrm{OBJ}}/s_{21,\mathrm{REF}}$.

It was found, however, that in the HFSS simulation result there was systematically a residual delay left after this correction, which turns into a non-physical reactive impedance. The delay is always positive (under-estimates the phase) and increases linearly with frequency. The reason seems to be that the propagation constant calculated from the 2D model of the ports does not correspond to the simulated propagation of the wave through the 3D model. The effect decrease with increasing mesh size, as can be expected if the problem is related to the discretisation.

Since the mesh size is effectively limited by the computing resources, the problem was circumvented by simulating the reference s_{21}-parameter of the pipe only, using the same mesh but changing the material properties in the model to produce a smooth pipe without discontinuities (as seen from the inside).

"Experience is simply the name we give our mistakes"

Oscar Wilde

Chapter 7

Bench Measurement and Simulation Results

7.1 Transfer Impedances

7.1.1 Verifications of Analytic Formulae

In the derivation of the analytic expressions for the transfer impedances, certain simplifying assumptions were made. Notably, the fields were calculated in two dimensions, assuming that the pick-up was infinitely long. The effect of the pick-up length was introduced only later, in the calculations of the transfer impedances. In reality, the finite length of the pick-up make the transverse fields a function of the longitudinal position in the pick-up. Therefore, in order to verify the validity of the analytical expressions, a series of simulations was performed to determine the dependence of the transfer impedances on the basic parameters of the pick-up. The simplest possible pick-up model, consisting of a round beam pipe with a cylindrical cavity housing the antenna loops, was used for this purpose. Simulated results for the dependence of the transfer impedances on the loop opening angle ϕ are shown in Fig. 7.1, for some different values of the cavity radius d. There is a good agreement between simulated and theoretical values. Likewise, the simulated dependence on the depth of the shielding cavity, shown in Fig. 7.2, follow the theoretical expectations. By varying the pick-up length in the simulation, it could also be concluded that the analytic results are valid also for pick-ups that are short with respect to the cavity radius.

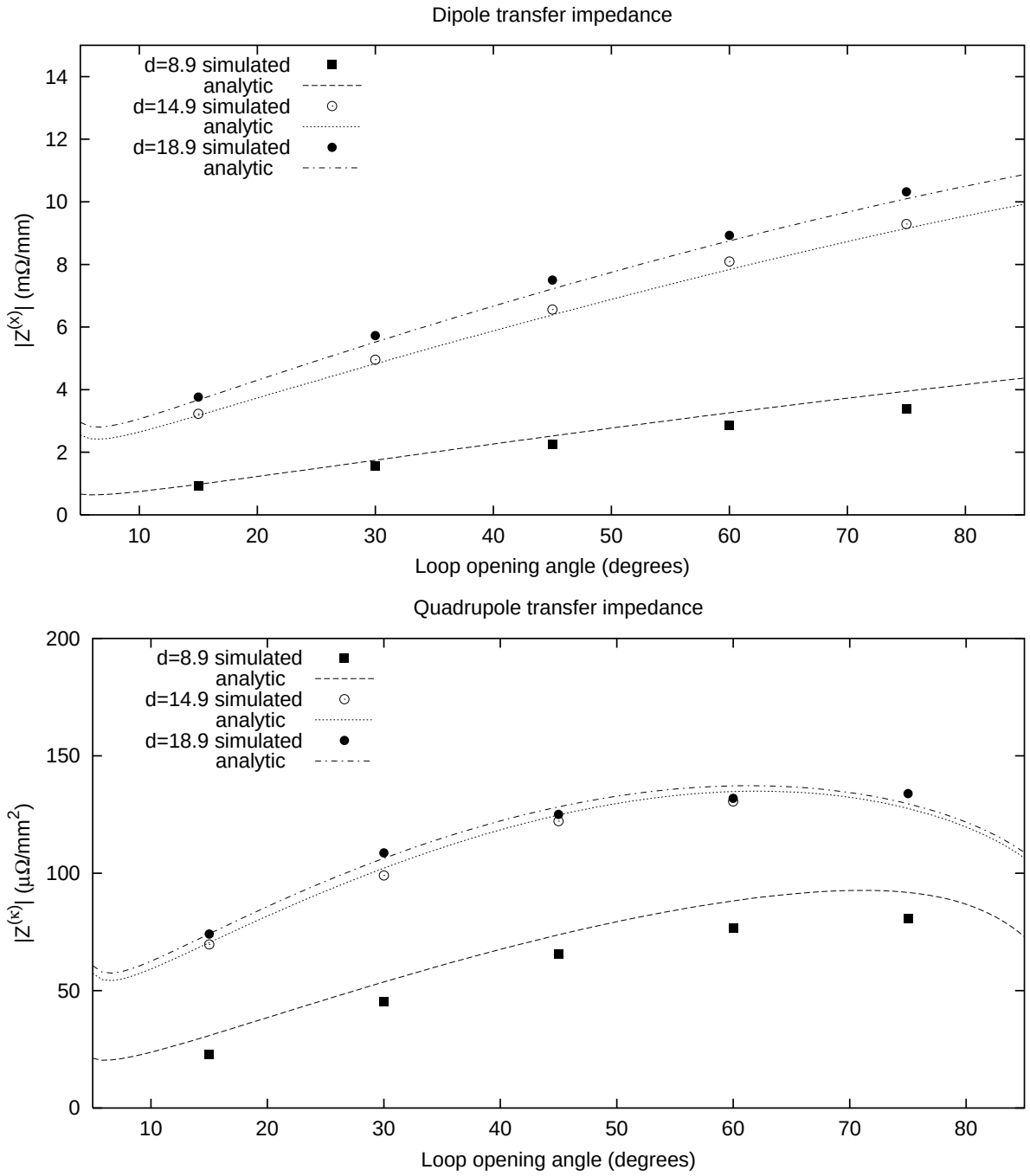

Figure 7.1: Simulated dipole and quadrupole transfer impedance in the pass-band for the 'conceptual' pick-up, as a function of the loop opening angle. The antenna position was 8.15 cm, the antenna rod radius 2.5 mm, and the load 200 mΩ. Data for some values of the cavity radius d are shown. The lines are the analytical predictions.

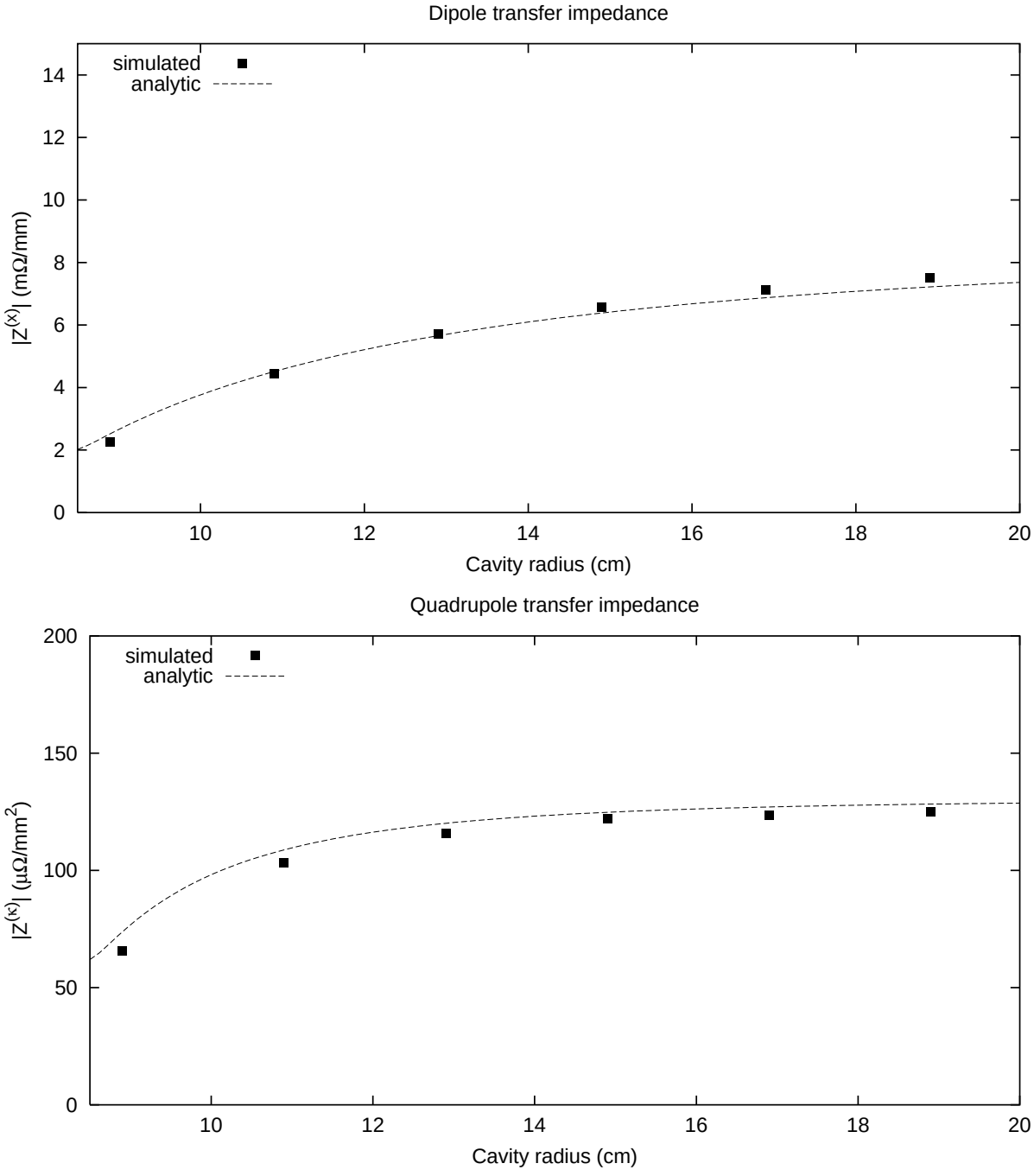

Figure 7.2: Simulated dipole and quadrupole transfer impedance in the pass-band for the 'conceptual' pick-up, as a function of the cavity radius d. The antenna position was 8.15 cm, the antenna rod radius 2.5 mm, and the load 200 mΩ.

7.1.2 Prototype Measurements and Simulations

First Machine Prototype

The transfer impedances of the first machine prototype were measured in the laboratory before the pick-up was installed in the machine. This was done by introducing an off-centre wire antenna and recording the response of the pick-up to the wire current as a function of its azimuthal position. A pulse generator was used to simulate the current pulse of a passing bunch, and the corresponding pulse height on the different pick-up outputs were measured. The results of these measurements are shown in Fig. 7.3. The transfer impedances for field modes up to sextupole were extracted from the data using Fourier transform, and the result is summarised in Tab. 7.1. The measured values were compared to simulated ones with good agreement.

	Δ_H	Δ_V	Ξ		
$Z^{(0)}$	0	0	-0.0007	$\pm$ 0.005	Ω
$Z^{(x)}$	2.38	0.20	0.08	$\pm$ 0.17	mΩ/mm
$Z^{(y)}$	0.14	2.23	-0.10	$\pm$ 0.17	mΩ/mm
$Z^{(\kappa)}$	1.54	1.54	-47.07	$\pm$ 5.6	$\mu\Omega$/mm^2
$Z^{(\kappa')}$	-1.54	1.54	1.54	$\pm$ 5.6	$\mu\Omega$/mm^2
$Z^{(\zeta)}$	240.0	81.6	15.1	$\pm$ 186	nΩ/mm^3
$Z^{(\zeta')}$	57.7	297.7	40.8	$\pm$ 186	nΩ/mm^3

Table 7.1: Transfer impedances for the first prototype, extracted from the data plotted in Fig. 7.3.

The Lab Prototype

In the lab prototype, thin metal vanes were inserted in the electric symmetry planes of the quadrupole mode. By their placement, they are invisible to the quadrupole field, but suppresses field components with different symmetries. The transfer impedances of the lab prototype were determined from the response to displacements of the antenna wire along the horizontal and vertical axes. Using a network analyser, the frequency characteristics could also be determined. Simulations of the transfer impedances, shown in Fig. 7.4, agree well with the measurements, and demonstrate that the dipole transfer impedance is reduced by about 20% by the presence of the vanes.

Further simulations showed that the addition of symmetrically placed termination resistors in the far end of the loops gave no significant effect on the transfer impedances. This was also observed by measurements.

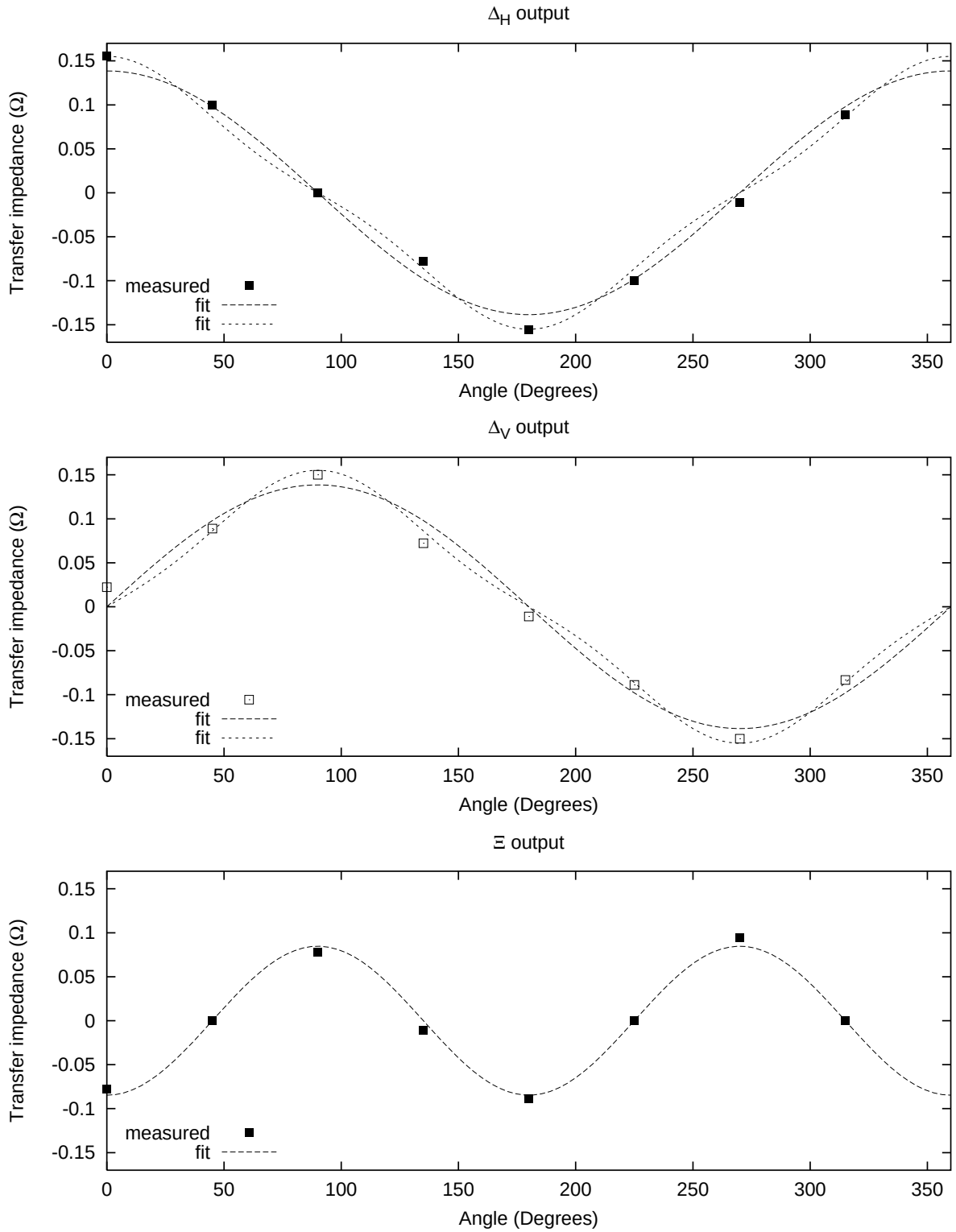

Figure 7.3: Coupling from wire antenna to the output of the hybrid, as a function of the azimuthal position of the antenna wire in the first prototype pick-up. For the dipole outputs, the dashed line is a fit assuming a pure dipole mode, and dotted line is a fit taking into account also the effect of the sextupole mode.

The Final Pick-up

The metal coating on the inside of the ceramic was initially added only to remove static charge from the insulating tube. However, it was realised that such a layer also reduces the longitudinal impedance by screening the electromagnetic fields induced by the beam[56]. The layer acts as a shunt, since if the impedance of the structure behind it is larger than the end-to-end resistance of the coating, the major part of the wall current pass through the coating.

This effect is particularly useful to exploit for a pick-ups structure, since the longitudinal impedance of the cavity is small at low frequencies, and therefore there is no screening effect. Simulations were performed to find the optimum value of the resistivity of the layer[57]. In general, it was found that for a fixed coating resistance, the high frequency cut-off is higher for the higher order field components. Since the monopole field component is not measured, the dipole signal cut-off is therefore the limiting factor. A scan of coating resistivities showed that a surface resistance of about 3.5 Ω would give a cut-off around 25 MHz for the dipole signal and 30 MHz for the quadrupole signal. Measurements of the coupling impedance performed on a prototype pick-up with approximately this coating resistivity agreed well with the simulations (see Fig. 7.5).

However, with such a low resistivity, the common-mode rejection of the pick-up was poor (see next section) and the resistivity was therefore increased to 80 Ω. In this case, no screening effect was observed for the measured signals in the pass-band of the pick-up. The transfer impedances for the final pick-up were therefore the same as for the pick-up without ceramic (Fig. 7.4).

7.2 Undesired Couplings

Ideally, when combining the four antenna loop signals in the way outlined in the previous chapter, the signal components proportional to the different beam moments should be separated, so that the Δ signals are only dependent on the beam position and the beam sextupole moment, and the Ξ signal is only dependent on the quadrupole moment κ.

In reality, there are always parasitic couplings. As long as these couplings have the same frequency characteristics as the desired signals, their effect can relatively easily be corrected for after signal acquisition. Such couplings are caused e.g. by misalignments in the antenna loops. Couplings with a different frequency characteristics are, however, much worse since they distort the measured bunch shape. Correcting the measured signal for this kind of parasitic couplings is, although theoretically possible, not practical. These coupling must therefore be suppressed.

The strongest parasitic coupling is naturally due to the strongest field component (i.e. the monopole field), which is just proportional to the beam current. The couplings from a centred wire to the four antenna loops were therefore measured using a network analyser, and the results combined numerically using Eq. (5.1) to form the composite signals Δ_{H}, Δ_{V} and Ξ. No hybrid was used.

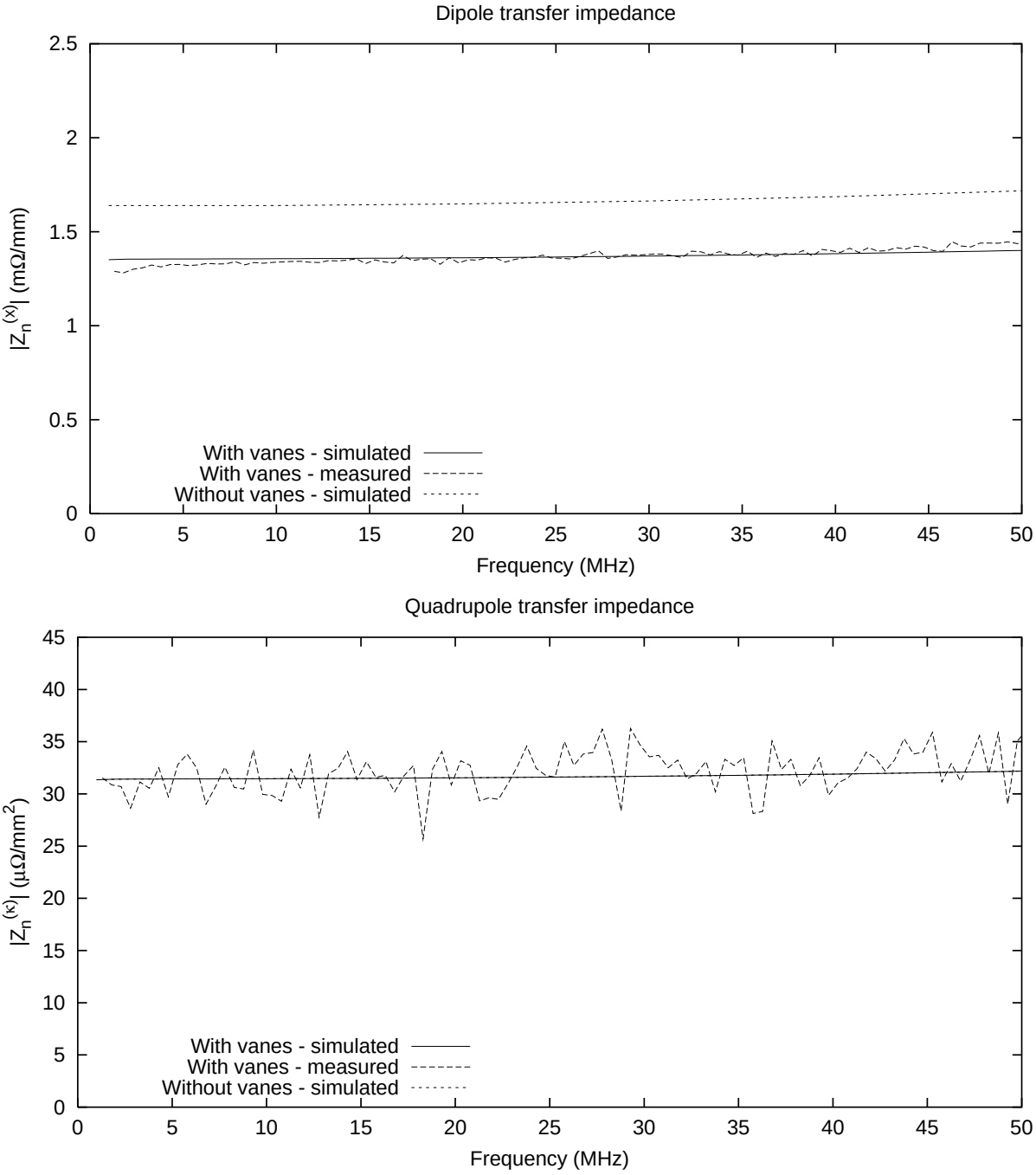

Figure 7.4: Simulated and measured single loop transfer impedances for the lab prototype with thin metal vanes. The simulated values without vanes are shown for comparison. For the quadrupole mode, there is no difference.

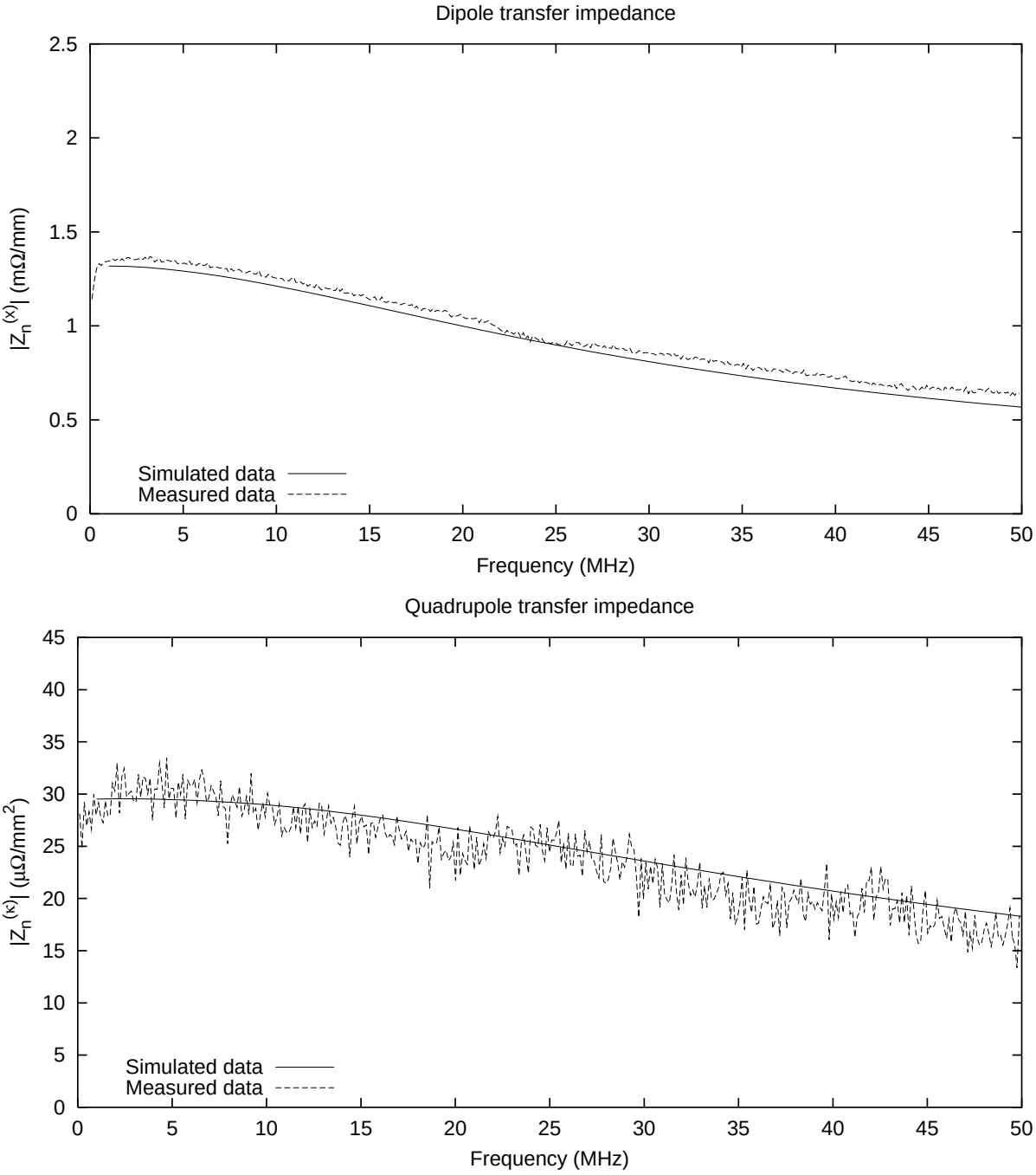

Figure 7.5: Simulated and measured single loop transfer impedances for the pick-up with a coating resistivity of 3.5 Ω.

7.2.1 Antenna Loop Improvements

The common-mode rejection of the initial version of the lab prototype, which had the same antenna loop design as the machine prototype, was rather poor in relative terms (see Fig. 7.6). The largest effect was seen in the Σ signal combination, which is not used. However, also the Ξ and Δ combinations had significant common-mode components. Moreover, the frequency characteristics of these couplings were different from the transfer impedances.

The reason for the common-mode couplings was found to be the placement of the ground point. At high frequencies, the antenna loop must be regarded as a distributed object. The passing beam induces an image current in the two rods parallel to the beam. These currents can be decomposed in parallel and an anti-parallel components. The anti-parallel component is the magnetic induction current, which one wants to measure. The parallel component cancels for low frequencies, because the wavelength is much longer than the length of the loop. At higher frequencies, however, the finite propagation velocity of the induced signals create a phase difference between the signals when they arrive in the transformer, unless it is placed symmetrically. This is why the transformer was placed in a symmetry point. The parallel components then cancel in the transformer, and only the anti-parallel is measured.

However, even if the parallel component does not give a contribution to the current in the primary winding of the transformer, it does contribute to the total charge. It therefore produces a time-varying potential difference between the primary and secondary winding of the read-out transformer. Since there is inevitably some stray capacitive coupling between the two windings, this will induce a signal on the secondary side at high frequencies, and spoil the common mode rejection.

This was solved by moving the ground point to the transformer end of the loop. To do this in a symmetric fashion required an arrangement of three read-out transformers instead of a single one. This new readout design improved the common mode rejection significantly (see Fig. 7.7). The remaining parasitic coupling, mainly due to loop alignment, had a flat frequency response.

7.2.2 Effects of the Coating on the Ceramic

Adding the ceramic with the low-resistance coating, the parasitic couplings were increased strongly (see Fig. 7.8). The source of this was an error in the roundness of the ceramic chamber. This asymmetry couples the field modes, and notably converts part of the monopole field created by the beam to higher order field components. The effect is proportional to the current flowing through the ceramic, which gives the frequency characteristic with a low frequency cut-off at 10 MHz, given by the ratio between the inductance of the cavity and the end-to-end resistance on the ceramic.

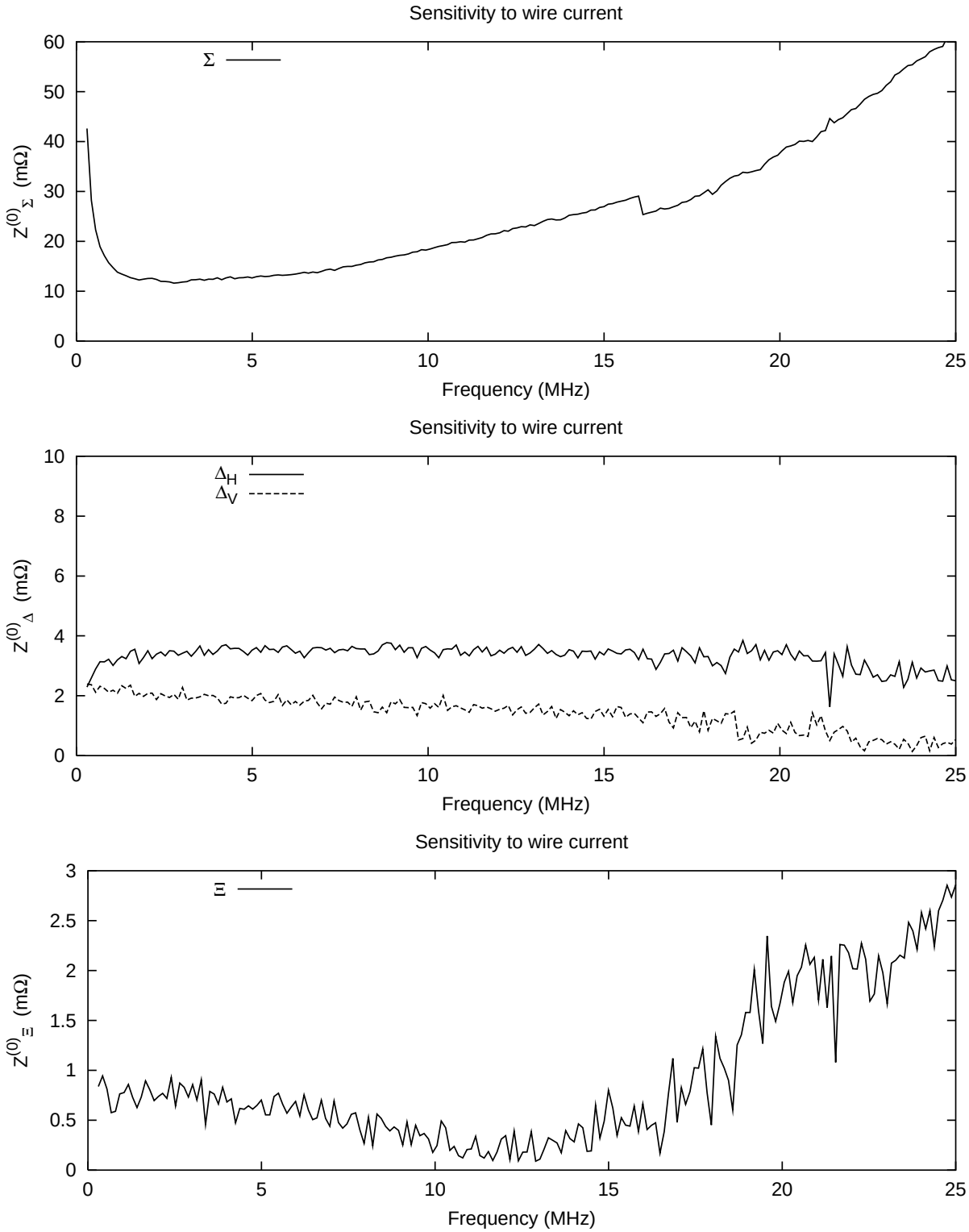

Figure 7.6: Parasitic coupling from a centred wire to the different outputs of the lab prototype with the initial loop design. Note that the frequency characteristics are not flat. (The kink in the upper graph, and the fluctuations in the lower graphs are due to the measurement instrument.)

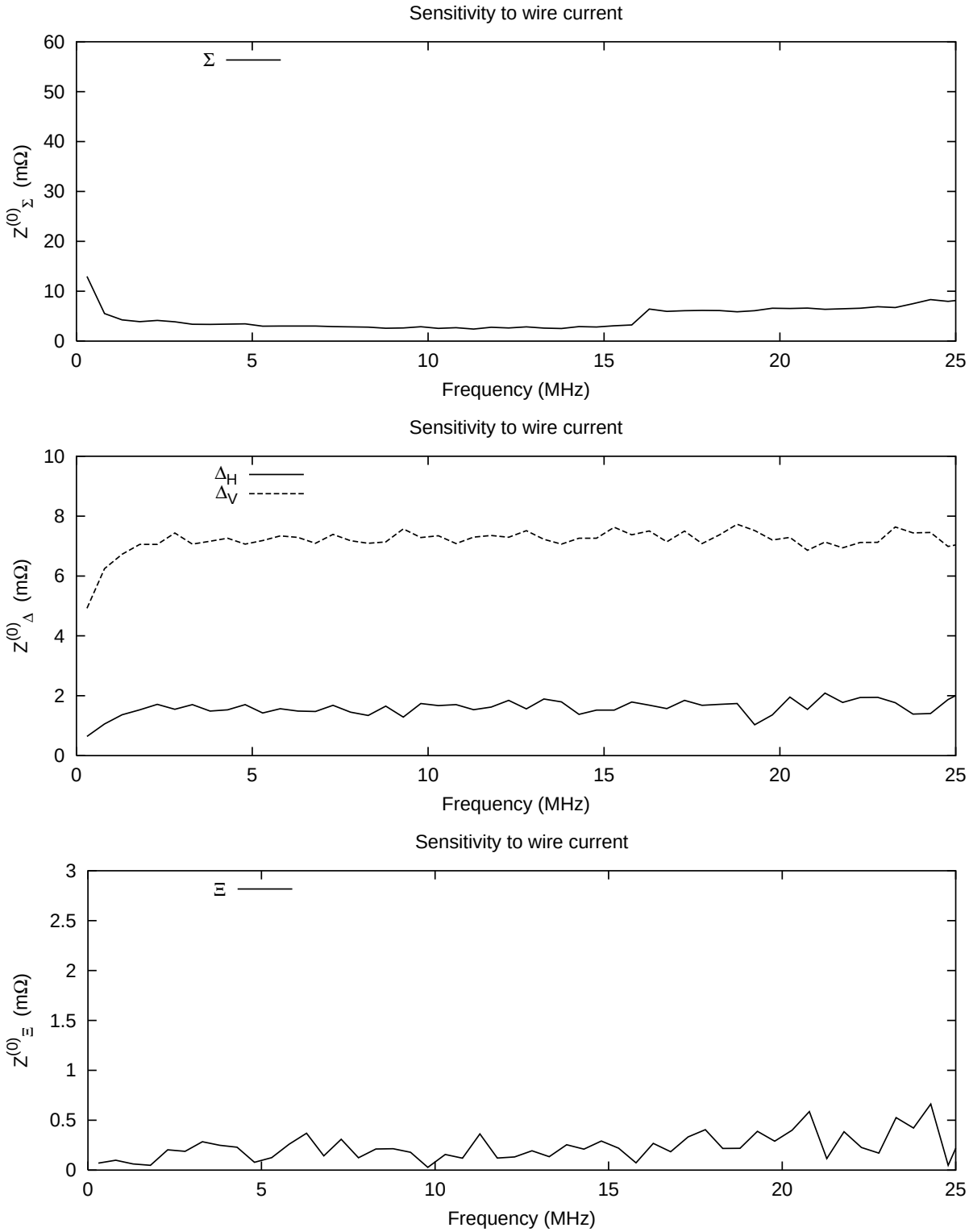

Figure 7.7: Parasitic coupling from a centred wire to the different outputs of the lab prototype with the improved antenna loop design with three transformers. The frequency characteristics is flat, indicating that the coupling is due to antenna offsets. (The kink in the upper graph, and the fluctuations in the lower graphs are due to the measurement instrument.)

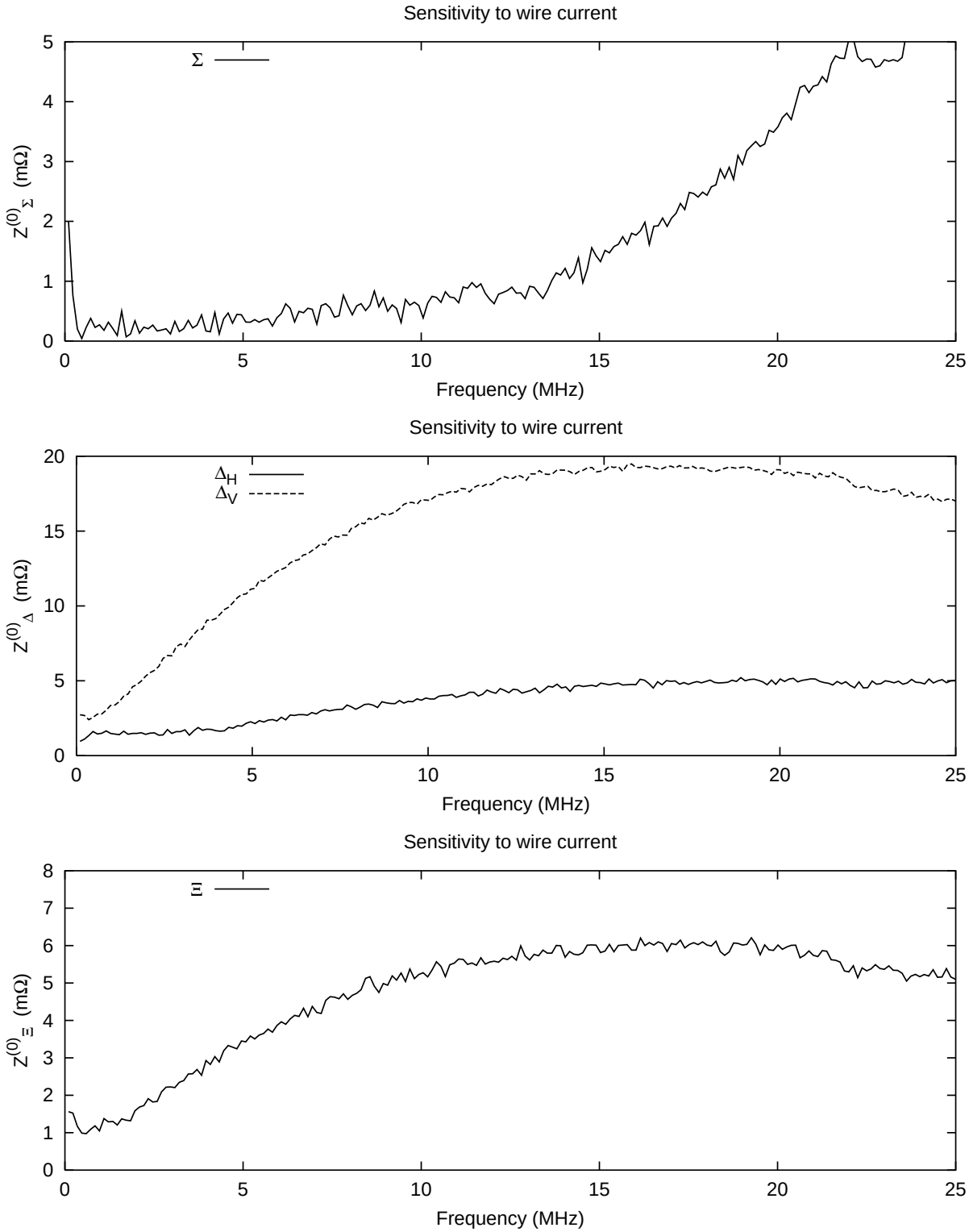

Figure 7.8: Parasitic coupling from a centred wire to the different outputs of the pick-up with a low resistivity coating. The parasitic signals in the Δ and Ξ signals are proportional to the current in the resistive layer, which explains the frequency characteristics.

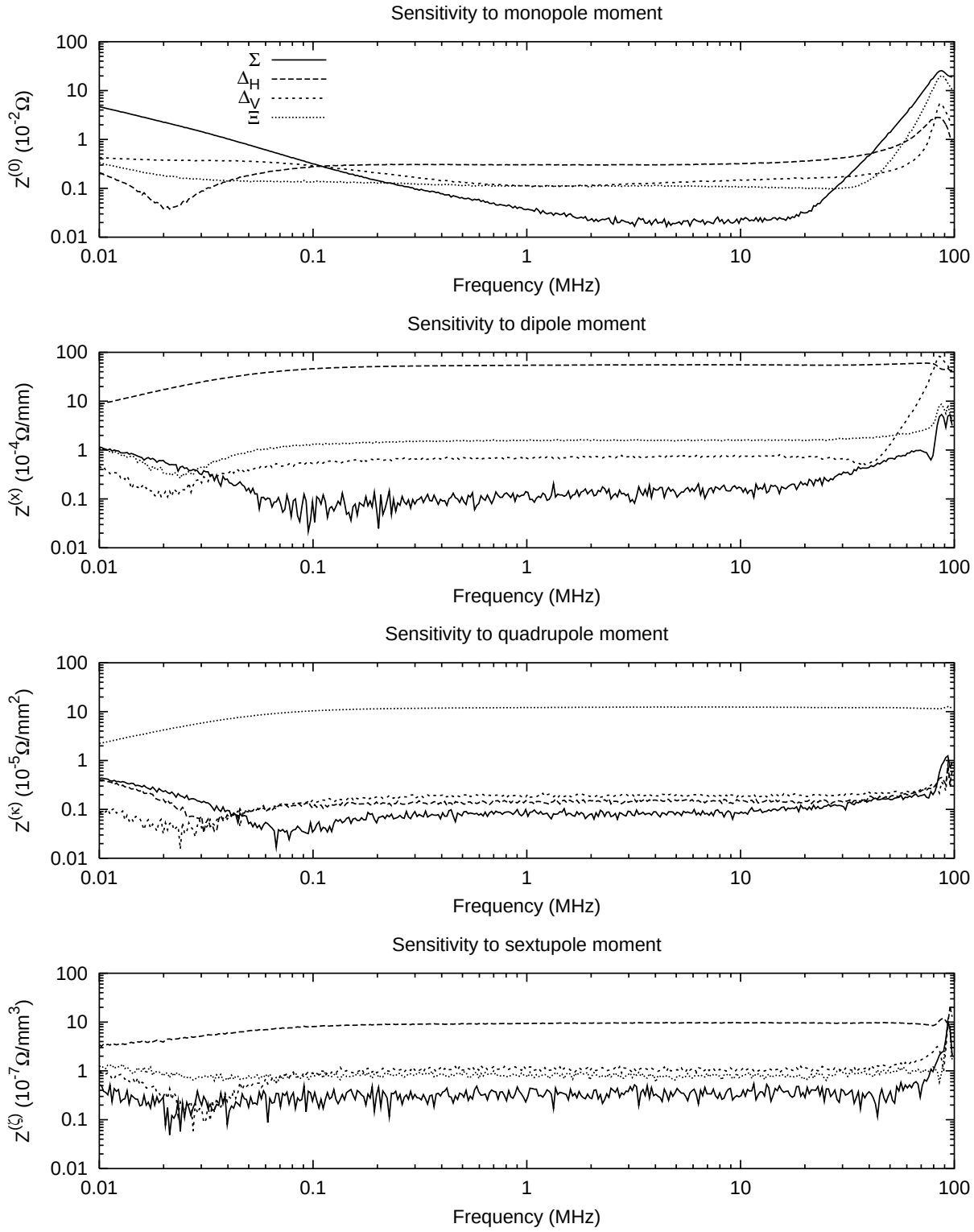

Figure 7.9: Measured couplings from the different antenna moments to the outputs of the final pick-up (with a high resistivity coating). The frequency response is flat, and the parasitic couplings are small. The rise of the common-mode signal in the Σ combination ($Z_\Sigma^{(0)}$) at low frequencies is an instrument effect.

From the magnitude of the measured parasitic couplings, it was estimated that an increase in resistivity by about a factor 100 (about 300 Ω) should reduce the parasitic signals sufficiently. In practice, it was not possible to make a good quality titanium deposition with such a high resistivity, and the design value was therefore reduced to about 80 Ω. With this coating value, the measured transfer impedances (see Fig. 7.9) show a very nice flat frequency response and a good suppression of unwanted couplings.

7.3 Longitudinal Impedance

7.3.1 Simulations

The longitudinal impedance of the "conceptual" pick-up, consisting of only the cavity and antenna loops was simulated as a reference case, and the result is shown in Fig. 7.10. Several sharp peaks are present in the spectrum. These can be divided in two groups, depending on their origin. Antenna loop resonances show up at regular intervals starting at about 150 MHz, with a spacing of approximately 300 MHz, and the cavity-related resonances are grouped together in the high frequency part of the spectrum.

The inclusion of the metal vanes reduced the longitudinal impedance. The low-frequency inductance of the pick-up is reduced by about a factor two, since the path for the wall currents is shortened, and the peak value of the first resonance is reduced by almost the same amount (see Fig. 7.10).

The antenna loop resonances are due to standing waves in the loop. These occur when the length of the loop is a multiple of half a wavelength. The ground point forces a node in one end of the loop. If the loop is a multiple of a whole wavelength, the standing wave has a node also in the other end of the loop, and no effect is seen on the beam. If not, a longitudinal voltage is produced. Since this is a resonant effect, it produces a sharp peak in the longitudinal impedance spectrum. The resonance can be damped by adding a resistor between the end of the loop and ground (the beam pipe). The value of this termination resistor should be small enough to damp the resonance effectively, but large enough not to affect the transfer impedances of the pick-up. Termination resistors of 200 Ω were therefore added and their beneficial effect for the longitudinal impedance can be seen in Fig. 7.10, where all the loop-related resonances are strongly damped.

With a resistive coating, the longitudinal impedance is further reduced. Impedance simulations for the two tested coating resistivities (3.5 Ω and 80 Ω) are showed in Fig. 7.11, and show that also the high-frequency cavity resonances are gone. For the low resistivity case, the impedance is essentially zero, apart from at very low frequencies. For the higher resistivities, the peak at low frequencies is still dominating. The difference between the impedance of the "conceptual" pick-up and the final version with metal vanes, loop terminations and a resistive coating of 80 Ω are several orders of magnitude.

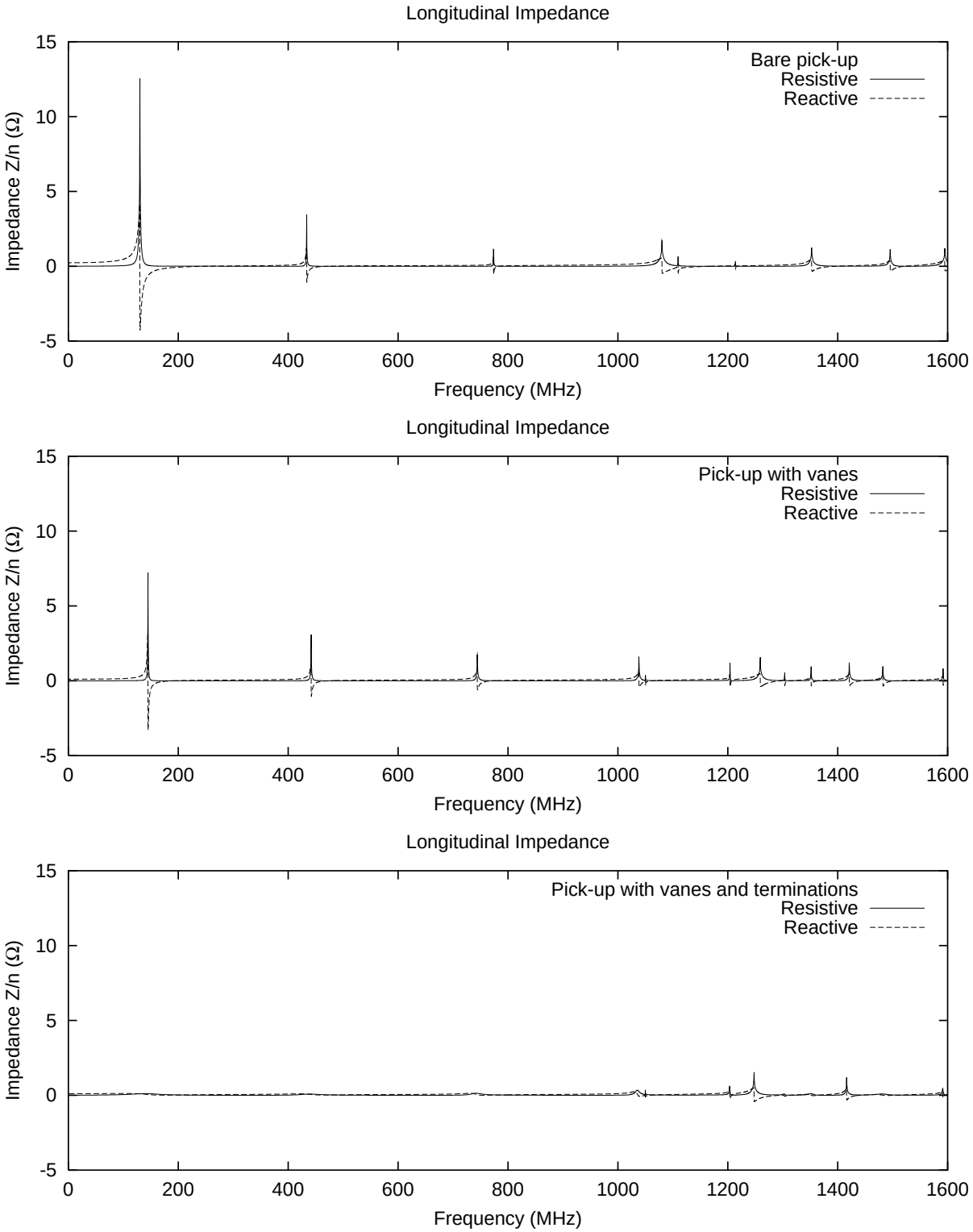

Figure 7.10: Simulated longitudinal impedances. The top graph is for a pick-up without vanes, the middle with vanes, and the bottom graph with vanes and resistive loop terminations.

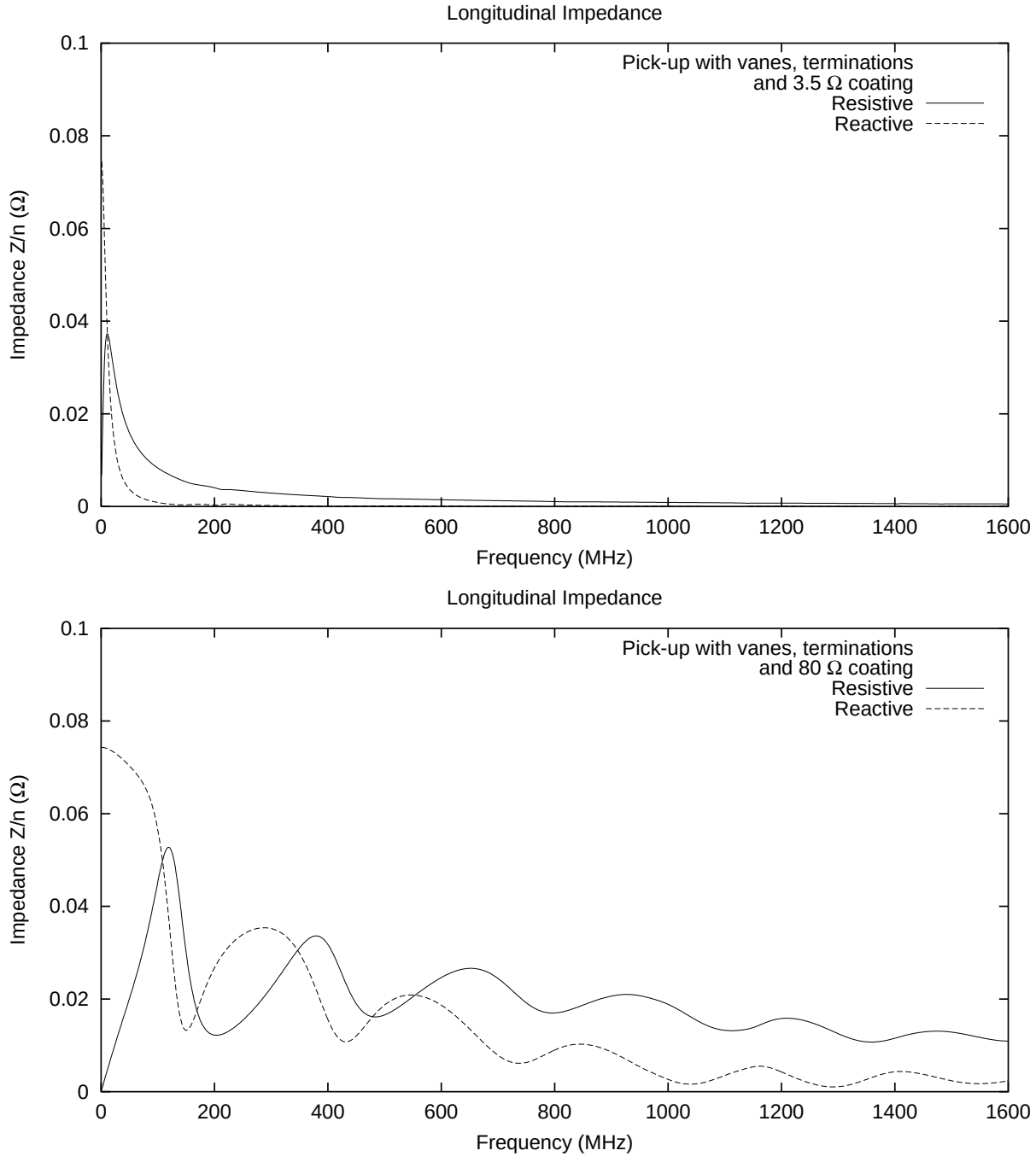

Figure 7.11: Simulated longitudinal impedance for a pick-up with metallic vanes, loop terminations and a resistive coating. The top graph corresponds to a coating of $3.5\,\Omega$*, and the bottom graph* $80\,\Omega$*.*

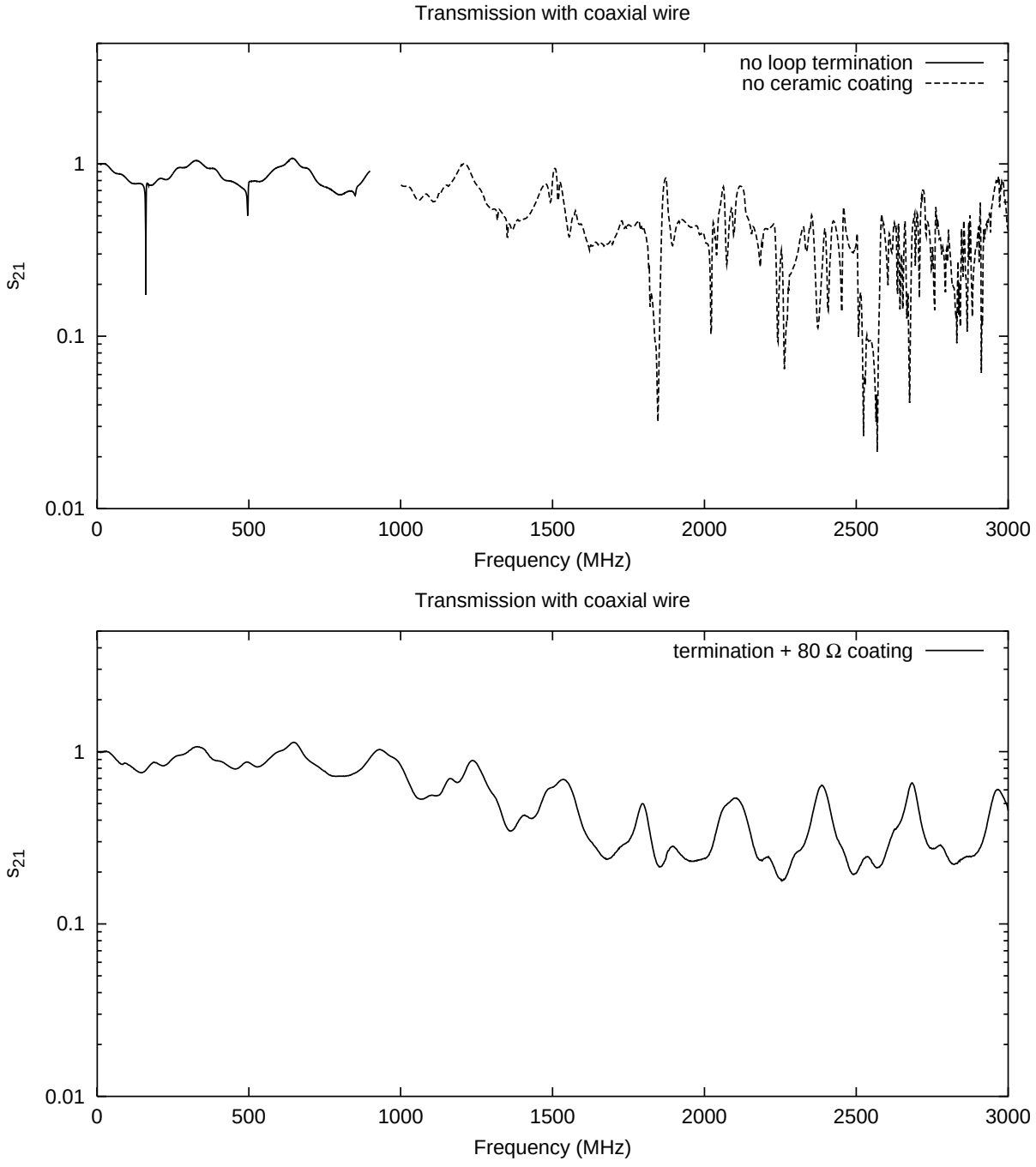

Figure 7.12: Measured transmission through the pick-up measured with a centred wire. The top graph shows the situation without the loop terminations and coating, and the bottom graph the result of their inclusion. The wavy shape of the line is mainly due to mismatch at entry and exit.

7.3.2 Measurements

To measure the longitudinal impedance using the wire method, one needs a reference vacuum chamber of the same length as the object being measured. Also a very good matching between instrument and the object under test is required, in order to avoid a false result. Given the difficulties of the longitudinal impedance measurement, and the good agreement between simulations and measurements in all other cases, it was decided to rely on simulations for the absolute value of the impedance. However, transmission measurement were performed on the different pick-up versions, although without attempting to extract a numerical value of the impedance. The impedance peaks predicted by the simulations could, however, be observed as dips in the signal transmission through the pick-up structure (see Fig. 7.12).

"Errors using inadequate data are much less than those using no data at all"

Charles Babbage

Chapter 8

Beam Measurements

8.1 Analysis of the Measured Data

Beam measurements were performed using the first pick-up prototype. The signal from the four antenna loops of the pick-up were combined in a hybrid circuit and amplified. After being cabled to an adjacent building, the signals from the prototype pick-up was sampled at 500 Ms/s using an eight-bit digital sampling oscilloscope. This oscilloscope was triggered at injection by a timing signal from the PS control system, and could sample up to 250 consecutive turns at maximum sampling rate. The number of turns could be increased by reducing the sampling rate. Since the pick-up design does not allow the beam current to be measured, the signal from a wall current monitor was used as current reference. This monitor was physically situated several magnets downstream of the quadrupole pick-up itself, which is acceptable since the longitudinal bunch shape does not changes significantly in a fraction of a machine turn.

The data from the oscilloscope was read out over the GPIB bus to a LabView program that calculated the beam position and quadrupole moment for a single bunch over a given number of turns. First, a Gaussian curve was fitted to the bunch profile, as measured by the wall current monitor. Then, Gaussian fits were performed on the signals from the pick-up, with position and width fixed by the first fit. This method was found to give less fluctuations than for example integrating the pulse induced by the bunch.

8.2 Beam-based Calibration

8.2.1 Signal Correlations

The quadrupole signal can be calibrated against the dipole signal using the beam. Since the quadrupole moment

$$\kappa = \sigma_x^2 - \sigma_y^2 + \bar{x}^2 - \bar{y}^2 \tag{8.1}$$

is dependent on beam position, one can check that the measured position and quadrupole moments are coherent by plotting the measured values of $x^2 - y^2$ versus κ. Since the beam size oscillations and position oscillations have different decay times, measured data can be selected such that only beam position oscillations are present. Data from measurements taken between 40 and 160 turns after injection is plotted in Fig. 8.1. The slope of the fitted line (0.983) is very close to the ideal value of one.

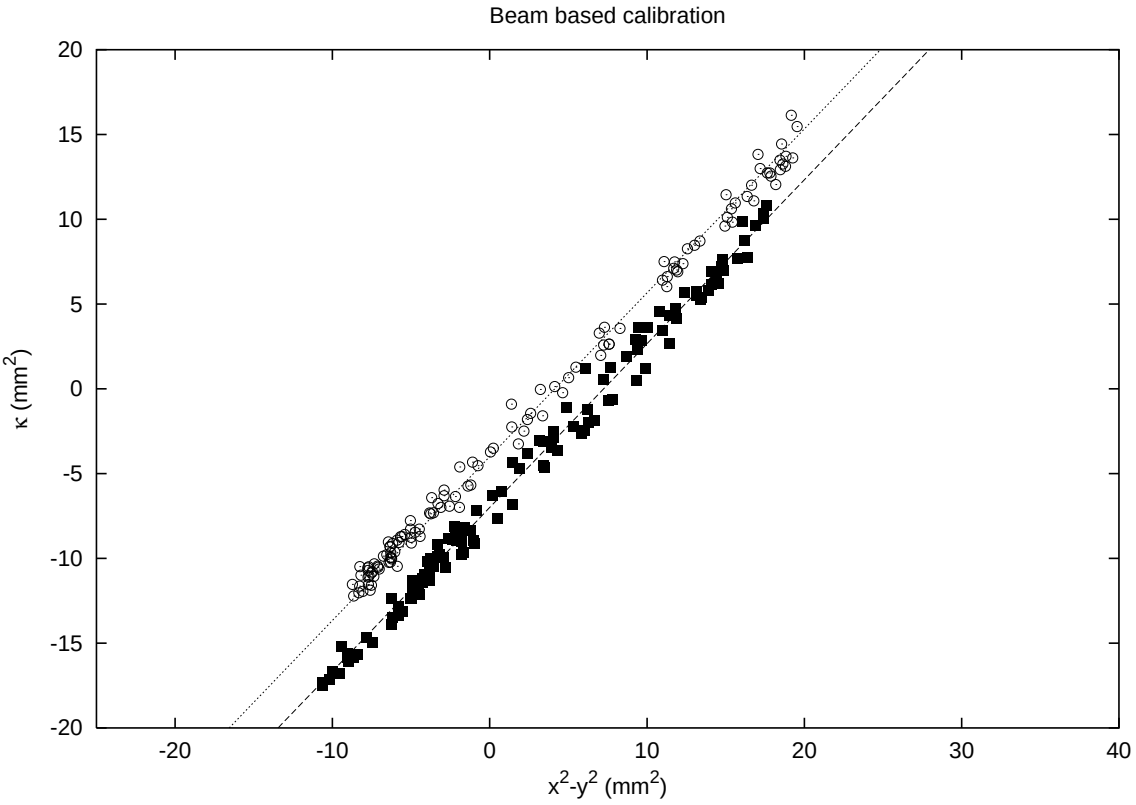

Figure 8.1: Measured quadrupole moment κ versus $x^2 - y^2$, calculated from the measured beam position. Data from two different beam shots are shown. The slope of the lines are 0.983, close to the ideal value of 1.

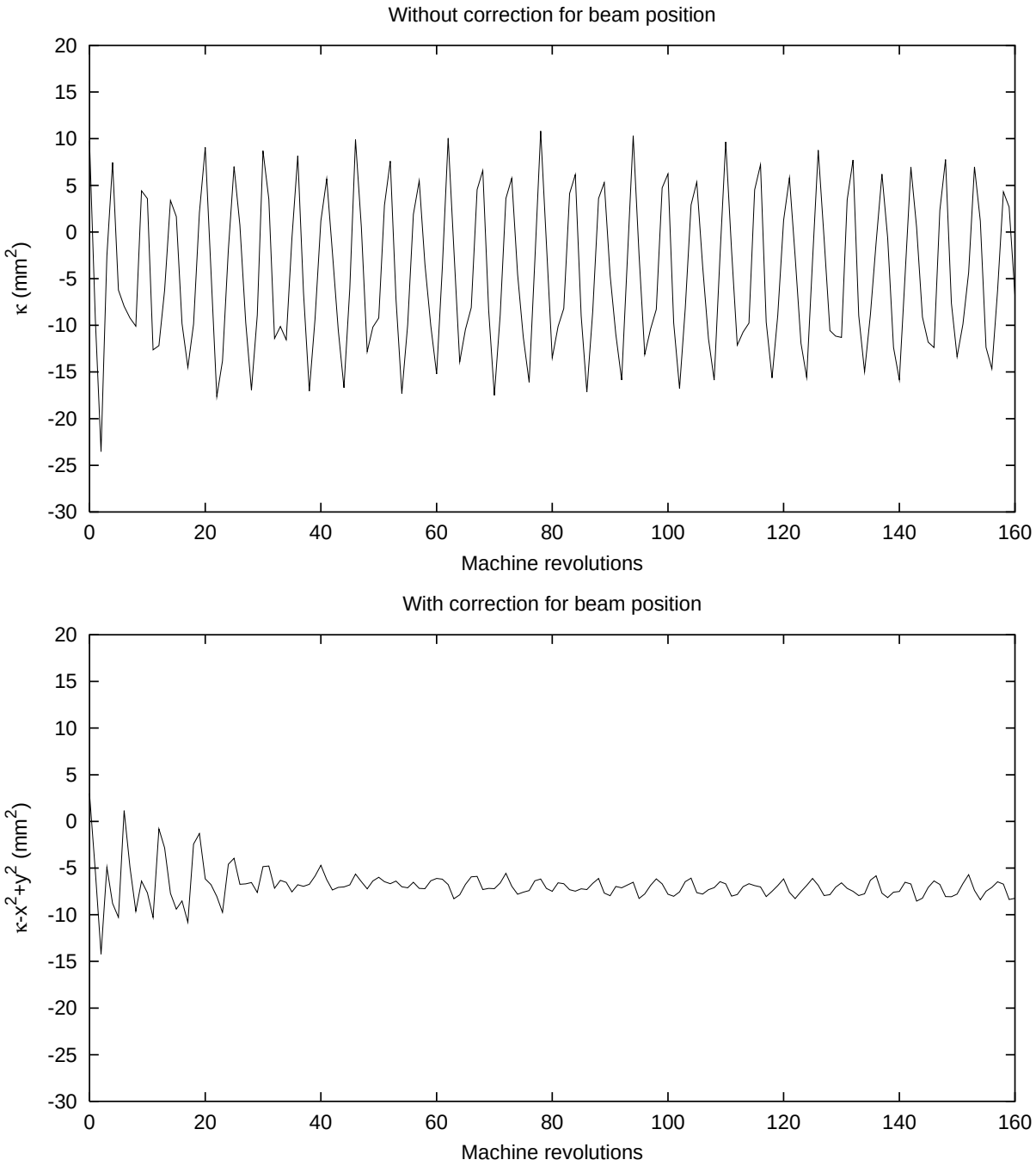

Figure 8.2: Plots of the quadrupole moment κ and the quadrupole antenna moment corrected for the measured beam position.

Once this calibration is verified, the measured quadrupole moment can be corrected for the position term using the measured beam position, resulting in

$$\kappa - \bar{x}^2 + \bar{y}^2 = \sigma_x^2 - \sigma_y^2 \tag{8.2}$$

which is only dependent on beam dimensions. Without the beam position dependence, the signal is much more useful, as illustrated in Fig. 8.2.1 where the same measurement data is plotted with and without correction for the beam position term.

8.2.2 Comparison with Turn-by-Turn SEM-grid

The correlation measurements make sure that the length unit is coherent in the beam position and quadrupole moment measured by the quadrupole pick up, but do not fix this unit. This calibration can be done by comparison with another instrument. One can either compare the amplitude of beam position oscillations measured by a position pick-up with the same amplitude measured by the quadrupole pick-up, or compare the amplitude of beam size oscillation is the same way.

The beam size oscillations measured with the prototype pick-up were compared to the beam size oscillations measured with a turn-by-turn SEM grid. The measurement was made in the horizontal plane, where the beam was oscillating due to a rather large dispersion mismatch between the Booster and the PS. The vertical plane was well matched, which was verified by the absence of any frequency component at the vertical quadrupole frequency in the quadrupole signal. The beam size measured with the SEM grid was then squared and translated in phase to account for the different locations of the instruments (see Fig. 8.3). Due to the dependence of the quadrupole moment on the vertical beam size, The two signals also had to be aligned vertically. The agreement between oscillation amplitudes measured by the two instruments is quite good.

8.3 Sensitivity and Accuracy Estimation

The statistical fluctuations in the quadrupole moment measured by the prototype pick-up were estimated from the noise floor in the Fourier transform of a measurement on a stable, circulating beam. An r.m.s. value of about 0.5 mm^2 was obtained. This is much higher than what would be expected from the measured amplifier noise. It is therefore expected that the noise performance can be significantly improved with the new pick-up design and an optimised acquisition system. However, this noise level is already sufficient to make an emittance measurement as outlined in Chapter 4.

For such an emittance measurement, systematic effects are important. For the prototype, the offset in the measured quadrupole moment was estimated to about 10 mm^2, by comparing with the beam dimensions as measured with SEM-grids. Due to tighter tolerances and improved common mode rejection, this value should also drop significantly for the final version pick-up. Using the bench measurement data, it should be possible to control this offset to better than 1 mm^2.

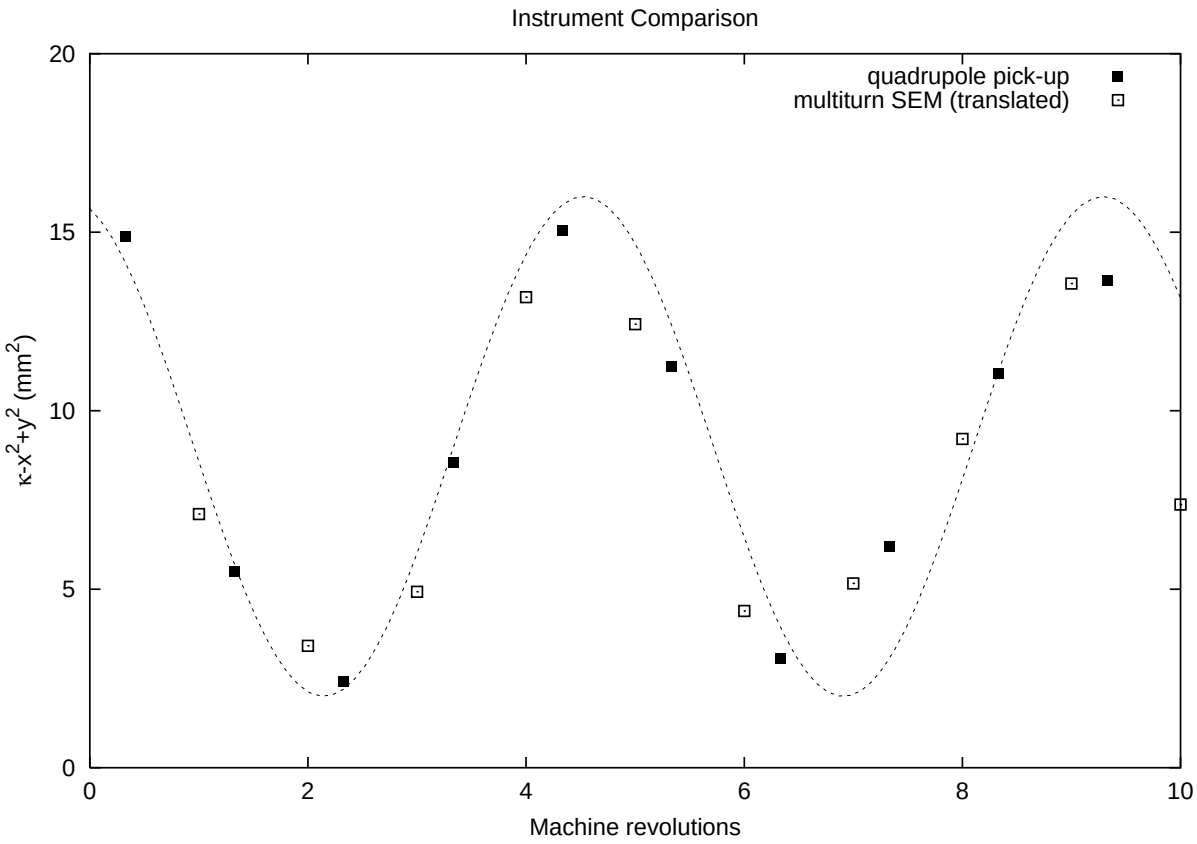

Figure 8.3: Comparative measurement of beam width oscillations after injection in the PS, using the prototype quadrupole pick-up and a turn-by-turn SEM grid. The quadrupole pick-up measurement have been translated vertically. The dashed curve is a sine fit to the first few turns.

8.4 Beam Observations

Since the aim of the prototype pick-up was to demonstrate the new pick-up design idea, no dedicated beam physics studies have been undertaken. However, a number of interesting phenomena have been observed while testing the pick-up on different beams. These are presented here to give an idea of the usefulness of the pick-up.

8.4.1 Coupling

When measuring beam size oscillations at injection of an elliptic beam (horizontal emittance larger the vertical) into a strongly coupled PS machine, a rather large oscillation of the beam size was observed at a frequency given by the tune separation.

Changing the beam ellipticity by varying the number of turns injected in the Booster resulted in a change in amplitude of the signal (see Fig. 8.4). It was therefore interpreted

as a sign of coupling mismatch. Because the normal modes are tilted, an elliptical beam injected in a strongly coupled machine rotates in real space in much the same way as a mismatched phase space ellipse rotates in phase space. An important point is that coupling mismatch creates emittance blow-up, just as any other mismatch. Since linear coupling will be used in a scheme to stabilise the LHC beam in the PS[58], the effect of coupling mismatch at injection should be further studied.

8.4.2 Space Charge Damping and Detuning

The beam size measured by the pick-up is sensitive to the direct space charge, which creates a tune spread within the beam. This tune spread makes the beam size oscillations decohere much faster than position oscillations, that are not sensitive to this effect. Also, the frequency of the beam size oscillation is detuned.

By changing the intensity of the injected beam using a movable sieve, keeping all other beam parameters constant, the change in damping time and frequency could be observed using the prototype pick-up (see Fig. 8.5).

With the very fast damping times that were observed, separation of horizontal and vertical beam size oscillations in frequency domain was not possible, since the damping blurred the peaks and made them overlap. This is a good argument for a SLAC-type measurement setup using two pick-ups, since it needs data from only a few machine turns.

Some attempts were made to evaluate the beam size oscillation frequency as a function of position within the bunch, to see the variation of the space charge forces, but no conclusive results were obtained. This kind of measurement could, however, be possible with the considerably improved final version of the pick-up.

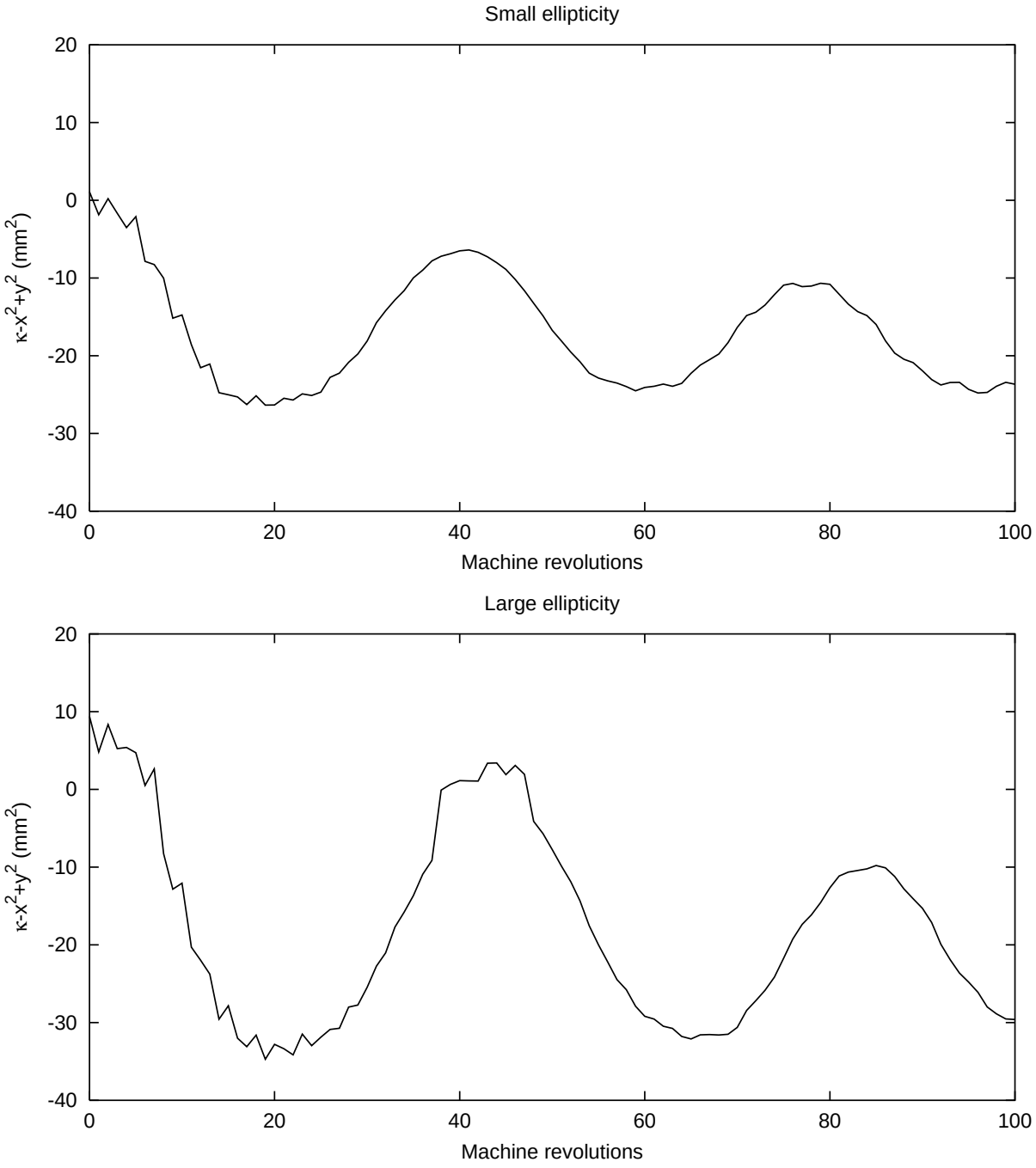

Figure 8.4: Quadrupole moment measured for an elliptic beam at injection into a strongly-coupled PS machine. The horizontal emittance of the injected beam depends on the number of turns used for multi-turn injection in the Booster, whereas the vertical emittance is approximately constant. The top and bottom graphs correspond to 6 and 9 injected turns, respectively. It can be seen that the oscillation amplitude increases with the ellipticity of the beam.

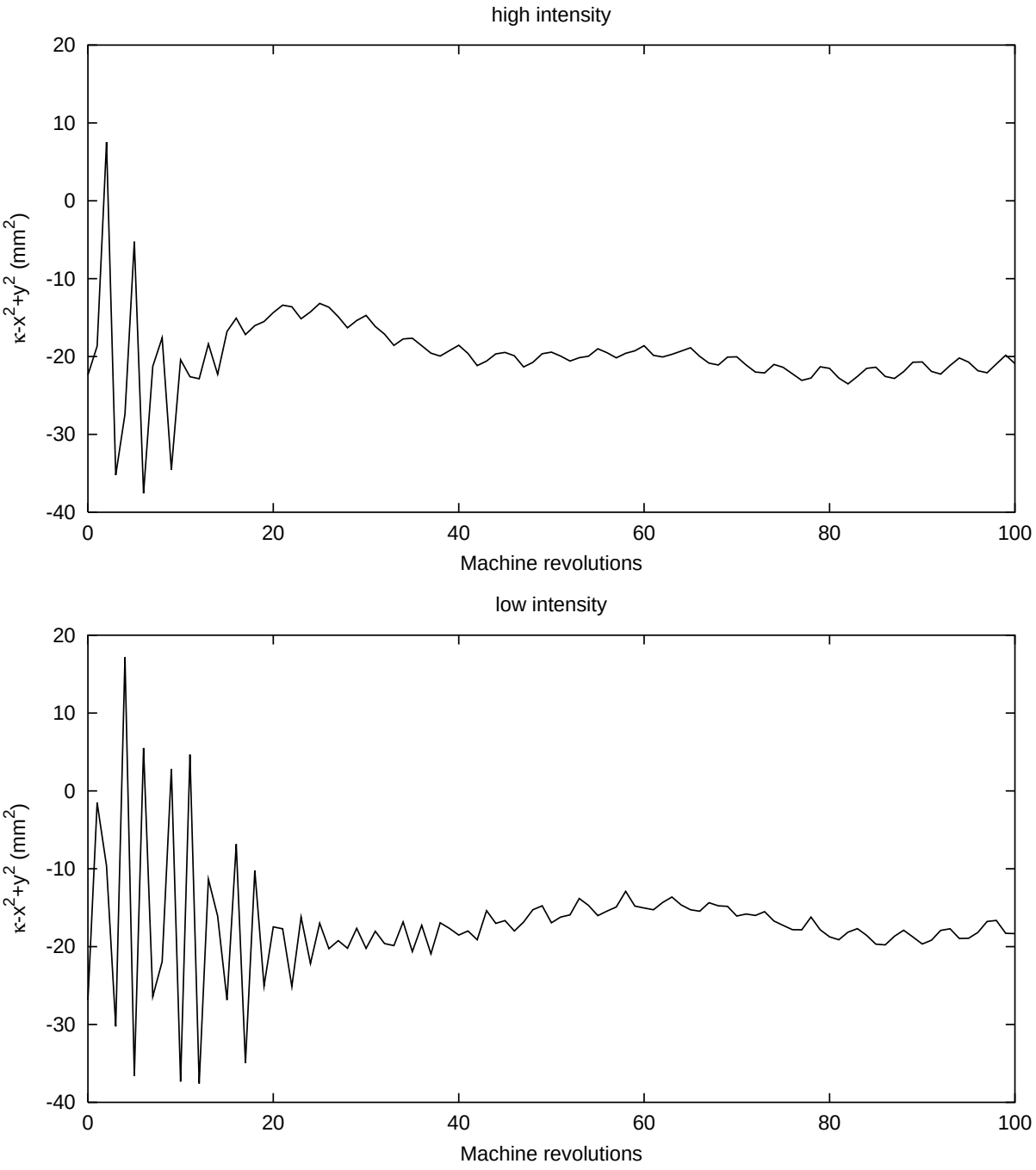

Figure 8.5: Quadrupole moment over the first 100 turns for a deliberately mismatched beam. The difference between the top and bottom graphs is a factor five in intensity. All other beam parameters are the same. It can be clearly seen how the damping time and frequency changes with intensity.

"Prediction is very difficult. Especially about the future."

Niels Bohr

Chapter 9

Summary and Conclusions

9.1 Motivation

For the LHC to reach its design luminosity, the beam brightness is a crucial parameter. To produce a bright beam for the collider, the emittance must be preserved along the injector chain. At each step in the chain, the emittance is allowed to grow by only about 10%. Verification of compliance with this demand poses a problem, since the systematic errors of the standard measurement techniques are of the same order of magnitude.

A large possible contribution to the emittance blow-up is due to optical mismatch at transfer of the beam between two machines in the chain. Apart from emittance blow-up, such mismatch also give rise to an oscillation of the beam size, which could be detected with an appropriate instrument. In order to be useful for continuously monitoring the LHC beam, the instrument has to be non-invasive. Such devices are not commonly available.

A quadrupole pick up is a non-invasive instrument sensitive to beam size, and therefore a candidate for mismatch monitoring. It measures the quadrupole moment

$$\kappa = \sigma_x^2 - \sigma_y^2 + \bar{x}^2 - \bar{y}^2 \tag{9.1}$$

of the beam. Although quadrupole pick-ups have been used before, their success have been hampered by some difficulties. The most important problem is that the very small signal containing the beam size information is embedded in a strong common-mode background. The extraction of the signal is therefore not trivial, and require sophisticated electronics. The problem scale quadratically in the ratio between the beam size and the pick-up aperture, and would be a severe limitation for measuring the small LHC beam in the PS machine, that has a rather large aperture.

9.2 The New Pick-up Design

A new type of quadrupole pick-up, that does not have the above mentioned problem, has been proposed and designed for the PS. The concept is based on measuring the beam-induced magnetic field in the radial direction, which is zero for a centred, symmetric beam. Therefore, there is ideally no common-mode signal. In practice, a common-mode rejection of more than 60 dB was obtained, with respect to a "conventional" quadrupole pick-up with the same aperture. The small remaining common-mode signal can be calibrated away using reference measurements.

Analytic expressions for the dependence of the pick-up transfer impedances on the basic design parameters have been derived. A good agreement between analytic, simulated, and measured results have been observed, suggesting that the basic properties are well understood.

Early on in the development process, a non-optimised proof-of-principle pick-up was built and installed in the PS machine, and has produced encouraging results with beam.

Studies on a prototype in the laboratory resulted in a significant reduction in unwanted parasitic couplings, e.g. by improving the readout of the current induced in the antenna loops. With the help of numerical simulations, the longitudinal impedance of the pick-up could be reduced by several orders of magnitude, as compared to the initial "conceptual" design.

The final pick-up, designed with the experience from lab tests and simulations, has a single loop transfer impedance to the quadrupole moment of $30\,\mu\Omega/\mathrm{mm}^2$, a transfer impedance to the dipole moment of $1.35\,\mathrm{m}\Omega/\mathrm{mm}$, and a longitudinal impedance Z/n that is less than $80\,\mathrm{m}\Omega$ in the entire spectrum up to 1.6 GHz. The bandwidth of the pick-up ranges from 70 KHz to more than 25 MHz, which corresponds to the bunch spectrum at PS injection.

9.3 Emittance and Matching Measurement

Measurement of emittance and optical parameters using quadrupole pick-ups have already been demonstrated in electron LINACs. Given the performance of the new pick-up design, these measurement methods can be adapted to the PS. For this, two pick-ups are needed.

Since the beam is circulating, the statistical measurement error can be reduced by using data from several consecutive machine turns. The periodicity of a circular machine also reduces the number of input parameters that are needed for the measurement, and the systematic errors should therefore be reduced with respect to the LINAC case. Moreover, many of these parameters are properties of the ring that can relatively easily be measured.

Error analysis of these methods show that already the performance of the proof-of-principle prototype tested in the PS was sufficient to measure the emittance of a single bunch in a circulating beam with an accuracy comparable to conventional methods, provided any pick-up offsets can be corrected for.

Two pick-ups of the final design have just been installed in the PS machine, and will

be commissioned when the machine starts up (spring 2001). Apart from the possibility of non-invasive emittance and matching measurements, these pick-ups will also provide an interesting tool for other beam studies, since they allow for the non-invasive measurement of transverse beam size also later in the acceleration cycle.

9.4 Further Possibilities

The basic pick-up design idea described in this report is applicable to any machine, and could be useful e.g. in the other machines in the LHC injector chain. However, the pick-up design has been optimised for injection studies in the PS machine, and would have to be modified for use in a different machine.

There are mainly two properties that are machine specific: the pick-up aperture and its required bandwidth. The aperture can be modified relatively easily, but to significantly increase the bandwidth might be more complicated. Still, the pick-up design was not yet optimised for a high bandwidth. The low-frequency response of the pick-up may be improved either by increasing the inductance of the antenna loop (i.e. making the pick-up longer) or reducing its load by increasing the turns ratio on the current transformers. In the high-frequency end, the limitation of the PS pick-up is the strong common-mode signal at the loop resonance. Pushing this resonance towards higher frequencies by shortening the loop would probably improve the situation. However, this would affect the low frequency response by reducing the inductance. In practice, increasing the bandwidth therefore means reduced transfer impedances. To test the limits, further studies are needed.

"We are getting into semantics again. If we use words, there is a very grave danger they will be misinterpreted."

H.R. Haldeman

Appendix A

Symbols and Acronyms

A.1 Symbols

The following table gives a listing of the symbols used in this report.

Symbol	Description
x, y	Position with respect to the reference trajectory
x', y'	Angle with respect to the reference trajectory
σ	Beam size
α	Twiss alpha parameter
β	Twiss beta parameter
γ	Twiss gamma parameter
ε	Statistical (r.m.s.) emittance
ε_N	Normalised r.m.s. emittance
D	Dispersion function
D'	Derivative of dispersion function
Q	Machine tune
Q'	Chromaticity
ν	Machine tune measured in radians
μ	Betatron phase advance
s	Longitudinal position along beam trajectory
S	Element 11 of the transfer matrix
C	Element 12 of the transfer matrix
c	Speed of light
β_{L}	Lorenz beta factor
γ_{L}	Lorenz gamma factor
κ	Quadrupole moment of the beam
κ'	Skew quadrupole moment of the beam
ζ	Sextupole moment of the beam

Symbol	Description
ζ'	Skew Sextupole moment of the beam
Z	Impedance
M	Inductance

A.2 Acronyms used in the text

Acronym	Meaning
CCD	Charge-Coupled Device
CERN	European Organization for Nuclear Research
LINAC	Linear Accelerator
PSB	Proton Synchrotron Booster
PS	CERN 26 GeV Proton Synchrotron
SPS	CERN Super Proton Synchrotron
LHC	Large Hadron Collider
SLAC	Stanford Linear Accelerator Centre
SLC	SLAC Linear Collider
SM	Standard Model
r.m.s.	Root-mean-square (Standard deviation)
TRIUMF	Tri-University Meson Facility
TNT	Tri-Nitro-Toluene
MCP	Micro-channel Plate
GPIB	General Purpose Interface Bus
FEM	Finite Element Method
OTR	Optical Transition Radiation

Appendix B

Quadrupole signal components

The quadrupole moment κ measured by a quadrupole pick-up can be expanded in terms of the optical parameters as

$$\kappa = \sigma_x^2 - \sigma_y^2 + x^2 - y^2 = \underbrace{\varepsilon_x\beta_x - \varepsilon_y\beta_y}_{\text{betatron part}} + \underbrace{\sigma_p^2 D_x^2 - \sigma_p^2 D_y^2}_{\text{dispersion part}} + \underbrace{x^2 - y^2}_{\text{position part}} \tag{B.1}$$

If the beam injected in a machine is not matched to the receiving machine in terms of Twiss values, dispersion and trajectory, its quadrupole moment will oscillate as a function of machine turn. The behaviour of the different terms can be calculated from the one-turn transfer matrix in Eq. (2.11).

The contribution of the horizontal beam position to the quadrupole moment is

$$\begin{aligned} x_n^2 &= (C_x\Delta x + S_x\Delta x' + \bar{x})^2 \\ &= \left(\bar{x} + (\cos\nu_x n + \bar{\alpha}_x \sin\nu_x n)\Delta x + \bar{\beta}_x \sin\nu_x n \Delta x'\right)^2 \\ &= \left(\bar{x} + \Delta x \cos\nu_x n + (\bar{\beta}_x\Delta x' + \bar{\alpha}_x\Delta x)\sin\nu_x n\right)^2 \\ &= \left(\bar{x} + \sqrt{\bar{\beta}_x}\delta_x \cos(\nu_x - \phi_x)\right)^2 \\ &= \bar{x}^2 + \frac{1}{2}\,\bar{\beta}_x\,\delta_x^2 + 2\,\bar{x}\,\sqrt{\bar{\beta}_x}\,\delta_x\,\cos(\nu_x - \phi_x) + \frac{1}{2}\,\bar{\beta}_x\,\delta_x^2\,\cos(2\nu_x - 2\phi_x) \end{aligned} \tag{B.2}$$

where δ_x and ϕ_x are the modulus and angle of the normalised missteering vector

$$\vec{\delta}_x = \frac{1}{\sqrt{\bar{\beta}_x}}\begin{pmatrix}\Delta x \\ \bar{\beta}_x\Delta x' + \bar{\alpha}_x\Delta x\end{pmatrix} = \begin{pmatrix}\dfrac{\Delta x}{\sqrt{\bar{\beta}_x}} \\ \sqrt{\bar{\beta}_x}\Delta x' + \bar{\alpha}_x\dfrac{\Delta x}{\sqrt{\bar{\beta}_x}}\end{pmatrix} \tag{B.3}$$

calculated at the first beam passage ($n = 0$). Barred parameters refer to the machine properties (lattice beta, closed orbit etc). The first term in Eq. (B.2) is just the closed orbit contribution. The second term is also a constant and has the form of an emittance

(proportional to the lattice beta). It represents, in fact, the emittance blow-up due to missteering[34]

$$\Delta\varepsilon_x = \frac{1}{2}\delta_x^2. \tag{B.4}$$

Two oscillating terms are present if the missteering is non-zero. The amplitude of the signal component at the betatron frequency is proportional to the closed orbit position in the pick-up and therefore vanishes when the two are well aligned. The result for the vertical position is obtained just by changing the appropriate indexes.

The corresponding result for the horizontal dispersion term is obtained in a very similar way.

$$\begin{aligned}
\sigma_{\mathrm{p}}^2 {D_x}_n^2 &= (C_x\Delta D_x + S_x\Delta D_x' + \bar{D}_x)^2 \\
&= \sigma_{\mathrm{p}}^2\left(\bar{D}_x + (\cos\nu_x n + \bar{\alpha}_x \sin\nu_x n)\Delta D_x + \bar{\beta}_x \sin\nu_x n \Delta D_x'\right)^2 \\
&= \sigma_{\mathrm{p}}^2\left(\bar{D}_x + \Delta D_x \cos\nu_x n + (\bar{\beta}_x\Delta D_x' + \bar{\alpha}_x\Delta D_x)\sin\nu_x n\right)^2 \\
&= \sigma_{\mathrm{p}}^2\left(\bar{D}_x + \sqrt{\bar{\beta}_x}\delta_{D_x}\cos(\nu_x - \phi_{D_x})\right)^2 \\
&= \sigma_{\mathrm{p}}^2\,\bar{D}_x^2 + \frac{1}{2}\,\sigma_{\mathrm{p}}^2\,\bar{\beta}_x\,\delta_{D_x}^2 + \\
&\quad 2\,\sigma_{\mathrm{p}}^2\,\bar{D}_x\sqrt{\bar{\beta}_x}\,\delta_{D_x}\,\cos(\nu_x - \phi_{D_x}) + \frac{1}{2}\,\sigma_{\mathrm{p}}^2\,\bar{\beta}_x\,\delta_{D_x}^2\,\cos(2\nu_x - 2\phi_{D_x})
\end{aligned} \tag{B.5}$$

where δ_x and ϕ_{Dx} are the modulus and angle of the dispersion mismatch vector

$$\vec{\delta}_{D_x} = \frac{1}{\sqrt{\bar{\beta}_x}}\begin{pmatrix}\Delta D_x \\ \bar{\beta}_x\Delta D_x' + \bar{\alpha}_x\Delta D_x\end{pmatrix} = \begin{pmatrix}\frac{\Delta D_x}{\sqrt{\bar{\beta}_x}} \\ \sqrt{\bar{\beta}_x}\Delta D_x' + \bar{\alpha}_x\frac{\Delta D_x}{\sqrt{\bar{\beta}_x}}\end{pmatrix} \tag{B.6}$$

also calculated at the first beam passage ($n = 0$). Analogous to the case of beam position, the first term in Eq. (B.2) is the lattice dispersion contribution and the second term represents the emittance blow-up due to dispersion mismatch[34]

$$\Delta\varepsilon_x = \frac{1}{2}\sigma_{\mathrm{p}}^2\delta_D^2. \tag{B.7}$$

As in the previous case, two oscillating terms are present if the dispersion is not matched. The amplitude of the signal component at the betatron frequency vanishes when the lattice dispersion at the position of the pick-up is zero. The result for the vertical dispersion is obtained just by changing the appropriate indexes. In this case, however, the lattice dispersion is zero in conventional rings, so the signal component at the betatron frequency is absent.

The evolution of the betatron part can be calculated from Eq. (2.12)

$$\begin{aligned}
\epsilon_x\beta_{xn} &= \tilde{\varepsilon}_x(C_x^2\tilde{\beta}_x - 2C_xS_x\tilde{\alpha}_x + S_x^2\tilde{\gamma}_x) \\
&= \tilde{\varepsilon}_x\tilde{\beta}_x(\cos\nu_x n + \bar{\alpha}_x\sin\nu_x n)^2 - 2\tilde{\varepsilon}_x\tilde{\alpha}_x(\cos\nu_x n + \bar{\alpha}_x\sin\nu_x n)\bar{\beta}_x\sin\nu_x n + \\
&\quad +\tilde{\epsilon}_x\tilde{\gamma}_x(\bar{\beta}_x\sin\nu_x n)^2 \\
&= \tilde{\varepsilon}_x\frac{1}{2}(\bar{\beta}_x\tilde{\gamma}_x + \bar{\gamma}_x\tilde{\beta}_x - 2\bar{\alpha}_x\tilde{\alpha}_x)\bar{\beta}_x + + \qquad \text{(B.8)} \\
&\quad +\tilde{\varepsilon}_x\bar{\beta}_x\left(\left(\frac{\tilde{\beta}_x}{\bar{\beta}_x} - \frac{1}{2}(\bar{\beta}_x\tilde{\gamma}_x + \bar{\gamma}_x\tilde{\beta}_x - 2\bar{\alpha}_x\tilde{\alpha}_x)\right)\cos 2\nu_x n + \frac{\bar{\alpha}_x\tilde{\beta}_x - \tilde{\alpha}_x\bar{\beta}_x}{\bar{\beta}_x}\sin 2\nu_x n\right)
\end{aligned}$$

where the tilde above a symbol refers to a parameter of the injected beam. The constant term is the ordinary emittance term, where the injected emittance is increased by a blow-up factor

$$\frac{\tilde{\bar{\varepsilon}}_x}{\bar{\varepsilon}_x} = 1 + \frac{\Delta\varepsilon_x}{\bar{\varepsilon}_x} = \frac{1}{2}(\bar{\beta}_x\tilde{\gamma}_x + \bar{\gamma}_x\tilde{\beta}_x - 2\bar{\alpha}_x\tilde{\alpha}_x) \qquad \text{(B.9)}$$

in the case of betatron mismatch. There is only one oscillating term at twice the betatron frequency. The amplitude of this oscillation is

$$\begin{aligned}
\delta_{\beta_x}^2 &= \left(\frac{\tilde{\beta}_x}{\bar{\beta}_x} - 1 - \frac{\Delta\varepsilon_x}{\bar{\varepsilon}_x}\right)^2 + \left(\frac{\bar{\alpha}_x\tilde{\beta}_x - \tilde{\alpha}_x\bar{\beta}_x}{\bar{\beta}_x}\right)^2 \\
&= \frac{\tilde{\beta}_x}{\bar{\beta}_x}\left(\frac{1}{2}\left(\bar{\beta}_x\tilde{\gamma}_x + \bar{\gamma}_x\tilde{\beta}_x - 2\bar{\alpha}_x\tilde{\alpha}_x\right) - 1\right) - \left(\frac{\tilde{\beta}_x}{\bar{\beta}_x} - 1\right)\frac{\Delta\varepsilon_x}{\bar{\varepsilon}_x} + \left(\frac{\Delta\varepsilon_x}{\bar{\varepsilon}_x}\right)^2 \\
&= \frac{\Delta\varepsilon_x}{\bar{\varepsilon}_x} - \frac{\Delta\beta_x}{\bar{\beta}_x}\frac{\Delta\varepsilon_x}{\bar{\varepsilon}_x} + \left(\frac{\Delta\varepsilon_x}{\bar{\varepsilon}_x}\right)^2 \approx \frac{\Delta\varepsilon_x}{\bar{\varepsilon}_x} \qquad \text{(B.10)}
\end{aligned}$$

where the last approximation is valid for small mismatch (small emittance blow-up). Under similar conditions one can approximate

$$\vec{\delta}_{\beta_x} \approx \begin{pmatrix} \dfrac{\tilde{\beta}_x}{\bar{\beta}_x} - 1 \\ \dfrac{\bar{\alpha}_x\tilde{\beta}_x - \tilde{\alpha}_x\bar{\beta}_x}{\bar{\beta}_x} \end{pmatrix} = \begin{pmatrix} \dfrac{\Delta\beta_x}{\bar{\beta}_x} \\ \bar{\alpha}_x\dfrac{\Delta\beta_x}{\bar{\beta}_x} - \Delta\alpha_x \end{pmatrix} \qquad \text{(B.11)}$$

Again, the corresponding equations for the vertical plane are obtained by changing indices.

Putting all the partial results together yields for the quadrupole moment as a function of turn

$$\begin{aligned}\kappa_n = {} & \bar{\beta}_x(\varepsilon_x + \Delta\varepsilon_x) - \bar{\beta}_y(\varepsilon_y + \Delta\varepsilon_y) + \bar{D}_x^2\,\sigma_\mathrm{p}^2 + \bar{x}^2 - \bar{y}^2 \\ & + \bar{\beta}_x\left(\varepsilon_x\delta_{\beta_x}\cos(2\nu_x n - \phi_{\beta_x}) + \sigma_\mathrm{p}^2\delta_{D_x}^2\cos(2\nu_x n - 2\phi_{D_x}) + \delta_x^2\cos(2\nu_x n - 2\phi_x)\right) \\ & - \bar{\beta}_y\left(\varepsilon_y\delta_{\beta_y}\cos(2\nu_y n - \phi_{\beta_y}) + \sigma_\mathrm{p}^2\delta_{D_y}^2\cos(2\nu_y n - 2\phi_{D_y}) + \delta_y^2\cos(2\nu_y n - 2\phi_y)\right) \\ & + \sqrt{\bar{\beta}_x}\left(\sigma_\mathrm{p}^2 D_x\,\delta_{D_x}\cos(\nu_x n - \phi_{D_x}) + \bar{x}\,\delta_x\cos(\nu_x n - \phi_x)\right) \\ & - \sqrt{\bar{\beta}_y}\,\bar{y}\,\delta_y\sin(\nu_y n - \phi_y) \end{aligned} \tag{B.12}$$

where the emittance increase is given by

$$\Delta\varepsilon_x \approx \varepsilon_x\frac{\delta_{\beta_x}^2}{2} + \sigma_\mathrm{p}^2\frac{\delta_{D_x}^2}{2} + \frac{\delta_x^2}{2} \tag{B.13}$$

$$\Delta\varepsilon_y \approx \varepsilon_y\frac{\delta_{\beta_y}^2}{2} + \sigma_\mathrm{p}^2\frac{\delta_{D_y}^2}{2} + \frac{\delta_y^2}{2} \tag{B.14}$$

Appendix C

Error analysis of Matrix Method

The matrix equation can be expanded using singular value decomposition as

$$\vec{k} = R^T \cdot \Lambda \cdot L \cdot \vec{e} \tag{C.1}$$

where R and T are row orthogonal matrices, and Λ is a diagonal matrix containing the singular values λ_i. The solution can be written

$$\vec{e} = L^T \cdot \Lambda^{-1} \cdot R \cdot \vec{k} \tag{C.2}$$

where singular values equal to zero, and their corresponding solution space, have been removed. In order to properly solve the system, one needs to have as many non-zero singular values as there are components in the vector e (six in this case). Since the matrix R is row-orthogonal, it will distribute any uncorrelated noise power in the vector evenly, such that the average noise power in a component of $\vec{k}$ equals the average noise power in a component of $R \cdot \vec{k}$. This noise is then amplified by a factor λ^{-1} and distributed over the result $\vec{e}$ by the matrix L. The main noise contribution comes from the smallest singular value λ_6 (if by convention the singular values are ordered in decreasing order)

$$\Delta\vec{e} \propto \vec{l}_6 \lambda_6^{-1} |\Delta k| \tag{C.3}$$

The emittance in calculated from (4.12), which gives

$$\begin{aligned} \Delta\epsilon_x &= \frac{\partial\epsilon_x}{\partial e_1}\Delta e_1 + \frac{\partial\epsilon_x}{\partial e_2}\Delta e_2 + \frac{\partial\epsilon_x}{\partial e_3}\Delta e_3 = \\ &= \frac{1}{2}\frac{e_3}{\sqrt{e_1 e_3 - e_2^2}}\Delta e_1 - \frac{1}{2}\frac{2e_2}{\sqrt{e_1 e_3 - e_2^2}}\Delta e_2 + \frac{1}{2}\frac{e_1}{\sqrt{e_1 e_3 - e_2^2}}\Delta e_3 \end{aligned} \tag{C.4}$$

using the definition of $\vec{e}$ in (4.10),this gives

$$\Delta\epsilon_x = \frac{1}{2}(\gamma_x \Delta e_1 - 2\alpha_x \Delta e_2 + \beta_x \Delta e_3) \tag{C.5}$$

from which the error can be estimated.

$$\Delta\epsilon_x \approx \frac{1}{2}(\gamma_x l_{61} - 2\alpha_H l_{62} + \beta_H l_{63})\lambda_6^{-1}|\Delta k| \tag{C.6}$$

To get a more accurate estimations, the square sum of the (uncorrelated) contributions from all the singular values can be made

$$\Delta\epsilon_x \approx \frac{1}{2}\left(\sum_{i=1}^{6}(\gamma_x l_{i1} - 2\alpha_x l_{i2} + \beta_x l_{i3})^2\lambda_i^{-2}\right)^{1/2}|\Delta k| \tag{C.7}$$

The above formula holds for uncorrelated noise in the input vector $\vec{k}$, coming from noise in the pick-up.

"The secret to creativity is knowing how to hide your sources."

Albert Einstein

References

[1] The LHC online parameter database. http://www.cern.ch/lhc.

[2] F. Mandl and G. Shaw. *Quantum Field Theory*. Chichester-Wiley, 1984.

[3] The ALEPH Collaboration. Observation of an Excess in the Search for the Standard Model Higgs. CERN-EP/2000-138, Submitted to Physics Letters B.

[4] G. Giudice. Beyond the Standard Model. CERN Academic Training Lectures.

[5] U. Amaldi, W. de Boer, and H. Fürstenau. Comparison of Grand Unified Theories with Weak and Stong coupling constants measured at LEP. *Physics Letters B*, 260(3,4):447–455, 1991.

[6] F. Willeke. Report on the Working Group on Emittance Preservation. In *Proceedings of the workshop on LHC injectors (LHC'96)* [59].

[7] J. Gareyte. Requirements of the LHC on its injectors. In *Proceedings of the workshop on LHC injectors (LHC'96)* [59].

[8] M. Benedikt, editor. *The PS Complex as Proton Pre-Injector for the LHC – Design and Implementation Report*. Number CERN 2000-003 in Yellow Report. CERN, 2000.

[9] H. Goldstein. *Classical mechanics*. Addison-Wesley, 2nd edition, 1980.

[10] R.P. Walker. Radiation damping. In Turner [60]. CERN 94-01.

[11] D. Möhl. Stochastic Cooling (Storage Rings). In Turner [61]. CERN 95-06.

[12] B. Seligmann. An introduction to electron colling. In S. Turner, editor, *Proceedings of CERN Accelerator School – General Accelerator Physics Course*, CERN Yellow Report, Jülich, Germany, 1991. CERN 91-04.

[13] K. Schindl. Space charge. In S. Turner, editor, *Proceedings of CERN accelerator school: Beam measurement*, Montreux, Switzerland, 1998.

[14] L. Palumbo, V.G. Vaccaro, and M. Zobov. Wake Fields and Impedances. In Turner [61]. CERN 95-06.

[15] A. Sorensen. Introduction to intrabeam scattering. In S. Turner, editor, *Proceedings of CERN accelerator school*, CERN Yellow Report, Aarhus, 1986. CERN 87-10.

[16] K. Schindl. The PS Booster as Pre-Injector for the LHC. In *Proceedings of the workshop on LHC injectors (LHC'96)* [59].

[17] H. Koziol and K. Wittenburg. Summary on Transverse Emittance Measurement and Instruments. In R. Cappi, editor, *Proceedings of 4th ICFA Beam Dynamics Mini-Workshop on Transverse Emittance Preservation and Measurement*, Geneva, Switzerland, 1998. CERN/PS/DI/Note 98-03.

[18] R. Jung. Beam Profile Monitors. In J. Bosser [62], chapter 9. CERN-PE-ED 001-92.

[19] P. Elmfors et al. Wire Scanners in Low Energy Accelerators. *Nucl.Instr.Meth.*, A396:13–22, 1997.

[20] H. Schönauer. BEAMSCOPE – A Novel Device for Measuring Emittances and Betatron Amplitude Distributions. In *Proceedings of the 8th IEEE Particle Accelerator Conference*, IEEE Trans. Nucl. Sci.: 26 (1979), pages 3294–3296, San Francisco, CA, 1979.

[21] C. Bovet and R. Jung. A New Diagnostics Tool for Betatron Phase Space Matching into a Circular Accelerator. In *Proceedings of the 5th European Particle Accelerator Conference* [63], pages 1597–1599.

[22] C. Bovet et al. First Results from Betatron Matching Monitors Intalled in the CERN PSB and SPS. In *Proceedings of the 6th European Particle Accelerator Conference*, pages 1488–1890, Stockholm, Sweden, 1998.

[23] M. Benedikt et al. Study of New PSB-PS Transfer Line Optics with Improved Dispersion Matching by Means of Turn-Turn Beam Profile Acquisitions. CERN Internal Note PS/AE/Note 2001-003, 2001.

[24] L.L. Gol'din. Investigation of Charged-Particle Beams by Means of Signal Electrodes. *Instruments and Experimental Techniques*, pages 780–784, 1966. Translated from Pribory i Tekhnika Eksperimenta, No. 4, pp. 18-21, July-August 1966.

[25] G. Nassibian. The Measurement of the Multipole Coefficients of a Cylindrical Charge Distribution. CERN Internal Note SI/Note EL/70-13, 1970.

[26] R.H. Miller et al. Non-Intercepting Emittance Monitor. In *Proceedings of the 12th International Conference on High Energy Accelerators*, pages 602–605, Batavia, IL, 1983.

[27] J.C. Sheppard et al. Non-Intercepting Energy Spread Monitor. In *Proceedings of the 12th IEEE Particle Accelerator Conference*, volume 2, pages 757–579, Washington, DC, 1987.

[28] S.J. Russell. Emittance Measurements of the Sub-Picosecond Accelerator Electron Beam using Beam Position Monitors. *Review of Scientific Instruments*, 70(2):1362–1366, February 1999.

[29] G. Carron et al. Observation of Transverse Quadrupole Mode Instabilities in Intense Cooled Antiproton Beam in the AA. In *Proceedings of the 13th IEEE Particle Accelerator Conference*, volume 2, pages 803–805, Chicago, IL, 1989.

[30] V. Chohan, F. Pedersen, S. van der Meer, and D.J. Williams. Measurement of Coherent Quadrupole Oscillations at Injection into the Antiproton Accumulator. In *Proceedings of the 2nd European Particle Accelerator Conference*, volume 1, pages 320–322, Nice, France, 1990.

[31] M. Chanel. Study of Beam Envelope Oscillations by Measuring the Beam Transfer Function with a Quadrupolar Pick-up and Kicker. In *Proceedings of the 5th European Particle Accelerator Conference* [63], pages 1015–1017.

[32] J. Rossbach and P Schmüser. Basic Accelerator Optics. In Turner [60]. CERN 94-01.

[33] P.J. Bryant and K.Johnsen. *The Principles of Accelerators and Storage Rings*. Cambridge University Press, Cambridge, 1993.

[34] D.A. Edwards and M.J. Syphers, editors. *An Introduction to the Physics of High Energy Accelerators*. Wiley, New York, 1993.

[35] P.M. Lapostolle. Possible emittance increase through filamentation due to space charge in continuous beams. In *Proceedings of the 4th Particle Accelerator Conference*, IEEE Trans. Nucl. Sci.: 18 (1979), pages 1101–1014, Chicago, USA, 1971.

[36] A.W. Chao, editor. *Physics of Collective Beam Instabilities in High Energy Accelerators*. Wiley, New York, 1993.

[37] A.W. Chao and M. Tigner, editors. *Handbook of Accelerator Physics and Engineering*. World Scientific, 1999.

[38] E. Schulte. Beam Position Monitors (Pick-ups) and Q Measurement. In J. Bosser [62], chapter 5. CERN-PE-ED 001-92.

[39] R. Assmann et al. Use of Movable Beam Position Monitors for Emittance Measurements. In *Proceedings of the 7th European Particle Accelerator Conference* [64], pages 1693–1695.

[40] S.J. Russell and B.E. Carlsten. Measuring Emittance using Beam Position Monitors. In *Proceedings of the 15th IEEE Particle Accelerator Conference* [65], pages 2537–2539.

[41] M. Heald and J. Marion. *Classical Electromagnetic Radiation.* Saunders College Publishing, Orlando, 3rd edition, 1995.

[42] M. Read Teague. Image analysis via the general theory of moments. *J.Opt.Soc.Am*, 70(8):920–930, 1980.

[43] M. K. Hu. Visual Pattern Recognition by Moment Invariants. *IRE Trans.Info.Theory*, IT-8:179–187, 1962.

[44] Y. Yin. A Multistrip Beam Profile High Order Moment Monitor. In *Proceedings of the 15th International Conference on High Energy Accelerators*, pages 160–162, Hamburg, Germany, 1992.

[45] Y. Yin. Development of a Multistrip Monitor for Nonintercepting Measurement of Beam Geometric Moments. In *Proceedings of the 15th IEEE Particle Accelerator Conference* [65], pages 2441–2443.

[46] Y. Yin, B. Rawnsley, and G.H. Mackenzie. Measurement of Transverse Geometric Moments of the TRIUMF Beam with a Multistrip Monitor. In *Proceedings of 4th European Particle Accelerator Conference*, volume 2, pages 1658–1660, London, UK, 1994.

[47] G. Nassibian. The Basic Limits to the Measurement of the Charge Distribution in a Cylindrical Beam by Means of Electrostatic Induction Electrodes. CERN Internal Note SI/Note EL/71-2, 1971.

[48] S.J. Russell et al. Characterization of Beam Postion Monitors for Measurement of Second Moment. In *Proceedings of the 16th Particle Accelerator Conference* [66], pages 2580–2582.

[49] S.J. Russell. Preliminary Results of RMS Emittance Measurements Performed on the Sub-Picosecond Accelerator using Beam Position Monitors. In *Proceedings of 17th Particle Accelerator Conference*, pages 2177–2179, Vancouver, BC, 1997.

[50] S.J. Russell and B.E. Carlsten. Measuring Emittance Growth due to Magnetic Bunching of an Electron Beam using the Second Moment of its Image Charge. In *Proceedings of the 18th Particle Accelerator Conference* [67], pages 477–481.

[51] S.J. Russell. Unstable Matrix Equations and their Relationship to Measuring the Emittance of an Electron Beam using Beam Position Monitors. *Nuclear Instruments and Methods in Physics Research A*, 430:498–506, 1999.

[52] F.M. Bieniosek and K. Fullett. Measurement and Reduction of Quadrupole Injection Oscillations in the Fermilab Antiproton Accumulator. In *Proceedings of the 16th Particle Accelerator Conference* [66], pages 1942–1944.

[53] F. Caspers. Bench Measurements. In A.W. Chao and M. Tigner [37], Section 7.5.1.

[54] V.G. Vaccaro. Coupling Impedance Measurements: An Improved Wire Method. INFN/TC-94/023, 1994.

[55] Ansoft Corporation. The High Frequency Structure Simulator Program. http://www.ansoft.com.

[56] E. Jensen et al. RF Screening by Thin Resistive Layers. In *Proceedings of the 18th Particle Accelerator Conference* [67], pages 1408–1410.

[57] A. Jansson and D.J. Williams. A New Optimized Design of Quadrupole Pick-up using Magnetic Coupling. To be published in Nucl. Instr. Meth. in Phys. Res. A.

[58] R. Cappi, E. Metral, and D. Möhl. Transverse Instabilities in the Presence of Linear Coupling. In *Proceedings of the 7th European Particle Accelerator Conference* [64].

[59] *Proceedings of the workshop on LHC injectors (LHC'96)*, volume 58 of *Particle Accelerators*, Montreux, Switzerland, 1997.

[60] S. Turner, editor. *Proceedings of CERN Accelerator School – Fifth General Accelerator Physics Course*, CERN Yellow Report, Jyväskylä, Finland, 1992. CERN 94-01.

[61] S. Turner, editor. *Proceedings of CERN Accelerator School – Advanced Accelerator Physics Course*, CERN Yellow Report, Rhodes, Greece, 1993. CERN 95-06.

[62] J. Bosser, editor. *Beam Instrumentation.* CERN, Geneva, 1994. CERN-PE-ED 001-92.

[63] *Proceedings of the 5th European Particle Accelerator Conference*, Sitges, Spain, 1996.

[64] *Proceedings of the 7th European Particle Accelerator Conference*, Vienna, Austria, 2000.

[65] Proceedings of the 15th IEEE Particle Accelerator Conference. In *Proceedings of the 15th IEEE Particle Accelerator Conference*, Washington, DC, 1993.

[66] *Proceedings of the 16th Particle Accelerator Conference*, Dallas, TX, 1995.

[67] *Proceedings of the 18th Particle Accelerator Conference*, New York, NY, 1999.

Acknowledgements

I would like to thank my examining professor at Stockholm University, Sven-Olof Holmgren, and my supervisor at the Manne Siegbahn Laboratory, Örjan Skeppstedt, for their support. I would also like to thank my CERN supervisor, Mats Lindroos, who has done the day-to-day supervision of this work. I am also grateful to Karl-Gunnar Rensfelt at the Manne Siegbahn Laboratory for arranging my connection with Stockholm University and being my supervisor for the first half of the thesis work.

Finally, I would like to thank all my colleagues at CERN. In particular, without the enthusiastic support and experienced help of David Williams, the magnetic quadrupole pick-up could well have remained a good idea collecting dust in an internal note. When he retired, Lars Søby took over and was very helpful. Jean-Mary Roux in the drawing office checked the mechanical design, did the CAD drawings, and was very patient with the frequent design modifications. Erk Jensen helped with the simulations. Madeleine in the PS cafeteria made the coffee...

This work was supported by the Department of Physics at Stockholm University, Manne Siegbahn Laboratory and the PS division of the European Organization for Nuclear Research (CERN).